

UNIVERSITY OF CALIFORNIA

Los Angeles

Precipitating Shallow Cumulus Convection

A dissertation submitted in partial satisfaction of the
requirements for the degree Doctor of Philosophy
in Atmospheric and Oceanic Sciences

by

Aloisia Antoinette Nuijens

2010

The dissertation of Aloisia Antoinette Nuijens is approved.

J. David Neelin

Carlos R. Mechoso

Russel E. Caflich

Joao Teixeira

Bjorn B. Stevens, Committee Chair

University of California, Los Angeles

2010

Contents

1	Introduction	1
2	The Environment of Precipitating Shallow Cumulus Convection	7
2.1	Introduction	8
2.2	Data and methodology	10
a	Data	10
b	Methodology	17
2.3	Precipitation	20
a	Intensity and frequency of precipitation	20
b	Temporal and spatial variability	26
2.4	Meteorological environment	27
a	Atmospheric profiles	28
b	Deeper clouds, more rain?	30
c	Surface fluxes and winds	32
d	Relations between winds, humidity and echo fraction	35
2.5	Discussion	37

a	Bulk theory	38
b	Aerosol effects	41
2.6	Conclusions	43
3	The influence of wind speed on shallow cumulus convection from Large-Eddy-Simulation	46
3.1	Introduction	47
3.2	Simulation set-up	50
a	Case specifications	50
b	Strategy	52
3.3	Results	55
a	Stationary solution for the references cases	55
b	Transient response to a wind speed perturbation	58
c	Towards a new equilibrium	60
3.4	The buoyancy and mass flux response	62
3.5	A different behavior at strong winds?	65
3.6	Discussion and conclusions	69
4	A bulk perspective on the influence of wind speed	73
4.1	Introduction	74
4.2	The mixed-layer model	77
a	The mixed-layer model equations	77
b	The response to wind speed in comparison with LES	80

4.3	A two-layer shallow cumulus bulk model	83
a	A short description of the SCBM	84
b	Solution of the reference case	90
c	The response to wind speed	92
4.4	A simple explanation for the deepening response at stronger winds	95
4.5	Summary and conclusions	102
5	Summary and concluding remarks	105
A	Sensitivity to the Galilean transform	111
A.1	Introduction	111
A.2	Results	114
a	Thermodynamics and cloud properties	114
b	Precipitation	119
B	Turbulence effects on warm rain autoconversion in Large-Eddy Simulation	121
B.1	Introduction	121
B.2	Turbulence effects in LES	122
C	The shallow cumulus bulk model by Bretherton and Park	129
C.1	Prognostic equations	129
C.2	Cloud model	131

List of Figures

1.1	A cartoon illustrating the type of clouds along a typical trade-wind trajectory. From Stevens (2005).	3
1.2	Comparison of cloud top height detection from airborne lidar data (the NCAR aerosol backscatter lidar deployed during RICO, winter of 2004-2005) at an 18 dB threshold (connected red circles) with space-borne lidar data (the CALIPSO 333m product) for RICO (gray) and locations in the broader trades (black) during winter months in 2006, 2007 and 2008. From Medeiros et al. (2010).	4
2.1	Scheme indicating the 150 km radius domain of the SPolKa radar, located on Barbuda. Also shown are Spanish Point (Sounding / ISFF site) and the north-east domain in which aircraft (C-130) and ship (RVSJ) operations were performed.	11
2.2	Six hour averages of the sensible heat flux (left) and latent heat flux (right) are plotted for ISFF versus RVSJ (see section 2.1.iii) using data from January 3-25 (2005), where all frequencies < 26 hours have been removed.	16

2.3	a) Probability density functions of pixel rain-rate $P(R_i)$, i.e., the probability divided by the bin width, which, for bins less than 1 mm h^{-1} can be greater than 1. The solid line is the pdf conditioned on $Z_i > 7\text{dBZ}$ (corresponding to $R_i > 0.11\text{mm h}^{-1}$) for dataset I. Also shown are conditional pdf's for scans with $F < 0.03$ (dashed line) and $F > 0.03$ (dotted line). The x -axis is on a log-scale. b) The cumulative distribution of pixel rain-rates $C(R_i)$ corresponding to the solid line in a), with vertical lines indicating $C(R_i = 0.4 \text{ mm h}^{-1})$ and $C(R_i = 1 \text{ mm h}^{-1})$	21
2.4	The echo fraction F of each radar scan of dataset I is plotted versus month and day during RICO. The inset zooms in on the period between December 16 and January 8.	23
2.5	(a) The cumulative distribution function of the area rain-rate $C(R)$ using the radar scans in dataset I. (b) Six hour averages of echo fraction \bar{f} versus area rain-rate \bar{R} using dataset III.	25
2.6	Left panel: the mean echo fraction for three hour bins is plotted against local Atlantic Standard Time (AST) with the large dot denoting dataset I and the small dot dataset II. The bars are the mean and uncertainty in the estimate of the mean (σ/\sqrt{N}), where N equals the number of scans. Right panel: the mean echo fraction (indicated by the gray scale) for 15 radar segments for dataset II. The wind-rose indicates the frequency of wind direction during RICO as measured by the length of the thick horizontal lines, with mean wind speed printed at the end of each line.	26

2.7	Mean profiles of (from left to right): θ_e , $\theta - \bar{\theta}$, RH and u (with the uncertainty of the mean as a shaded area) for three composites: (dotted line) $0 < \bar{f} < 0.008$ with $\langle \bar{f} \rangle = 0.003$, (dashed line) $0.008 < \bar{f} < 0.03$ with $\langle \bar{f} \rangle = 0.014$ and (solid line) $\bar{f} > 0.03$ with $\langle \bar{f} \rangle = 0.05$. About 66 soundings are used in each composite.	29
2.8	Plotted are three composites (open circles), as well as six composites (filled circles), of the pressure level at which $RH = 75\%$, the integrated water vapor IWV , the lifting condensation level LCL and the pressure level at maximum $d\theta/dz$ (the inversion), against $\langle \bar{f} \rangle$. Errorbars denote the uncertainty in the estimate of the mean. Slightly more than 30 soundings are used in each of the six composites.	31
2.9	Vertical profiles of cloud fraction derived from lidar data. The solid line represents all free-tropospheric circles identified as 'wet' ($\bar{f} > 0.02$ with $\langle \bar{f} \rangle = 0.05$) and 'dry' ($\bar{f} < 0.02$ with $\langle \bar{f} \rangle = 0.007$). The asterisk is the condensate fraction for the wet circles as measured by the in situ probes of the aircraft, which is zero for the dry circles.	33
2.10	Similar as in Figure 2.8: plotted are both three and six composites of SST, wind speed, wind direction at 10 AGL (ISFF data), the sensible (SH), latent (LH) and θ_e -flux against $\langle \bar{f} \rangle$. Slightly more than 30 data points are used in each of the six composites.	34

2.11	(a)	Daily average echo fraction \bar{f}^d is plotted versus daily wind speed (average over a 1 km layer centered in the upper subcloud layer from SPol radial velocity data) for $\bar{f}^d > 0.02$ with vertical and horizontal bars as the uncertainty of the mean. Size of the dot varies according to the mean RH over a 900-750 hPa layer from soundings, and shading varies with the mean wind direction. In absence of soundings, rather just an error bar are plotted. The six days in Table 2.1 are excluded. (b) Same as in a, but for $\bar{f}^d < 0.02$. (c) Same as in (a) yet the size and thickness of the squares vary according to \bar{f}^d , with $\bar{f}^d > 0.02$, and the mean relative humidity is plotted on the y -axis. (d) Same as in (c) but for $\bar{f}^d < 0.02$	36
2.12	Illustration of the processes in a bulk trade-wind layer in equilibrium: wind speed (U), surface θ_e flux ($\overline{w'\theta'_e}$), subsidence velocity (\bar{w}) and the radiative flux difference (ΔQ) across the boundary layer depth (here denoted by h). Top and middle panel display composite 1 and 2 (sparse-precipitation regime), similarly, the middle and bottom panel display composite 2 and 3 (widespread-precipitation regime). θ_e profiles indicate the location of most pronounced variations in specific humidity.	40	
3.1	Initial profiles of liquid water potential temperature θ_l , specific humidity q_t , subsidence velocity w_s and absolute wind speed $U = \sqrt{(u^2 + v^2)}$ for case S _{8.5} (red), S _{7.5} (blue) and RICO (green). S _{8.5} and S _{7.5} have the same q_t profile (in blue). Dotted lines indicate the free tropospheric profile $d\theta_l/dz(z) = Q_r/w(z)$	50	

3.2	Profiles of liquid water potential temperature, specific humidity, zonal wind speed, the turbulent heat flux $\overline{w'\theta'_l}$, turbulent moisture flux $\overline{w'q'}$ and liquid water q_l for simulations of $S_{7.5}$ averaged over hour 52-60 (blue solid) and of $S_{8.5}$ averaged over hour 52-60 (red solid). Dotted lines in the moisture flux profiles correspond to the (negative of) the large-scale drying flux $\overline{w}\overline{q}$	56
3.3	Time series before and after the wind speed perturbation for case $S_{8.5}$. Panels show (from top to bottom): the boundary layer height h , the fraction of cloudy columns cc , the surface sensible heat flux SH , the surface latent heat flux LH , the surface buoyancy flux B and the mass flux at cloud base M for simulations U_{10} (blue), U_5 (grey) and U_{15} (dark blue).	59
3.4	Profiles of (a) liquid water potential temperature, (b) specific humidity, (c) the turbulent moisture flux $\overline{w'q'}$, (d) the turbulent heat flux $\overline{w'\theta'_l}$, (e) liquid water q_l , (f) zonal and meridional wind speed u, v , (g,h) the momentum fluxes $\overline{u'w'}$, $\overline{v'w'}$, (i,j) shear S and buoyancy B production of turbulent kinetic energy, (k) cloud core fraction cc_{core} , (l) cloud core vertical velocity w_{core} , (m) mass flux M , (n) the excess in virtual potential temperature $(\theta_{v,core} - \overline{\theta}_v)$ and (o) liquid water potential temperature deficit $(\theta_{v,l,core} - \overline{\theta}_{v,l})$. Profiles are averaged over hour 100-108 for U_5 (grey), U_{10} (blue) and U_{15} (dark blue). Dotted lines in the moisture flux profiles correspond to the (negative of) the large-scale drying flux $\overline{w}\overline{q}$ (see Equation 3.6).	61
3.5	Idealized illustration of the response of clouds and the vertical humidity profile to wind speed, as observed in LES.	64

3.6	Idealized sketch of the moisture balance for different wind speed cases, denoted by $U - \Delta U$, U and $U + \Delta U$. Top panels show humidity profiles. Bottom panels show profiles of the turbulent moisture flux $\overline{w'q'}$ (black) and large-scale drying flux $\overline{w}\overline{q}$ (red). The bottom left profile corresponds to an idealized subsidence profile. The subscripts 'h' and 's' refer to the inversion height and surface respectively.	66
3.7	Profiles of the RICO case (solid green lines) versus the S _{8.5} case (dashed blue lines), as averages over hour 52-60. RICO simulations are initialized with a (geostrophic) zonal wind profile that equals -9.9 (green), -14.9 (dark green) and -4.9 (grey) at the surface. Variable notation as in Figure 3.4.	68
3.8	Vertical profiles of equivalent potential temperature θ_e , humidity q and zonal wind speed u from radiosondes taken during RICO. The dotted and dashed lines correspond to regimes with little precipitation and moderate precipitation respectively. Adapted from Figure 2.7 in Chapter 3.	71
4.1	Illustration of the mixed-layer model.	79
4.2	Sensitivity of (a) specific humidity q_M , (b) potential temperature θ_M , (c) the surface moisture flux $\overline{w'q'}$, (d) the surface heat flux $\overline{w'\theta'}$, (e) the mixed-layer and cloud base height $\eta = z_{cl}$, (f) the surface buoyancy flux $\overline{w'\theta'_v}$, (g) and (h) the entrainment velocity E to wind speed U in the mixed-layer model for a range of $\Delta\theta_v = \{0.03\text{K (dark blue)} - 0.16\text{K (light green)}\}$. The red dots indicate one example of a solution in which Δq_t is adjusted as to maintain a constant $\overline{w'\theta'_v} _s$. Further details are given in the text.	81

4.3	Cartoon (taken from Bretherton and Park (2008)) illustrating the two-layer structure of the shallow cumulus bulk model.	85
4.4	Vertical cloud and mass flux structure from SCBM solutions at day 16 with a 10 m s^{-1} wind speed. The panels represent the mass flux (a), cloud liquid water (b), the θ_v excess (c), θ_{vl} -deficit (d) and q_t excess of cumulus updrafts. Different lines and colors represent different versions of the cloud plume model used (see legend and Appendix C).	90
4.5	Solutions of the SCBM versus wind speed at day 20 (the wind speed is perturbed on day 16). Panels show (from top to bottom, left to right) the sub-cloud layer q_t (a), the sub-cloud layer θ_{vl} (b), the surface moisture flux (c), the surface θ_{vl} (buoyancy) flux (d), cloud base height (e), inversion (cloud top) height (f), the q_t jump at cloud base (g), the mass flux at cloud base (h), the q_t jump at the inversion (i) and the θ_{vl} jump at the inversion. Different symbols correspond to different versions of the cloud plume model used, see legend and Appendix C.	93
4.6	The vertical structure predicted by the SCBM at day 20 for wind speeds of 10 m s^{-1} (black), 5 m s^{-1} (light grey) and 15 m s^{-1} (dark grey). The panels show profiles of q_t (a), θ_{vl} (b), liquid water q_l (c), the turbulent moisture flux (d), the turbulent flux of θ_{vl} (e) and the mass flux (f). Solid versus dashed lines indicate different cloud plume models used, see legend and Appendix C.	95

4.7	Cartoon illustrating the possible response of the temperature and humidity profiles (top) and the heat, moisture and buoyancy flux profile (middle) to a wind speed perturbation of δU , given the assumption that the boundary layer does not deepen. The initial equilibrium state is indicated by solid lines, the possible new equilibrium by dashed lines. Shown in red at the bottom is the response whereby $\delta Q_q, \delta Q_\theta = 0$, which leads to an inconsistency at h	99
A.1	Top panels show time series of inversion height z_i , total number of cloudy columns cc and liquid water path LWP for simulations with LES version 2 (green) and version 3 (blue) either without (lighter colors) or with (dark colors) a galilean transform. Lower panels show corresponding six hour averaged profiles of (from left to right, top to bottom) potential temperature θ_l , liquid (cloud) water r_c , zonal u and meridional v wind speed, and their variances. . .	115
A.2	Six hour averaged profiles for liquid (cloud) water r_c , cloud fraction cc , vertical velocity variance w'^2 , in-cloud vertical velocity (updraft speed) w_{cld} and in-cloud liquid (cloud) water $r_{c,cld}$. Top panel shows the base simulation with $\Delta t = 1$ s, limiters and 100 by 100 by 40 m resolution (colors as in Figure A.1). Lower panels show the base simulations (solid lines) versus simulations with a longer time step, higher resolution, or without limiters (dashed lines).	116
A.3	Labels as in Figure A.2, but for UCLA-LES version 3.0.	117

A.4	Left panels show six-hour averaged profiles of cloud water r_c , rain water r_r , gradient of virtual potential temperature $d\theta_v/dt$ and updraft speed w_{cld} . Rightmost panels show time series of inversion height z_i , total number of cloudy columns cc , liquid (cloud+rain) water path LWP , rain water path RWP and surface precipitation P_{sfc}	119
B.1	Time series of the number of cloudy columns (cloud fraction) C , liquid (cloud + rain) water path L , rain water path R and surface rain-rate R_{sfc} for simulations with cloud droplet number concentrations N_c of 140 cm^{-3} (grey) and 300 cm^{-3} (black), without turbulence-enhanced coalescence (dashed line) and with turbulence-enhanced coalescence (solid line)	126
B.2	Snapshot of the initial development of precipitation in a typical cumulus cloud from the LES. Shown from left to right are the dissipation, cloud-water mixing ratio and rain-water mixing ratio. The latter two share the color bar on the far right.	128

List of Tables

2.1	The daily average echo fraction, wind speed, wind direction (derived from radial velocity data) and mean relative humidity between 900 and 700 hPa (from the daily mean sounding) for six days during RICO identified as 'disturbed days' (section 2.5).	18
2.2	The number of radar scans, soundings and surface data, details of the domain and the symbol for echo fraction (with its mean value) and area-average rainfall (with its mean value in mm h^{-1} and W m^{-2}) of the datasets used in section 3.1 and 3.2 (I), 3.3 (II), section 4.1-4.3 (III) and section 4.4 (IV).	19
3.1	The initial and boundary conditions, forcings and other numerical specifications for the simulations $S_{8.5}$, $S_{7.5}$ and RICO. Details and explanation of the variables is given in the text. ⁽¹⁾ $w(z) = w_0(1 - e^{-z/H})$, ⁽²⁾ $Q_r + Q_{\theta_l}$, ⁽³⁾ $d\theta_l/dz(z) = Q_r/w(z)$, ⁽⁴⁾ stretched grid at $z > 4$ km.	54
4.1	The initial conditions and forcings derived from case S1 used in Chapter 4 (Table 3.1) and here used for the mixed-layer model.	82

4.2	Estimates of cloud base height z_{lcl} , entrainment rate E , turbulent moisture and heat fluxes at $\eta = z_{lcl}$ (from Equation 4.7), and the humidity, potential temperature and virtual potential temperature jumps $\Delta q_t, \Delta \theta_l, \Delta \theta_v$ at $\eta = z_{lcl}$ (from Equation 4.8 and noting that in equilibrium $E = M - \bar{w}$). All estimates are averages of the last eight hours of simulation of the S1 case performed with LES (Chapter 4).	84
4.3	The initial conditions and forcings for the SCBM derived from the equilibrium state of case S2 used in Chapter 4 (Table 3.1). Values of $p_B, p_I, SST - T_{MS}, \epsilon$ and δ are based on eight hour averages at the end of the S2 U10 simulation. ⁽¹⁾ $\bar{w}(z) = \bar{w}_0(1 - e^{-z/H}), \bar{w}_0 = 8.5 \cdot 10^{-3} \text{ m s}^{-1}, H = 1000 \text{ m}$	91
A.1	Sensitivity to Galilean transform (NG = no transform, G = galilean transform) as well as resolution, time step and use of limiters for scalar advection for UCLA-LES version 2.0 (leapfrog) and version 3.0 (runge-kutta). All simulations are without micro-physics, unless denoted by <i>precip</i> , in which case cloud droplet number concentrations equal $N_c = 70 \text{ mg}^{-1}$. Variables are averages over the last six hours of each simulation (12 hours in total) and represent: CFL number, cloud (liquid) water path L , inversion height z_i , fraction of cloudy columns C , rain water path R , surface rain rate P_{sfc} and rain-drop number concentrations averaged over raining regions only N_r	113

B.1 Sensitivity to turbulence-enhanced coalescence T, versus no turbulence enhancement NT, for cloud droplet number concentrations $N_c = 70, 140$ and 300 mg^{-1} . NT-140-hr and T-140-hr represent simulations with doubled horizontal resolution (grid spacing of 50 m). Variables are cloud (liquid) water path L , rain water path R , inversion height z_i , fraction of cloudy columns C , rain-drop number concentrations averaged over raining regions N_r , surface rain rate R_{sfc} and the maximum rain-rate R_{max} within the (domain-averaged) profile of rain-rate. All variables are averaged over the last four hours of each simulation. 127

ACKNOWLEDGEMENTS

The material in Chapter 2 is reproduced from Nuijens et al. (2009) (copyright by the American Meteorological Society, AMS) and is used in this dissertation by permission of the publisher. The authors of the paper wish to express their appreciation to Bob Rilling at NCAR for his helpful suggestions on the quality control of the SPolKa radar data. The first author would like to thank Margreet van Zanten and the Atmospheric Research Group at the Royal Netherlands Meteorological Institute (KNMI) for their help and hospitality throughout the course of this study. Thanks go to Chris Holloway for motivating conversations on our analysis, to Brian Medeiros and Robert Wood for careful comments on earlier versions, and to an anonymous reviewer who challenged us to think more deeply about aerosol-meteorology relationships which greatly improved the manuscript. This work was supported by NSF through Grant ATM-00342625.

The material in Appendix B is an excerpt of a manuscript in preparation for publication in the Quarterly Journal of the Royal Meteorological Society. The manuscript is titled “Turbulence effects on warm-rain autoconversion in precipitating shallow convection”, authored by Axel Seifert, Louise Nuijens and Bjorn Stevens. I wish to acknowledge both my co-authors for their guidance in the development of my contribution to this manuscript.

First, I want to thank my advisor Bjorn Stevens. Working with him has been one great moving experience, and not only literally. He has been a continuous source of inspiration and has ensured that research is a challenge but mostly a lot of fun. Of all the things I would like to thank him for, the most important ones are for having so much trust in me and for stimulating me to become an independent researcher. Bjorn has helped to make each place an interesting one, with new friends and colleagues and

exposure to more research. My life in Los Angeles and Hamburg would have not been the same without his care and encouragement and I hope to have him as a mentor and friend for many more years.

I would like to thank my committee, Carlos Roberto Mechoso, David Neelin, Russ Caffisch and Joao Teixeira, for their positiveness towards my work and for many nice chats during my time at UCLA. I enjoyed taking your classes, being your teaching assistant and seeing you at conferences. I would also like to thank Kristen Corbosiero and Kuo-Nan Liou for being involved at various stages of my classwork, research and life.

I very much enjoyed writing and discussing with Pier Siebesma, Margreet van Zanten, Axel Seifert and Brian Medeiros and I hope to continue our collaborations. A special thanks goes to Jordi Vila Guerau-de Arellano, for his endless enthusiasm and interest in my work long before and long after I started my PhD. I always enjoy our meetings, whether in rainy Wageningen or sunny Cancun. Many thanks to Gilles Bellon, for sharing his work on bulk models and LES with me, from which Chapter 3 has greatly benefited. Many thanks also go to Chris Bretherton for sharing his model and comments that I have gratefully made use of in Chapter 4. Lastly, I would like to acknowledge the helpful comments and suggestions from Georgios Matheou, Joao Teixeira, Thijs Heus and Harm Jonker on LES and its numerics.

Moving around has one great advantage: meeting many interesting people and I feel truly lucky to have so many colleagues as my friends and vice versa. I am very thankful for all the help and support I received during my first year at UCLA from the more experienced PhD's and friends: Simona Bordoni, Chris Holloway, Mimi Hughes, Slobodan Jovicic, Nikki Lovenduski, Brian Medeiros and Verica Savic-Jovicic. I would

also like to thank my friends and classmates Sergio Abarca, Sarah Kapnick, Liang Jun-Hong and Matina Gkioulidou. I spent much time with you struggling through classes and research, as well as celebrating our accomplished goals afterwards. It (almost) makes me want to struggle on a little longer. Much too short was the touch of Italian in LA ... I am grateful for the delicious dinners and time spent unplugging wires with Laura Zamboni, Diego Fazi, Chiara Antoniazzi and Alberto Villa. And to my relief, dark and rainy days in Hamburg were much less dark (though still rainy) with the company of Fast Fast & Friends.

Most of all, I am thankful for all the love and support from my parents. Because of you and our daily to weekly contact, especially in the last few months, home never feels very far away. It must not have been easy having me move around so much, and I think you have seen way too much of Schiphol (at least you know where to find the best coffee there). All the dinners, walks in the woods and movie nights that I spent at home, with you and with Jeannette and Fabian, were really great.

Lastly, I would like to thank Daniel. Meeting him may have been the best thing about moving around. I admire his interest in all kinds of science, people and places and through him and his work I am being challenged to have a broader view on many things. Most of all though, I love him for trying to live by the rule that life should be fun, and so with him it is.

Louise Nuijens

Los Angeles, California

May, 2010

VITA

- April 20, 1983** Born, Pretoria, Republic of South-Africa
- 2005** B.S. in Soil, Water and Atmosphere
Wageningen University, Wageningen, The Netherlands
- 2006** M.S. in Meteorology and Air Quality
Wageningen University, Wageningen, The Netherlands
- 2006-2007** IGPP Fellowship
University of California, Los Angeles
- 2007-present** Research Assistant
Department of Atmospheric and Oceanic Sciences
University of California, Los Angeles
- 2008** M.S. in Atmospheric and Oceanic Sciences
Department of Atmospheric and Oceanic Sciences
University of California, Los Angeles
- 2008** Bosart Award “for positive contribution to department
life”
Department of Atmospheric and Oceanic Sciences
University of California, Los Angeles
- 2009** Teaching Assistant
Department of Atmospheric and Oceanic Sciences
University of California, Los Angeles

PUBLICATIONS AND PRESENTATIONS

- Medeiros, B., L. Nuijens, C. Antoniazzi and B. Stevens 2010: Low-latitude boundary layer clouds as seen by CALIPSO. Submitted to *J. Geophys. Res.*
- Nuijens, L., B. Stevens and A.P. Siebesma 2009: The environment of precipitating shallow cumulus convection. *J. Atmos. Sci.*, 66, 1962-1979
- Rauber, R.M., B. Stevens and co-authors 2007: Rain in (shallow) cumulus over the ocean - The RICO campaign. *Bull. Amer. Soc. Meteor.* 88 (12), 1912-1928
- Rauber, R.M., B. Stevens and co-authors 2007: In the Drivers Seat - RICO and Education. *Bull. Amer. Soc. Meteor.* 88 (12), 1929-1937
- Seifert, A., L. Nuijens and B. Stevens 2010: Turbulence effects on warm-rain autoconversion. Submitted to *Quart. J. Roy. Meteor. Soc.*
- Van Zanten, M.C., B. Stevens, L. Nuijens, A.P. Siebesma and co-authors 2010: Controls on precipitation and cloudiness in simulations of shallow fair-weather cumulus. In preparation for *Atmos. Chem. Phys.*.
- Nuijens, L. and B. Stevens: Relationships between wind speed, humidity and precipitating shallow cumulus convection. CFMIP/GCSS Boundary Layer WG Workshop, Vancouver, Canada, June 2009
- Nuijens, L., M.C. Van Zanten, A.P. Siebesma and B. Stevens: The LES Intercomparison case on precipitating shallow cumulus. CFMIP/GCSS Boundary Layer WG Workshop, Vancouver, Canada, June 2009
- Nuijens, L. and B. Stevens: Relationships between wind speed, humidity and precipitating shallow cumulus convection. Workshop on Advanced concepts for boundary layer parameterizations, Offenbach, Germany, May 2009

- Nuijens, L. and B. Stevens: Relationships between wind speed, humidity and precipitating shallow cumulus convection. European Geophysical Union meeting, Vienna, April 2009
- Nuijens, L.: The environment of precipitating shallow cumulus convection. Aerosol, Clouds & Climate Group Meeting, Max Planck Institute for Meteorology, Hamburg, Germany, January 2009
- Nuijens, L. and B. Stevens: On the chances of getting wet. Poster presentation at the Autumn School on 'Climate Change, Causes and Impacts', Paphos, Cyprus, 12 - 19 October 2008
- Nuijens, L.: The chances of rain showers in the trades. Department of Meteorology, University of Reading, UK, November 2008
- Nuijens, L. and B. Stevens: On the chances of getting wet. Poster presentation at the 15th International Conference on Clouds and Precipitation, Cancun, Mexico, July 2008
- Nuijens, L. and B. Stevens: The chances of getting wet. 4th Pan-GCSS meeting 'Advances on Modeling and Observing Clouds and Convection', Toulouse, France, June 2008
- Nuijens, L. and B. Stevens: Precipitating Shallow Cumulus: Poster presentation at the Berkeley Atmospheric Sciences Center (BASC) Symposium, Berkeley CA, September, 2007

ABSTRACT OF THE DISSERTATION

Precipitating Shallow Cumulus Convection

by

Aloisia Antoinette Nuijens

Doctor of Philosophy in Atmospheric and Oceanic Sciences

University of California, Los Angeles, 2010

Professor Bjorn B. Stevens, Chair

This dissertation explores relationships between precipitating shallow cumulus convection and large-scale meteorological conditions. Using observations in a typical shallow “trade-wind” cumulus region, the variability in convection and precipitation is addressed in connection with variability in boundary layer structure, winds, subsidence and open-sea surface fluxes. Large-Eddy-Simulation (LES) and bulk theory are used to further explore the explicit role of wind speed on convection.

S-Band radar data reveal that warm rain showers from trade-wind cumuli are prevalent, contributing to at least half of the total rainfall in the region. Soundings, surface flux and lidar data suggest that even within this meteorological regime, the undisturbed trades, subtle fluctuations in the strength of the easterly wind and in subsidence play a major role in regulating boundary layer humidity and the occurrence of clouds and rain,

whereas aerosol effects likely play a minor role.

In LES the response to an increase in wind speed is a moistening of the sub-cloud and cloud layer and a significant deepening of the cloud layer. The deepening leads to more dry and warm air mixed into the layer, maintaining a large surface moisture, but small surface heat flux at stronger winds. This ensures that surface buoyancy, cumulus updraft buoyancy as well as the convective mass flux change little. Cumuli at stronger winds are therefore deeper, but not more vigorous or numerous. Simple bulk concepts demonstrate that with a wind speed increase, but constant boundary layer depth, an inconsistency in the buoyancy budget of the sub-cloud layer develops. Deepening the layer can resolve this inconsistency. It is suggested that the deepening response may be independent of detailed internal dynamics of clouds and how they mix with the environment.

Both LES and bulk models indicate a limited regime in which equilibrium solutions are reached and cumuli remain shallow with tops below 3-4 km. This calls for a better understanding of the dynamics of cumulus congestus. Furthermore, because of its profound influence on the humidity structure and cloud depth, wind speed should be acknowledged as an explicit force in studies of shallow convection, in particularly those addressing interactions between cloud, aerosol and precipitation.

Chapter 1

Introduction

The “*trades*” owe their name to the prevailing pattern of easterly surface winds found over subtropical oceans that once made foreign commerce flourish. Even though the trade winds have long lost their commercial value, their historical name is still commonly used in the field of atmospheric sciences and reminds one of their ability to bridge large distances overseas. Through their transport of relatively dry air from higher latitudes towards the equator, trade winds induce evaporation from the ocean’s surface. This helps drive turbulent moisture fluxes in the lower boundary layer and the triggering of moist convection. In the heart of the trades, between 30°N and 30°S but outside of the Intertropical Convergence Zone (ITCZ), one can therefore find extensive fields of shallow “*trade-wind*” cumuli.

Trade-wind cumuli have tops that are mostly confined below the freezing level (typically near 5 km). Their growth is limited by a stable layer known as the trade inversion that separates the easterly winds in a moist well-mixed layer from the westerlies in the warm and dry free troposphere (Figure 1.1). Further into the tropics, the tropospheric stability is lower and the oceans are warmer, allowing convection to be deeper. The easterly winds meet at the ITCZ where strong upward motion is present, which at high

altitudes diverges into north and southward directed flow. This circulation, well-known as the Hadley circulation, is completed by strong subsiding motion over colder subtropical oceans at higher latitudes. These regions are marked by a strong trade inversion and a persistent stratocumulus-topped boundary layer.

Understanding what controls the vertical structure of airmasses and the clouds they embed along a trade-wind trajectory has been a major topic of interest in the past decades. In particular much attention has been given to the transition between stratocumulus and cumulus at the higher latitude side of the trades. If the partitioning between these two cloud types changes in a hypothetically warmer climate, this may substantially affect the radiative (cooling) impact of low-level clouds, hence the extent to which they offset greenhouse warming. Although compared to stratocumulus the radiative impact of shallow cumuli is small, their impact on tropical dynamics is not. By transporting moisture upwards and evaporating into the inversion, they essentially premoisten the atmosphere for deeper convection. The associated downward mixing of dry and warm air from the free troposphere also helps maintain a strong surface evaporation. If their moistening efficiency is reduced, humidity gradients across the tropics increase. This may inhibit deep convection at the edges of the ITCZ, but intensify convection in its center, with consequent impacts on the energetics of the large-scale circulation (Tiedtke 1989; Neggers et al. 2007).

Much of our current knowledge on trade-wind cumuli stems from a handful of early field studies (Austin 1948; Byers and Hall 1955; LeMone and Pennell 1976), some larger field campaigns such as ATEX and BOMEX, as well as from Large Eddy Simulation (LES) and theoretical studies (Arakawa and Schubert 1974; Betts and Ridgway 1989; Stevens et al. 2001; Siebesma et al. 2003; Stevens 2006, 2007). Because trade-

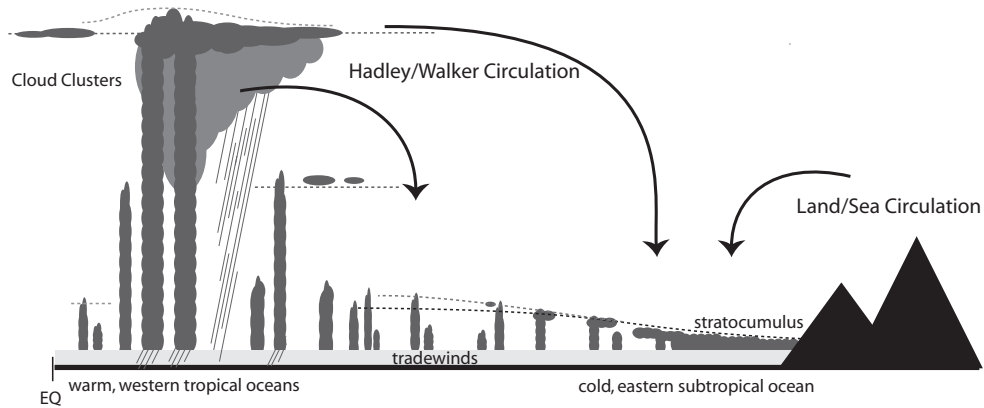


Figure 1.1: A cartoon illustrating the type of clouds along a typical trade-wind trajectory. From Stevens (2005).

wind cumuli in many of these studies are typically not deeper than 1-3 km, nomenclature refers to them as shallow. Observations however reveal that cumuli with tops up to 4-5 km, more typical of “congestus”, are in fact not uncommon in the trades (Figure 1.2) (Zhao and Di Girolamo 2007; Medeiros et al. 2010). Recent satellite- and ground-based remote sensing also contribute to the recognition that trade-wind cumuli can be accompanied by significant rain showers (Short and Nakamura 2000; Schumacher and Houze 2003; Nuijens et al. 2009) and that fields of cumuli take many different forms and patterns of organization other than scattered “popcorn” cumuli. These advances have triggered a renewed interest in shallow cumulus that has spun-off many questions. Why do these clouds rain so easily and how does this relate to aerosol effects? Does the organization of cumuli impact their overall behavior and statistics? What is the role of cold pools created by evaporation of rain water?

Relationships between clouds and precipitation are not the only uncertainties. Generally, relationships between the overall statistics of shallow cumuli and a varying large-scale environment remain to be understood in more detail. This has become particularly

evident as global climate models (GCM's) indicate different responses of these clouds to a warming climate (Bony et al. 2004; Medeiros et al. 2008), contributing to the uncertainty in estimating climate sensitivity. To improve the representation of shallow clouds in climate models a better understanding of processes on a range of scales is required. Particularly important is to evaluate how and to what extent processes on smaller scales affect those on larger scales and vice versa. For instance, precipitation may affect the vertical structure and organization of shallow cumulus, which in turn may affect the humidity structure of airmasses that are transported into the tropics. Hence, is it crucial to include precipitation in our representation of shallow cumulus? Such questions and thoughts have motivated and inspired this thesis, which focuses on relationships between precipitating shallow cumulus convection and the large-scale environment.

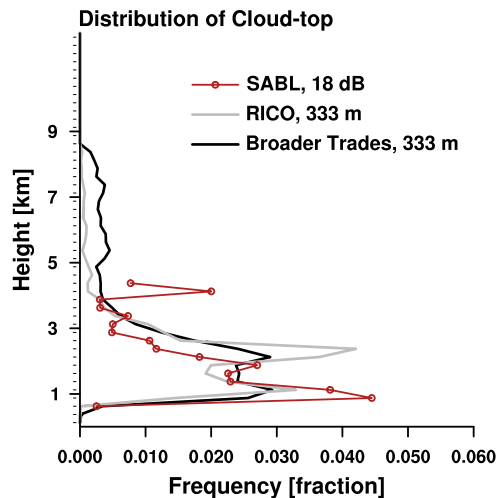


Figure 1.2: Comparison of cloud top height detection from airborne lidar data (the NCAR aerosol backscatter lidar deployed during RICO, winter of 2004-2005) at an 18 dB threshold (connected red circles) with space-borne lidar data (the CALIPSO 333m product) for RICO (gray) and locations in the broader trades (black) during winter months in 2006, 2007 and 2008. From Medeiros et al. (2010).

Chapter 2 addresses the questions: how much do shallow cumulus precipitate, is it

significant and how does variability in precipitation relate to variability in the environment? The analysis is based on observations that are taken from the Rain In Cumulus over the Ocean (RICO) Rauber et al. (2007) field study. RICO took place in a typical trade-wind region, in the vicinity of the Caribbean islands Antigua and Barbuda in the winter of 2004 and 2005. Designed in part to help address a general lack of cloud and precipitation statistics, RICO deployed a high-resolution ground-based radar. In Chapter 2, the frequency and intensity of shallow precipitation is studied using S-Band data from this radar. Additional data, including radiosonde, land-based and airborne-lidar data, are used to relate precipitation variability to the environment. These suggest that subtle fluctuations in the strength of the easterly winds and in subsidence play a major role in regulating environmental humidity, hence the occurrence of clouds and precipitation within the trades.

Wind speed is a particularly intriguing force as it may affect both the humidity structure of the trade-wind layer as well as the aerosol, thereby influencing clouds in more than one way. Because wind speed is most often kept constant in simulations of shallow cumulus convection, we do not precisely know the extent to which it influences cloud statistics, let alone precipitation statistics. Because satellite coverage during RICO was small and the cloud statistics from radar not reliable, the relationship between wind speed and shallow cumulus has not been evidently established from observations either.

In Chapter 3, Large-Eddy Simulations of typical shallow-cumulus cases are used to explore the impact of a wind speed perturbation on clouds, surface fluxes and the equilibrium structure of the trade-wind layer. A similar question is explored in Chapter 4, but from a theoretical point of view. Can simple bulk theory be used to understand the impact of wind speed? How important are the internal dynamics of clouds and the

way they mix with their environment? In the same chapter we give a simple explanation for the response of shallow cumulus convection to wind speed that is observed in LES and in well-known bulk models.

Even though precipitation was part of the motivation for our wind speed experiments, as of yet we ignore it in the simulations. The first reason for doing so is that precipitation, through its impact on cloud depth and boundary layer growth (Stevens 2007; Xue et al. 2007; Stevens and Seifert 2008), may obscure a relationship between wind speed and clouds that we first wish to establish. The second reason is that numerical errors are still a caveat in LES. In exploring the influence of numerics on cloud and precipitation statistics (Appendix A), it is found that precipitation exhibits a somewhat worrisome sensitivity to the CFL criterion of the flow, an effect that can be particularly large in comparing flows that move at different (wind) speeds. Nonetheless, if aware of such sensitivities, LES can still be used meaningfully to study precipitation and its relationship to macroscopic features of clouds (Appendix B). In our summary and concluding thoughts, we shall reflect on precipitation and ask how it may affect our wind speed simulations and possibly explain differences between the observations and the simulations (Chapter 5).

Chapter 2

The Environment of Precipitating Shallow Cumulus Convection

Abstract

Quantitative estimates of precipitation in a typical undisturbed trade-wind region are derived from two months of radar reflectivity data and compared to the meteorological environment determined from soundings, surface-flux, and airborne-lidar data. Shallow precipitation was ubiquitous, covering on average about two percent of the region and contributing to at least half of the total precipitation. Echo fractions on the scale of the radar domain range between zero to ten percent and vary greatly within a period of a few hours to a day. Variability in precipitation relates most strongly to variability in humidity and the zonal wind speed, although greater inversion heights and deeper clouds are also evident at times of more rain. Our analysis suggests that subtle fluctuations in both the strength of the easterlies and in subsidence play a major role in regulating humidity, hence precipitation, even within a given meteorological regime, here the undisturbed trades.

2.1. Introduction

Precipitation from shallow cumulus clouds over subtropical oceans, commonly described as warm rain showers, has been observed in several past studies (Byers and Hall 1955; Austin et al. 1996; Petty 1999; Johnson et al. 1999). Detailed estimates of the frequency, intensity and areal coverage of this type of precipitation however, in particular over larger areas and longer time periods, are scarce. The small area covered by these clouds, and thus the area covered by precipitation, are hard to measure using visible, microwave and infrared sensors aboard operational satellites. Sensor footprints are often too coarse and clouds and precipitation at higher levels can easily obscure low-level clouds and precipitation near the surface.

Recent studies using data from the space-born Tropical Rainfall Measuring Mission Precipitation Radar (TRMM PR), operational since December 1997, have indicated that shallow precipitation may contribute an appreciable amount to the total precipitation in the tropics (Short and Nakamura 2000; Schumacher and Houze 2003; Lau and Wu 2003), with estimates ranging up to 20%. These estimates are based on subsets of TRMM data for which the majority of radar echoes (that span at least 750 m in depth) have tops below 3 km. Although the TRMM PR benefits from a high vertical resolution and low rain-rate detection (a minimum of $0.4\text{-}0.5\text{ mm h}^{-1}$), it is yet unclear how much precipitation from shallow cumulus is actually observed by TRMM. Sensitivity and resolution effects can lead to an under sampling of radar echoes at low levels, in particular at off-nadir scanning angles due to radar main-lobe contamination (Short and Nakamura 2000).

The representation of shallow cumulus clouds in climate models and the role they

may play in determining climate sensitivity is an ongoing topic of interest (Bony et al. 2004; Medeiros et al. 2008). If a significant amount of precipitation over tropical oceans is in fact from shallow cumuli, a better understanding of interactions between precipitation and a cumulus population that may determine cloud fraction and cloud optical depth, hence cloud-radiative feedbacks, is required. Since microphysical processes were not incorporated in past modeling studies of shallow cumulus convection, several important questions are left unanswered: How much precipitation does a typical cumulus cloud produce? Do deeper cumuli rain more, and does precipitation significantly affect boundary layer dynamics? What is the influence of chemical factors i.e., the aerosol, on precipitation?

Recently a number of Large Eddy Simulation (LES) studies focused specifically on precipitating shallow cumulus. A GCSS* intercomparison case, based on observations from the Rain In Cumulus over the Ocean (RICO) field campaign (Rauber et al. 2007), surveys the microphysical robustness among different LES codes. Other LES studies that include microphysical processes show that increasing the humidity in the cloud layer leads to deeper clouds that rain more, but also indicate that precipitation itself may limit cloud growth, and hence the boundary layer depth (Stevens 2007; Stevens and Seifert 2008). Aerosol-cloud interactions, discussed by Xue and Feingold (2006) and Xue et al. (2007), indicate that the response of bulk cloud parameters to changes in the aerosol is complex. For instance, in their LES study cloud fraction decreases with increasing aerosol concentrations, opposite to the hypothesized aerosol second indirect effect, while aerosols may not only suppress precipitation, but also lead to enhanced droplet evaporation.

*Global Energy-Water Experiment (GEWEX) Cloud System Studies

Thus far, the results of several of these studies have not been compared to observations. Most modeling studies that focus on the role of the aerosol use idealized cases and prescribe large-scale forcings and initial temperature, humidity and wind profiles. In order to study aerosol effects however, particularly on larger scales, one also requires an understanding of the importance of meteorological factors in controlling clouds and precipitation, hence our study. Our specific interest is to obtain a better understanding of the following: to what extent can variability in shallow precipitation be related to variability in the meteorological environment?

The extensive dataset collected during RICO, set in a typical trade-wind region near the Caribbean islands of Antigua and Barbuda for a period slightly over two months, offers the opportunity to address this question from an observational point of view. A ground-based radar (SPolKa), scanning an area up to 150 km in radius, measured precipitation-related quantities with high resolution in both space and time. In addition, a variety of airborne, ship-based and land-based measurements were taken. Our objectives in this paper are two-fold: first, to present quantitative estimates of precipitation from shallow trade-wind cumuli (section 3); and second, to discuss precipitation variability in relation to variability in the meteorological environment (section 4).

2.2. Data and methodology

a. Data

All data used in this study have been collected in the close vicinity of the Caribbean islands of Antigua and Barbuda, mainly in a region upwind (northeast) of Barbuda (Figure 2.1). RICO operations lasted for 63 days, starting on November 24, 2004 and ending on January 25, 2005. A detailed overview of all operations and their time frames can

be found in Rauber et al. (2007). A weather summary by Caesar (2005) describes the meteorological conditions during RICO as typical for this region and time of year, with a cloud field dominated by shallow cumulus clouds organized as bands, clusters and isolated scattered cells. A few tropical waves, low and upper level troughs and weak cold fronts were present, but less than 5% of the total period was overcast or dominated by heavy precipitation associated with such disturbances. These disturbed periods are excluded from the analysis, as described in section 2.b.

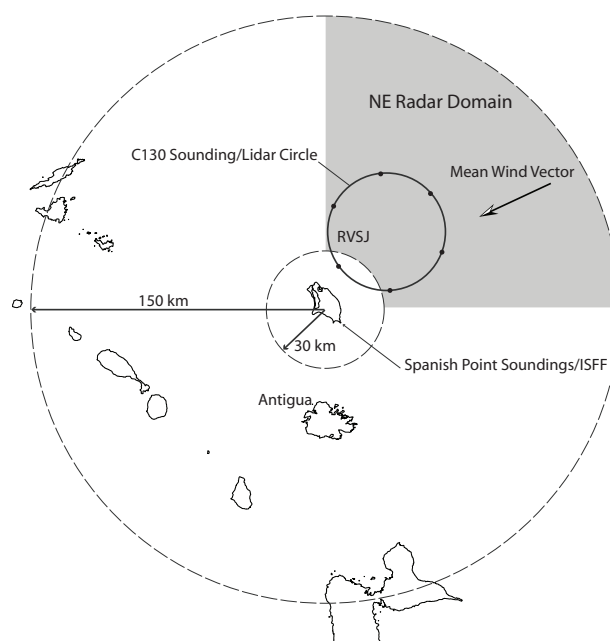


Figure 2.1: Scheme indicating the 150 km radius domain of the SPolKa radar, located on Barbuda. Also shown are Spanish Point (Sounding / ISFF site) and the northeast domain in which aircraft (C-130) and ship (RVSJ) operations were performed.

Radar reflectivity data Radar reflectivity data are obtained from measurements by the ground based S- and K-Band Dual Polarization radar (SPolKa), located on Barbuda (17.6°36.448' N, 61°49.457' W). The radar, with a beam width of 0.91°, performed

scanning routines at several elevation angles, from 0.5° up to 16.5° with a 1° increment. Only the S-Band (10.68 cm wavelength) data for the surveillance scans (the 360° scans taken at the 0.5° elevation angle that have a maximum range of 150 km), are used in the present study. These scans were performed approximately every 20 minutes, resulting in about 70 scans per day and a total of 3662 scans during RICO. Each scan is re-gridded onto a polar grid with a mesh of 150 m (in range) and 0.67° (in azimuth angle), comprising 984×540 pixels in total.

To exclude noise and anomalous returns from ground and sea clutter, birds etcetera, the scans are subjected to a multi-tiered filtering procedure. Histograms of unfiltered and filtered data are compared to evaluate each filtering procedure (not shown). First, radar noise, identified as pixels with a received radar power less than -115 dBm, and ground clutter, identified by island pixels that experience high reflectivities at the exact same coordinates in each scan, are removed. Second, pixels with differential reflectivity values outside an acceptable range of -1.5 - 3 dB that arise from objects with degrees of anisotropy much larger than expected from a raindrop, are removed. Third, pixels within a close range of the radar (< 60 km) showing irregular radial velocities or single isolated pixels with high reflectivities, presumably associated with birds and sea clutter, are removed as well. Fourth, a reflectivity threshold of 7 dBZ is used to exclude Bragg scattering returns caused by turbulent fluctuations in the refractive index of air due to humidity and temperature, for instance near the trade inversion or cloud edges. The 7 dBZ threshold is loosely based on findings from Knight and Miller (1993, 1998), who investigated the magnitude of Bragg scattering returns in and near clouds by considering theoretical expressions of the returned radar power from either hydrometeor or index of refraction variations, and who suggest 10 dBZ as a safe threshold above which Bragg

scattering is negligible. Note that some hydrometeor scattering from for instance light drizzle may be removed using the 7 dBZ threshold, hence estimates presented here likely underestimate the amount of rainfall from cumulus. While the expression 'radar echo' is commonly used for any signal on a radar scan other than noise, it refers in our paper only to those pixels that survived the filtering procedure.

Within 30 km of the radar, azimuthal-average reflectivities deviate significantly from values beyond 30 km. A reflectivity maximum is present within a 15 km range and may be explained by the presence of very small echoes, possibly noise or birds not captured by the filtering procedure. Trivej and Stevens (2010) show that the number of echoes close to the radar are anomalously high (their Figure 10a). In our analysis only data beyond a 30 km radius is used. At 30 km, the radar beam roughly scans a layer from the surface to 500 m above sea level, sampling precipitation in the subcloud layer. Beyond this range, the beam geometry is such that precipitation both below and in clouds is sampled. Beam broadening and changes in reflectivity with height, associated with the evolution of the hydrometeor size spectrum within the rainshaft, contribute to a general decrease of the azimuthal-average reflectivity of about 2 dBZ per 100 km. Because we do not correct for such effects, this will lead to uncertainties in the derivation of area-average rainfall rates (Joss. and Lee 1995), however, as further described in section 3.3, our analysis focuses on the areal coverage of rainfall so that these uncertainties are not expected to affect the overall conclusions.

In addition to radar reflectivity data, the radial (Doppler) velocity data is used to analyze the horizontal wind field. Radial velocities are averaged into concentric rings, each covering a range of ≈ 22 km, and Fourier analysis is applied to get the best fitting sinusoid to each ring, with the amplitude and phase corresponding to the (approximately

horizontal) ambient wind speed and wind direction.

Sounding data A total of 421 soundings are available from a variety of locations: 144 GAUS[†] radiosondes from Spanish Point (SPNT), a spit of land on the southeastern shore of Barbuda (Figure 2.1), 83 soundings from the research vessel Seward Johnson (RVSJ) and 194 dropsondes from the NSF NCAR C-130 aircraft (C130). The SPNT soundings were launched between December 7 and January 24 with a frequency of 2-4 soundings per day. The RVSJ soundings were launched from January 3 onwards, typically 6 to 8 soundings per day, while cruising an area NNE of Barbuda during January, except for a few days when the ship took up station at Antigua or stayed on the lee-side of Barbuda. The C130 aircraft released 6 to 9 dropsondes while flying free-tropospheric circles (at ≈ 4500 m) of roughly 60 km in diameter. These circles were performed twice, near the beginning and the end of almost every eight-hour flight. On RF01 (December 7) and RF16 (December 18) no full second circle was performed. All circles were flown in an area northeast of Barbuda within a 150 km range from the radar, except for RF06. The C130 dropsondes are combined into an average sounding for each circle (hereafter referred to as 'C130-C'). Combined, the soundings are distributed as follows (in terms of number of soundings per day): 2 to 6 soundings from December 7-20, 2 (occasionally 1) soundings from December 21-January 2 and 2 to 10 soundings from January 3-25.

The Spanish Point Sondes have been subjected to an automated quality control check by EOL's Atmospheric Sounding Processing Environment (ASPEN). A temperature radiation correction is applied to remove unrealistic temperature gradients due to radiation processes, and a low-pass wind filter to remove pendulum motions beneath the balloon.

[†]GPS Advances Upper-air Sounding system

Additional quality checks are applied, following analyses described in Yin and Albrecht (2000) and Sobel et al. (2004), to create a consistent dataset without data gaps below 600 hPa, corresponding roughly to the level at which C130 dropsondes were released (≈ 550 hPa). Eighteen soundings with either missing pressures at all levels, with unrealistic high relative humidities (after cloud penetration) or with gaps greater than 50 hPa, are excluded. The remaining 246 soundings are visually inspected to ensure consistency between the three datasets on any given day. The two-month average SPNT sounding does not differ much from the two-month average of all SPNT, RVSJ and C130-C soundings, and it is assumed that the dataset does not particularly emphasize the atmospheric conditions during January.

The soundings are re-gridded on a constant pressure grid starting at the surface and decreasing with a 2 hPa increment. Data is set to missing value when pressure changes in the opposite direction of the sonde motion, and data gaps smaller than 10 hPa are interpolated.

Surface-flux data Sea-surface temperature and surface-flux measurements performed by the ship (RVSJ) are available as 30 min statistics, but only for January 3 to 25. To obtain surface-flux data for the full two-month period data collected at the Integrated Surface Flux Facility (ISFF) meteorological station, located on Spanish Point, Barbuda (coincident with the sounding site), are used to estimate open-sea fluxes. These data include 5 min statistics of air temperature and relative humidity at 2 m AGL (Vaisala 50Y Humitters), pressure (Vaisala PTB220 barometer) and wind speed and wind direction at 10 m AGL (RMYoung Prop Vane) for December 4 - January 25 (53 days in total). In addition daily sea-surface temperatures, used as boundary condition of the ECMWF

IFS[‡] (Reynolds et al. 2002), are used to derive ISFF surface fluxes. This is performed using flux-profile relationships similar to the COARE 3.0 bulk air-sea flux algorithm Fairall et al. (2003).

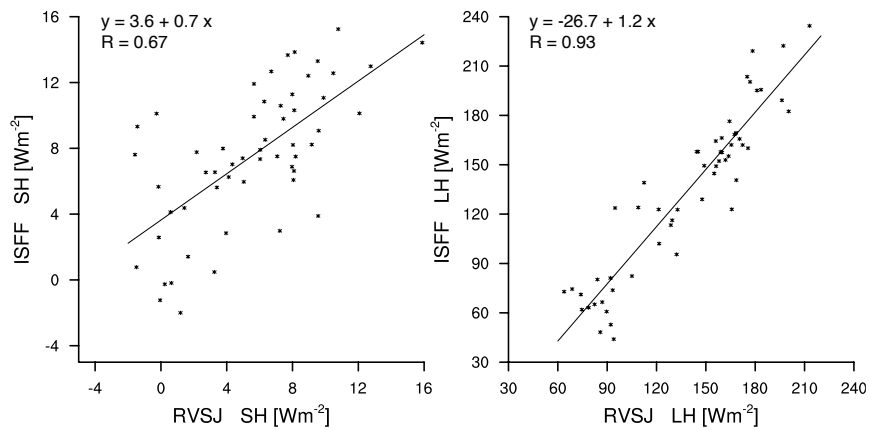


Figure 2.2: Six hour averages of the sensible heat flux (left) and latent heat flux (right) are plotted for ISFF versus RVSJ (see section 2.1.iii) using data from January 3-25 (2005), where all frequencies < 26 hours have been removed.

Differences between the ISFF and RVSJ fluxes are expected because of a strong diurnal cycle in the ISFF temperature. During the night, the ISFF sensible heat fluxes are considerably higher, because of stronger cooling of the air just above the surface (and the same SST estimate is used for both day and night), and the opposite is true for the fluxes during the day. After removing high frequency signals (< 26 hours) in temperature from the ISFF and RVSJ data, a reasonable agreement among sensible heat fluxes (given the small magnitude of the signal) and a good agreement among latent heat fluxes is obtained (Figure 2.2). To test whether remaining differences are caused by using different SST's, the fluxes for January are derived using RVSJ SST estimates instead, but changes are marginal. For these reasons we believe the ISFF provides a

[‡]European Center for Medium-Range Weather Forecasts Integrated Forecast System

useful estimate of the open-sea fluxes for the full two-month period.

Lidar data Data from the NCAR aerosol backscatter lidar, which operated at 532 and 1064 nm aboard the C130-aircraft, is used to derive cloud top height distributions. The lidar data is analyzed for all free tropospheric circles for flights RF01, RF03-19 (see also section 2.2), when the lidar was pointing at nadir. Cloud top is identified as the first return (at 1064 nm) that exceeds a given threshold, in this case 18 dB, and cloud top heights are estimated by using the measured range from aircraft, the aircraft altitude and its orientation (to account for slight offsets from nadir pointing).

b. Methodology

In our analysis, a distinction is made between the full set of radar data (I) and a subset of the radar data (II), from which scans on six days with disturbed conditions are excluded. Using the echo fraction (F), that represents the area covered by echoes on a radar scan and is used as a proxy for precipitation for reasons detailed in section 3.3, these six disturbed days are identified by the following procedure: Scans with echo fractions deviating more than three standard deviations from the mean echo fraction of dataset I ($\overline{F^I} = 0.031$), are set to missing value and the mean is recalculated ($\overline{F} = 0.023$). This procedure is repeated for scans that deviate more than three standard deviations from $\overline{F} = 0.023$. All scans set to missing value are distributed over the six days summarized in Table 2.1. Dataset II excludes all scans on these six days (354 scans) and is assumed to represent undisturbed trade-wind conditions ($\overline{F^{II}} = 0.02$). Although our analysis focuses mostly on undisturbed conditions, dataset I is used for the general overview of precipitation during RICO in section 3.

Date	\bar{f}^d	wspd [m s⁻¹]	wdir [deg]	RH [%]
12/13/2004	0.15	9.0	72	82
12/14/2004	0.13	8.5	91	93
12/15/2004	0.18	7.5	101	89
01/09/2005	0.09	8.9	70	84
01/10/2005	0.17	9.8	80	77
01/13/2005	0.08	12.7	77	81

Table 2.1: The daily average echo fraction, wind speed, wind direction (derived from radial velocity data) and mean relative humidity between 900 and 700 hPa (from the daily mean sounding) for six days during RICO identified as 'disturbed days' (section 2.5).

A third dataset (III) is created to explore relations between precipitation and meteorology. It combines dataset II with sounding and surface flux data, excluding 31 soundings and $\approx 10\%$ of surface-flux data on the disturbed six days, and focuses only on the echo fraction in the northeast segment of the radar domain, denoted by f , where most meteorological data were collected. This also eliminates a possible influence of the islands on downwind precipitation statistics. For consistency, 18 soundings (16 RVSJ and 2 C130-C soundings) released outside of the northeast segment ($\approx 60\text{-}61^\circ\text{W}$ and $17.6\text{-}18.6^\circ\text{N}$) are excluded as well, as they are notably different from soundings released within the northeast segment at approximately the same time.

The sounding, surface-flux and lidar data in III are composites based on a six hour average echo fraction over the northeast radar segment, \bar{f} . The six hour period is a compromise between the 11 hour (lag) autocorrelation period of echo fraction (the period after which subsequent rain events become uncorrelated) and the time it takes for an air-mass to advect through the northeast radar domain (≈ 3 hours). The compositing makes use of three or six categories, depending on the amount of detail that is worth showing, and the thresholds of \bar{f} are chosen such that an equal number of events is used in each

composite. For the soundings, \bar{f} is centered at the release time of each sounding and only the T , θ , q and surface pressure fields are averaged, from which other fields (RH , T_v , θ_v , θ_e) are recomputed using a 1000 hPa reference pressure. The surface-flux data are averaged over six hours, giving a total of $(53 - 6) \text{ days} \times 4 = 188$ data points, and then compared to \bar{f} during the same six hours.

All datasets are summarized in Table 2.2. The notation is as follows: echo fractions for the full and northeast radar domain are denoted by F and f , respectively. The overbar indicates a temporal average continuous in time (such as a daily average \bar{f}^d), whereas brackets denote a composite mean $\langle \bar{f} \rangle$ (an average not continuous in time). The six hour average of f is most frequently used and simply referred to as: \bar{f} .

	Dataset	Type of data	Domain	Echo fraction [-]	Area rainfall [mm h ⁻¹ / W m ⁻²]
I	Precip	radar scans [3662]	full	F $\bar{F}^I = 0.03$	R $\bar{R}^I = 0.05 / 35$
II	Precip	radar scans [3308]	full undisturbed	F $\bar{F}^{II} = 0.02$	R $\bar{R}^{II} = 0.03 / 21$
III	Composites	radar scans [3308] soundings [197] surface data [188]	NE undisturbed 6 hr average	\bar{f}	-
IV	Daily precip and winds	radar scans [3308] soundings [197]	NE undisturbed 24 hr average	\bar{f}^d	-

Table 2.2: The number of radar scans, soundings and surface data, details of the domain and the symbol for echo fraction (with its mean value) and area-average rainfall (with its mean value in mm h⁻¹ and W m⁻²) of the datasets used in section 3.1 and 3.2 (I), 3.3 (II), section 4.1-4.3 (III) and section 4.4 (IV).

2.3. Precipitation

What are typical rain-rates for shallow cumulus and are they significant? How frequently does precipitation occur? These questions are addressed by presenting precipitation statistics and related quantities. Relations between precipitation and the meteorological environment will be explored in section 4.

a. *Intensity and frequency of precipitation*

From reflectivity to pixel rain-rates The reflectivity Z_i (in $\text{mm}^6 \text{m}^{-3}$) of each radar pixel is converted to a pixel rain-rate R_i (in mm h^{-1}) using the TRMM Z - R relationship for convective rainfall near the surface: $Z = 148 R^{1.55}$. Because observations of shallow precipitation are scarce, few Z - R relationships in the literature are specifically tuned to this type of precipitation. The TRMM Z - R is chosen because it facilitates a comparison of satellite- and ground-based radar observations and leads to average rain-rates well within the range of rain-rates obtained from a variety of relations, at both high and low reflectivities. Using the TRMM Z - R , the Bragg filtering threshold of 7 dBZ corresponds to a minimum rain-rate of 0.11 mm h^{-1} , similarly 15, 20 and 25 dBZ correspond to 0.4, 0.8 and 1.6 mm h^{-1} . Z - R relationships used in two previous studies of RICO radar data are (1) $Z = 248 R^{1.75}$ (Nuijens 2005) and (2) $Z = 88.7 R^{1.52}$ (Snodgrass 2006), where the latter is derived from drop size spectra measured during one of the RICO C-130 flights. Using (1), reflectivities of 7 and 40 dBZ are converted to rain-rates that are 4 and 45% lower, respectively, than if the TRMM Z - R is used. Similarly, (2) leads to rain-rates that are 35 and 48% higher. Such differences introduce uncertainties of at least a few tens of percent when estimating the mean area rainfall during RICO, in

section 3.2.c.

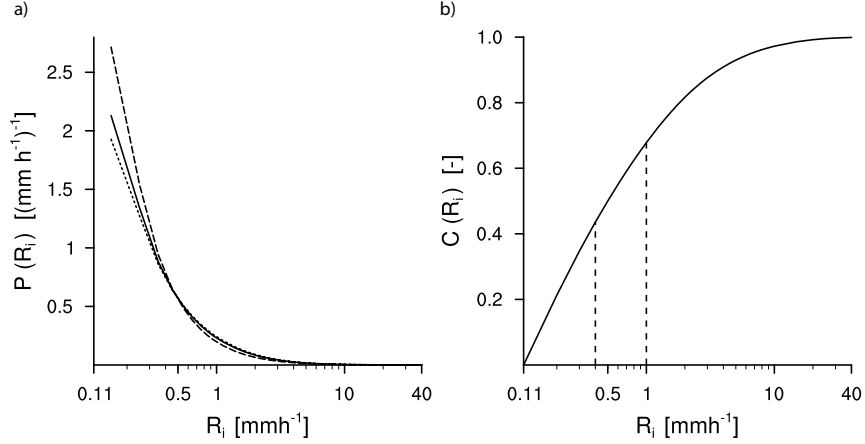


Figure 2.3: a) Probability density functions of pixel rain-rate $P(R_i)$, i.e., the probability divided by the bin width, which, for bins less than 1 mm h^{-1} can be greater than 1. The solid line is the pdf conditioned on $Z_i > 7\text{ dBZ}$ (corresponding to $R_i > 0.11 \text{ mm h}^{-1}$) for dataset I. Also shown are conditional pdf's for scans with $F < 0.03$ (dashed line) and $F > 0.03$ (dotted line). The x -axis is on a log-scale. b) The cumulative distribution of pixel rain-rates $C(R_i)$ corresponding to the solid line in a), with vertical lines indicating $C(R_i = 0.4 \text{ mm h}^{-1})$ and $C(R_i = 1 \text{ mm h}^{-1})$.

The probability density function of pixel rain-rates R_i , which is really a conditional pdf for $Z_i > 7 \text{ dBZ}$ or $R_i > 0.11 \text{ mm h}^{-1}$, is plotted as a solid line in Figure 2.3a. The probability density falls off rapidly to rain-rates of about 0.5 mm h^{-1} , with a corresponding cumulative probability of 0.5 (Figure 2.3b). The minimum detectable reflectivity by the TRMM radar is 17 dBZ , roughly $0.4 - 0.5 \text{ mm h}^{-1}$, and implies that TRMM could have detected up to half of the precipitation measured by SPol.

Frequency of precipitation A time series of echo fraction gives a first impression of the frequency of precipitation during RICO (Figure 2.4). The echo fraction is defined as:

$$F = \frac{\sum_{i=1}^N (I_i r_i)}{\sum_{i=1}^N r_i}, \quad I_i = \begin{cases} 1 & Z_i \geq 7 \text{ dBZ} \\ 0 & Z_i < 7 \text{ dBZ} \end{cases} \quad (2.1)$$

and represents the fraction of the total area that is covered with echoes, taking into account the increase of a pixel area with range due to the non-equidistant grid, where r is the distance from the radar, so that $r_i \Delta r \Delta \phi$ represents the area covered by each pixel i , with $\Delta r = 150$ m, $\Delta \phi = 0.67^\circ$ and N the total number of pixels between $r = 30$ -150 km and $0^\circ < \phi < 360^\circ$, excluding the pixels marked as land.

Aside from a few disturbed events where echo fractions largely exceed 0.1, on December 13 and 15 and January 9, smaller rainfall events are ubiquitous, which is particularly evident when zooming in on the period between December 16 and January 8 when shallow cumulus dominated the cloud field. The mean echo fraction of such undisturbed periods is roughly 0.02 (dataset II). Given a typical cloud fraction of 0.1 to 0.2 from LES studies of shallow cumulus (Siebesma et al. 2003), one can infer that on average about one tenth of the cloudy areas had rain.

The time series also indicates that precipitation was almost continuously present, with only a 0.3% probability of finding scans without echoes, increasing to 10% for scans with echoes that cover less than 10 pixels ($F \approx 0.001$). The chances of detecting precipitation anywhere in a given domain at a given time however is scale-dependent (Tustison et al. 2001) and will be further addressed in a forthcoming paper (Van Zanten et al. 2010). Using data from the space-born TRMM Precipitation Radar (PR), Short and Nakamura (2000) also describe a near constant background of shallow rainfall over the subtropical oceans, even at times of deep convection. The TRMM PR has an antenna

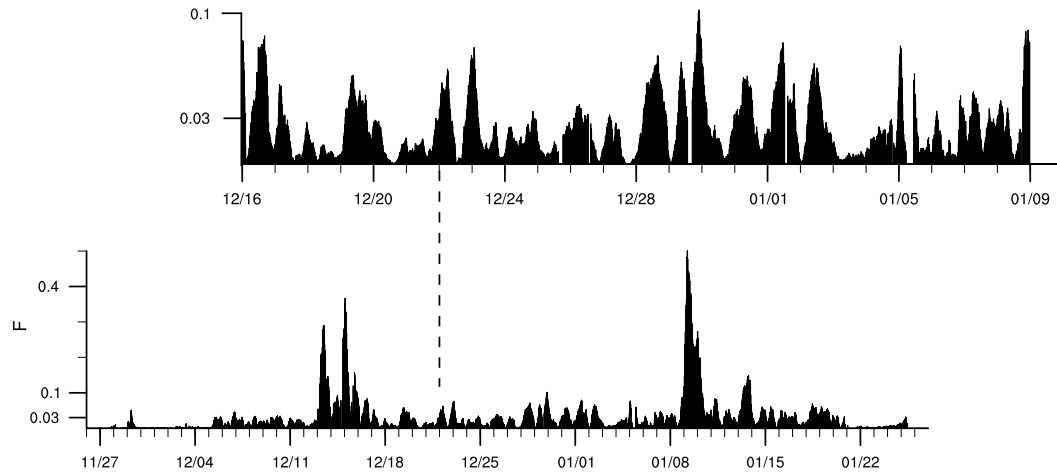


Figure 2.4: The echo fraction F of each radar scan of dataset I is plotted versus month and day during RICO. The inset zooms in on the period between December 16 and January 8.

beam that scans in cross-track direction over $\pm 17^\circ$, making a 220 km swath width from end to end, with a high vertical resolution (250 m). For the 17 TRMM overpasses during RICO, with the PR beam axis centered close to Antigua and Barbuda, surface echo fractions are comparable to values plotted in Figure 2.4, on the order of 0.03 and less. The agreement of TRMM and SPol echo fractions by means of a scatterplot however (not shown) is poor, possibly because the TRMM overpasses sample a sub-domain of SPol, but also because TRMM has a different horizontal resolution (5 x 5 km mesh) and a different sensitivity to low rain-rates (rain-rates only as low as 0.4-0.5 mm h⁻¹ can be observed, yet many observed SPol rain-rates are below this threshold, Figure 2.3).

Area-average rainfall Assuming that the rain-rates in Figure 2.3 are realistic, one may think of 1 mm h⁻¹ as a significant rain shower, certainly more intense than drizzle. In terms of the energy budget of a cloud (1 mm h⁻¹ \approx 700 W m⁻²), such a value is still

small compared to the moisture flux carried by a cloud ($\approx 5000\text{-}10000 \text{ W m}^{-2}$), where the latter is estimated by dividing a typical moisture flux of a 100 W m^{-2} by cloud core fractions of one or two percent. Whether such values have a significant impact on the structure of the cloud-topped boundary layer on larger scales is yet to be evaluated, though LES studies show that rain-rates of this order of magnitude lead to a lowering of the inversion height, as compared to non-precipitating simulations (Stevens and Seifert 2008). In terms of the contribution of precipitation to heat and moisture budgets over a larger area, one should consider the rain intensity averaged over both raining and non-raining areas.

The area-average rainfall is estimated for dataset I as follows:

$$R = \frac{\sum_{i=1}^N (I_i R_i r_i)}{\sum_{i=1}^N r_i} \quad (2.2)$$

where R_i is the pixel rain-rate of each pixel i and other symbols are as in equation 2.1.

On average the area-average rainfall for dataset I (\overline{R}^I) is about $0.05 \text{ mm h}^{-1} \approx 1.2 \text{ mm day}^{-1} \approx 35 \text{ W m}^{-2}$, where the latter is about a factor three smaller than a typical surface moisture flux (the other two Z - R relations in section 3.2(b) lead to estimates of \overline{R} that range from 0.03 to 0.07 mm h^{-1}). For individual radar scans of dataset II, R is at most $\approx 0.3 \text{ mm h}^{-1}$, which implies, given the cumulative distribution function of R (Figure 2.5), that shallow precipitation contributes a substantial part, say over 50%, of the total precipitation during RICO. In comparison, the contribution of shallow to total precipitation as estimated by TRMM ranges up to 22% (Short and Nakamura 2000). Because of resolution and sensitivity differences between TRMM and SPol, such values can not be compared directly. Also, the estimates in Short and Nakamura (2000) are based on a much larger region (the subtropical oceans) and longer time period (both

winter and summer seasons) and include only echoes with tops mostly below 3 km, whereas clouds during RICO often had tops reaching up to 4 km that likely contributed considerably to the total precipitation.

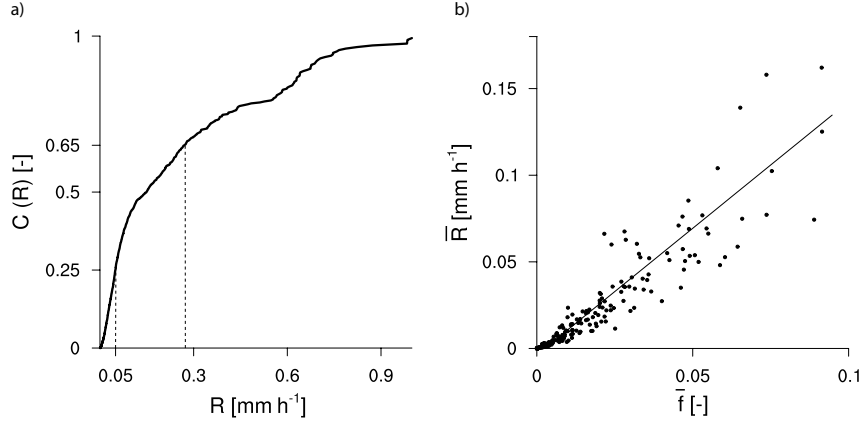


Figure 2.5: (a) The cumulative distribution function of the area rain-rate $C(R)$ using the radar scans in dataset I. (b) Six hour averages of echo fraction \bar{f} versus area rain-rate \bar{R} using dataset III.

Ideally the variability in precipitation during RICO is addressed from area-average rain-rates, which depend on both the echo fraction and the intensity of individual pixels, where the latter two are not necessarily uncorrelated. Clouds with different dimensions may produce different rain intensities, for instance, deeper clouds may rain more intensely and if these clouds have greater horizontal dimensions, and a higher cloud fraction, one may expect more intense rain-rates on scans with higher echo fractions. Similarly, shallow clouds may correspond to low echo fractions and a higher probability of weak rain-rates. The latter is somewhat evident in the previously introduced Figure 2.3, which also plots conditional probability density functions of rain-rates for scans with $F < 0.03$ (the dashed line) and $F > 0.03$ (dotted line). However, overall the pdf's suggest that a similar range of rain-rates is sampled irrespective of F . Because, as recognized in early studies (Doneaud et al. 1984), F and R are well-correlated (Figure

2.5b), we use echo fraction as a proxy for rainfall in the remaining analysis. By doing so, we circumvent the errors introduced by estimating rain-rates without applying a correction for the range (height) dependency (as discussed in section 2.a.i), and the Z - R uncertainty.

b. Temporal and spatial variability

Even for the undisturbed days a substantial variability in precipitation is seen, with the echo fraction routinely changing in just a day or less (Figure 2.4). If it is not random, what regulates this variability? May it be attributed to a diurnal cycle? And how do statistics differ for different segments of the radar domain?

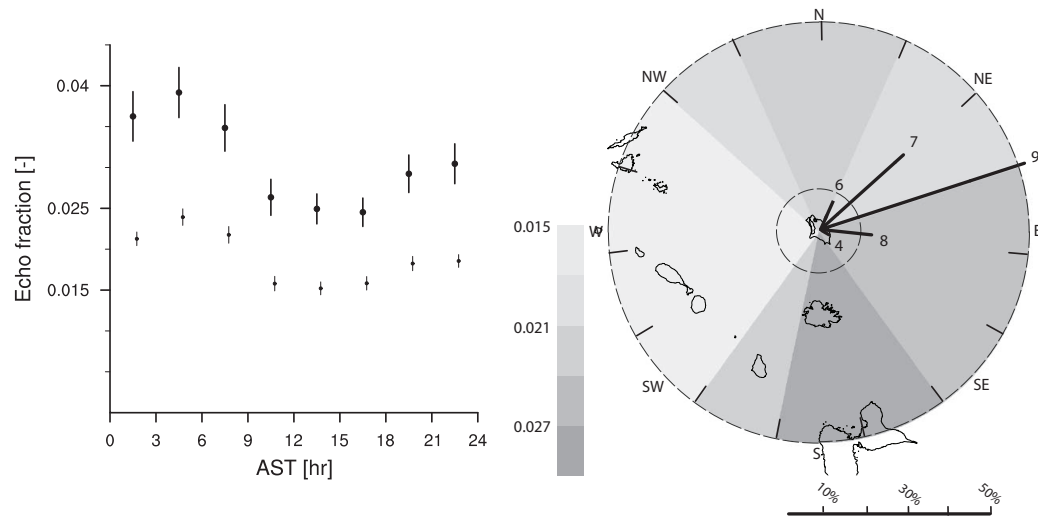


Figure 2.6: Left panel: the mean echo fraction for three hour bins is plotted against local Atlantic Standard Time (AST) with the large dot denoting dataset I and the small dot dataset II. The bars are the mean and uncertainty in the estimate of the mean (σ/\sqrt{N}), where N equals the number of scans. Right panel: the mean echo fraction (indicated by the gray scale) for 15 radar segments for dataset II. The wind rose indicates the frequency of wind direction during RICO as measured by the length of the thick horizontal lines, with mean wind speed printed at the end of each line.

Distinct diurnal cycles with an early morning maximum in precipitation have been observed in several studies on deep convection (Nesbitt and Zisper 2003; Gray and Jacobson Jr. 1977). Although it is unclear whether the mechanisms proposed for diurnal cycles apply to shallow convection, Figure 2.6 (left panel) indicates morning peaks and afternoon minima in precipitation, even for the undisturbed days. Plotted are three hour average echo fractions versus Atlantic Standard Time (AST). The larger and small dot correspond to dataset I and II. With this diurnal cycle in mind, one can indeed observe early morning peaks for some days in Figure 2.4, but the occurrence of this diurnality seems to wander somewhat.

The mean echo fraction of 15 segments of the radar domain for dataset II is plotted in Figure 2.6 (right panel). Higher echo fractions are evident in the south and southeast segments and perhaps an island shadow with less precipitation downwind of Barbuda. As indicated by the wind rose, the mean flow tended to be northeasterly, yet several periods with more east-southeasterly flow were present. The disturbed days, that are excluded from this figure, are characterized by slightly more southeasterly flow (Table 2.1) and would lead to an even more dominant maximum in precipitation south of Barbuda. The overall mean echo fraction of the (90 degree) northeast area is $\bar{f}^{II} = 0.018$, close to the mean echo fraction of the full domain $\bar{F}^{II} = 0.02$. As described in the methodology (2.b), the remainder of our study focuses on the northeast segment, which does not appear unrepresentative of the statistics of the full domain.

2.4. Meteorological environment

The variability in the meteorological environment is explored by looking at changes in the vertical structure of the lower atmosphere, various characteristics of the cloud-

topped boundary layer, as well as surface fluxes, between periods of low versus high echo fraction.

a. Atmospheric profiles

Three composite profiles of equivalent potential temperature (θ_e), the potential temperature anomaly ($\theta - \bar{\theta}$, where $\bar{\theta}$ is the mean sounding of dataset III), relative humidity (RH) and zonal wind speed (u) are plotted in the four panels in Figure 2.7. Given the small variations in θ , θ_e variations mostly reflect variations in specific humidity. The dotted, dashed and solid line can be interpreted as the vertical structure of the atmosphere during periods of little or no, moderate, and widespread precipitation. Profiles are only shown up to 600 hPa, corresponding to the level at which the dropsondes were released. The shaded areas represent the uncertainty in the estimate of the mean: σ / \sqrt{N} , where N is the number of soundings in each composite, assuming that deviations of the mean are normally distributed. The composites reveal that deeper and moister layers are present at times of more rain, with differences of up to 10% between, for instance, the three relative humidity profiles.

Based on our inspection of the θ_e profiles, the largest differences in specific humidity between periods of little (dotted) and moderate precipitation (dashed) are confined to the layer below 800 hPa. Between moderate and widespread (solid) precipitation periods, differences in specific humidity are most pronounced from cloud base (here estimated at about 950 hPa) up to 600 hPa. The sensitivity of shallow precipitation to humidity has been noted in a recent LES study, where a 2 g kg^{-1} increase in the initial profiles of free tropospheric humidity led to surface rain-rates at least five times as high (Stevens 2007). The presence of deeper and moister layers during periods with (more

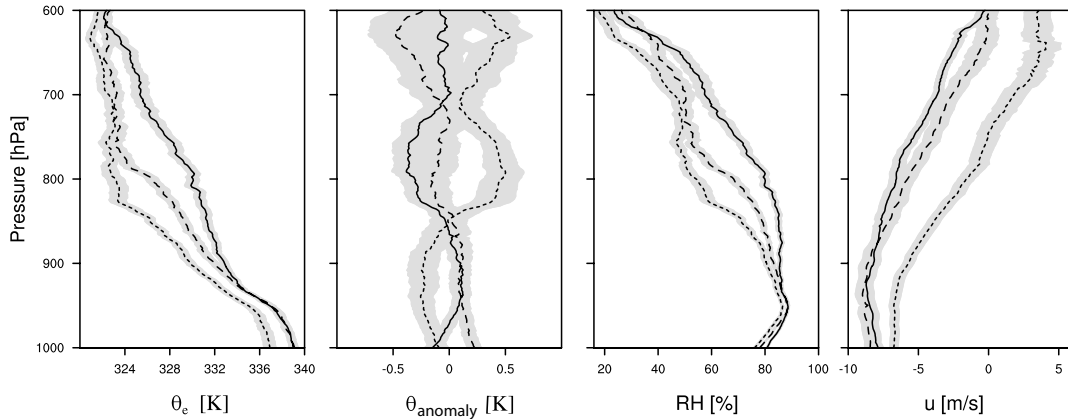


Figure 2.7: Mean profiles of (from left to right): θ_e , $\theta - \bar{\theta}$, RH and u (with the uncertainty of the mean as a shaded area) for three composites: (dotted line) $0 < \bar{f} < 0.008$ with $\langle \bar{f} \rangle = 0.003$, (dashed line) $0.008 < \bar{f} < 0.03$ with $\langle \bar{f} \rangle = 0.014$ and (solid line) $\bar{f} > 0.03$ with $\langle \bar{f} \rangle = 0.05$. About 66 soundings are used in each composite.

heavy) precipitation has also been described in observational studies of deep convection (Bretherton et al. 2004; Holloway and Neelin 2009).

The profiles of u indicate that stronger easterlies are present from the surface up to 600 hPa during periods with moderate precipitation, as compared to periods with little precipitation. The differences are far less pronounced, however, when precipitation is further enhanced (between the second and third composite). Differences in the meridional wind speed are minor and therefore not shown.

A relation between precipitation and the atmospheric thermal structure is less clear and because differences are hard to distinguish otherwise, potential temperature profiles are shown as anomalies. The profiles are overall similar, but the first composite (dotted line) shows a more stable layer near 850 hPa. Also note that the third composite (solid line) is slightly colder near the surface which may reflect cold pools created by evaporation of precipitation.

To further address the diurnal cycle for undisturbed periods, composite soundings

for the early morning (after midnight but well before sunrise) versus early afternoon soundings were compared. The results are consistent with Figure 2.7 i.e., the mornings are slightly more humid, however, the differences are not large enough to be statistically significant and therefore not shown.

b. *Deeper clouds, more rain?*

Deeper clouds with a higher (cloud-top) liquid water content may rain more, as shown in early studies of precipitating shallow cumulus (Austin 1948; Byers and Hall 1955), and more recent radar (Knight and Miller 1998) and LES studies (Stevens and Seifert 2008). Figure 2.7 indicates that at times of more rain, the environment is more humid and humidity variations are more pronounced at levels above cloud base as compared to times of little rain. Because entrained environmental air that is more humid is less effective at inducing cooling (through evaporation of liquid water) and drying, this suggests that entrainment plays an important role in promoting greater parcel buoyancies, deeper clouds, hence more rain, in an environment with moister (cloud) layers. To emphasize that moister layers are also deeper layers, the first pressure level above 950 hPa at which a relative humidity of 75% is crossed is calculated for each individual sounding of dataset III, averaged into composites based on \bar{f} and plotted as circles against the composite mean $\langle \bar{f} \rangle$ (panel (a) of Figure 2.8). Three composites (open circles) are shown to facilitate a comparison with the three composite profiles, but to reveal more detail six composites (filled circles) are shown as well, with errorbars denoting the uncertainty of the mean.

The integrated water vapor IWV over a 1000-200 hPa layer (excluding C130-C soundings for which only data with pressures greater than 600 hPa is available) increases

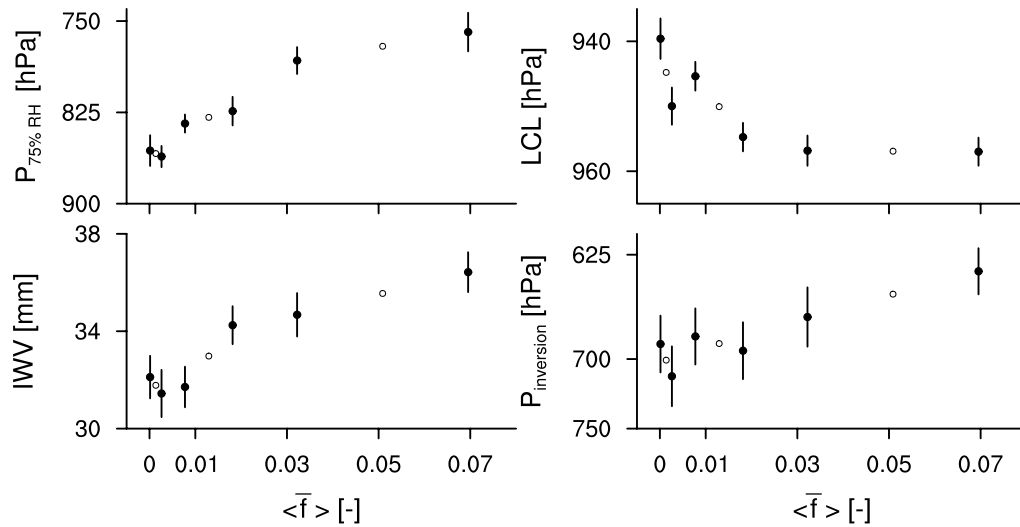


Figure 2.8: Plotted are three composites (open circles), as well as six composites (filled circles), of the pressure level at which $RH = 75\%$, the integrated water vapor IWV , the lifting condensation level LCL and the pressure level at maximum $d\theta/dz$ (the inversion), against $\langle \bar{f} \rangle$. Errorbars denote the uncertainty in the estimate of the mean. Slightly more than 30 soundings are used in each of the six composites.

substantially with echo fraction as well (panel b). Again the analogy with analyses of precipitating deep convection is worth mentioning: adopting a similar approach with sounding profiles over the island Nauru in the western tropical Pacific, Holloway and Neelin (2009) show that most of the variability in the humidity profiles, when conditioned on precipitation, is in the lower free troposphere and little in the boundary layer, which in our case is principally evident between the second and third composite profile (Figure 2.7). In their data, precipitation increases slowly with IWV up to about 65 mm, then followed by a sharp increase in precipitation for higher IWV . 65 mm is about the upper limit of IWV values during RICO, consistent with the much smaller amounts of precipitation observed in this region compared to the region of their analysis.

The lifting condensation level, calculated from the average temperature and humid-

ity over a 100 m layer above the sea-surface, is lower with increasing precipitation. This is less pronounced for high $\langle \bar{f} \rangle$, consistent with the composite profiles that indicate minor differences in specific humidity in the lower (sub-cloud) layers between the second and third composite. Composites of the level of maximum $d\theta/dz$, which can be used as an indicator of the inversion height and cloud top, shift to greater altitudes with increasing precipitation. Although the signal is small, the shift of this level, in particular at higher $\langle \bar{f} \rangle$, may indicate the importance of changes in large-scale subsidence.

Clouds are indeed deeper, with increased cloud fractions at all levels, during periods with more rain. This is most evident in lidar data from the free-tropospheric circles flown by the C130. Instead of the probability distribution of cloud-top height, the cumulative probability distribution is plotted, which, assuming that cloudy air is present at all heights below a detected cloud-top, is equivalent to the cloud fraction (Figure 2.9). The data is averaged into two composites: those circles identified as 'dry' (dashed line) and 'wet' (solid line) where the criteria for the latter are $\bar{f} < 0.02$ respectively $\bar{f} > 0.02$. The absolute cloud fraction is sensitive to the chosen lidar sensitivity threshold, particularly near cloud base where many thin clouds and significant aerosol backscatter can be expected. However, the qualitative differences between the wet and dry circles, and in particular the inferred cloud heights, do not depend on this threshold.

c. *Surface fluxes and winds*

Throughout RICO, SST's decreased gradually from roughly 300 to 299.3 K. Because precipitation at the beginning of the field campaign was slightly less prevalent than during January (Figure 2.4), there is some evidence of lower SST's corresponding to higher echo fractions, yet absolute differences are rather small. This is shown in Figure

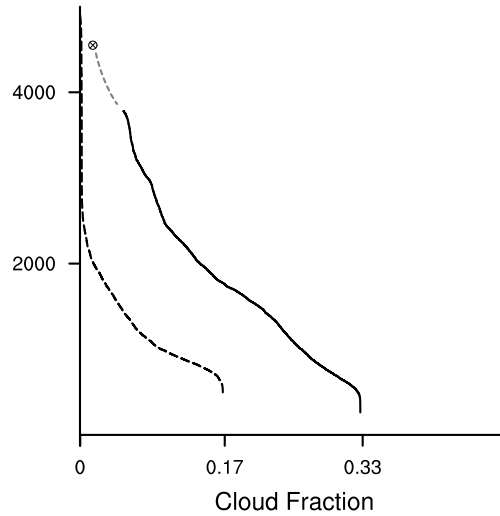


Figure 2.9: Vertical profiles of cloud fraction derived from lidar data. The solid line represents all free-tropospheric circles identified as 'wet' ($\bar{f} > 0.02$ with $\langle \bar{f} \rangle = 0.05$) and 'dry' ($\bar{f} < 0.02$ with $\langle \bar{f} \rangle = 0.007$). The asterisk is the condensate fraction for the wet circles as measured by the in situ probes of the aircraft, which is zero for the dry circles.

2.10 where three composites (open circles) as well as six composites (filled circles) of near-surface properties are plotted against $\langle \bar{f} \rangle$. Similar to the zonal wind profiles, wind speeds at 10 m increase with echo fraction, yet most pronouncedly at lower echo fractions when $\langle \bar{f} \rangle < 0.02$. It should be noted that the range of wind speeds plotted here is small, but that a similar behavior holds for daily average wind speeds, a point we return to later. Changes in wind direction are small as well, though precipitation appears more scarce for northerly winds and increases as the winds become more easterly.

The surface fluxes, and in particular the latent heat flux, remain essentially constant for $\langle \bar{f} \rangle < 0.02$, despite increasing wind speeds. This suggests that the latter offset decreasing differences in air-sea temperature and humidity. It may also indicate a tendency for stronger winds from the (south)east, advecting warmer and moister airmasses from regions with higher SST's, but overall the variability in wind direction is small. For

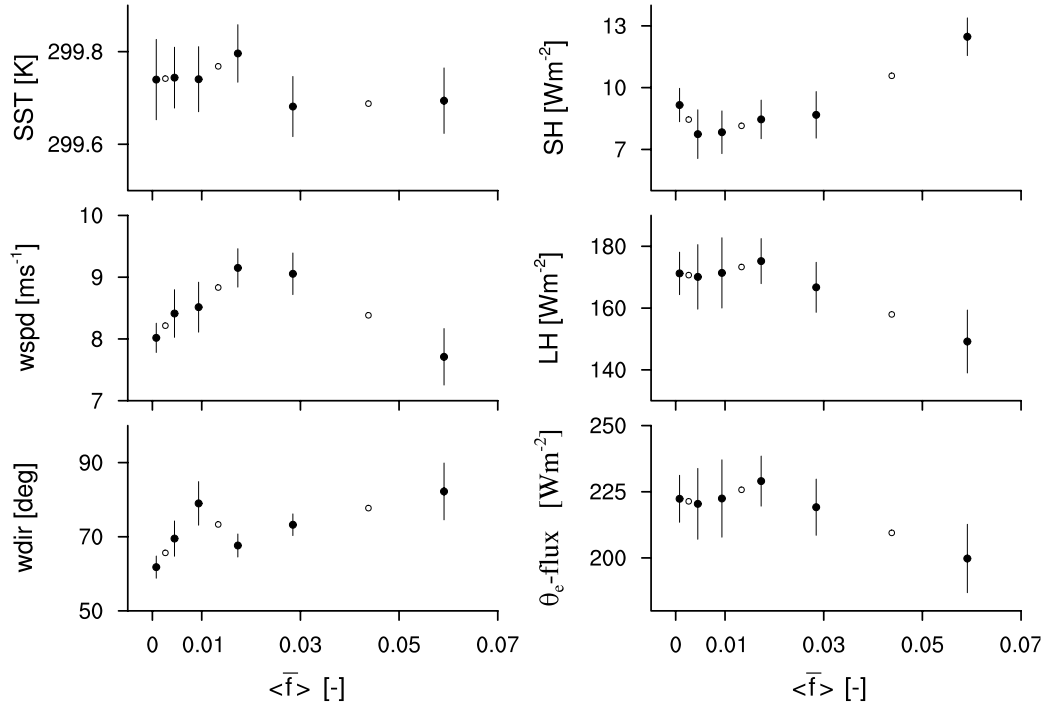


Figure 2.10: Similar as in Figure 2.8: plotted are both three and six composites of SST, wind speed, wind direction at 10 AGL (ISFF data), the sensible (SH), latent (LH) and θ_e -flux against $\langle \bar{f} \rangle$. Slightly more than 30 data points are used in each of the six composites.

higher echo fractions, $\langle \bar{f} \rangle > 0.02$, the sensible heat flux increases, despite a decrease in wind speed, and the latent heat flux decreases. This may indicate cooling and moistening due to evaporation of precipitation below cloud base, however, precipitation is not the only factor as the flux of θ_e , which is approximately conserved under evaporative cooling and moistening, also decreases.

The variability in surface θ_e fluxes appear largely regulated by subcloud layer θ_e and wind speed. The decrease in θ_e flux is only slightly weaker if SST's are held constant in the derivation of the fluxes. One may question whether the strong increase in sensible heat flux at high echo fractions is affected by using land-based temperature measurements. Although the ISFF sensible heat fluxes are indeed on average about 2-5

W m^{-2} higher than open-sea RVSJ fluxes, they overestimate low and high flux cases. Furthermore, a similar behavior is observed using only RVSJ fluxes during January.

d. *Relations between winds, humidity and echo fraction*

From the data composites, the winds and humidity in particular are seen to vary with echo fraction, but does humidity also vary with wind? To help answer this questions, relations between daily averages of the winds, echo fraction and humidity are explored by means of multi-variate scatterplots (Figure 2.11). Focusing on daily averages facilitates a comparison between the different datasets that have different temporal resolutions. The plots include a great deal of information, still we believe that showing relations in more than one dimension is worthwhile.

The left two panels in Figure 2.11 plot wind speed versus echo fraction, where the size of the dot is a measure of the mean relative humidity over a 900-700 hPa layer from soundings (averaged over all available soundings on a given day). The shading indicates ranges of wind direction based on its average (67 deg) and half a standard deviation (13 deg). The winds are derived from radial velocity data (with the same temporal frequency and spatial coverage as echo fraction), and thus are representative of the large-scale wind within the sub and lower-cloud layer. A much larger range of values is shown here compared to the ISFF composite winds in Figure 2.10. The right two panels complement the left two, yet the mean relative humidity is plotted on the y -axis and the size and thickness of the squares vary with echo fraction. The two bottom panels include days with an average echo fraction less than 0.02 ($\bar{f}^d < 0.02$), whereas the top panels include days with an average greater than 0.02.

To make it easier to discuss the apparent different behavior observed in the top versus

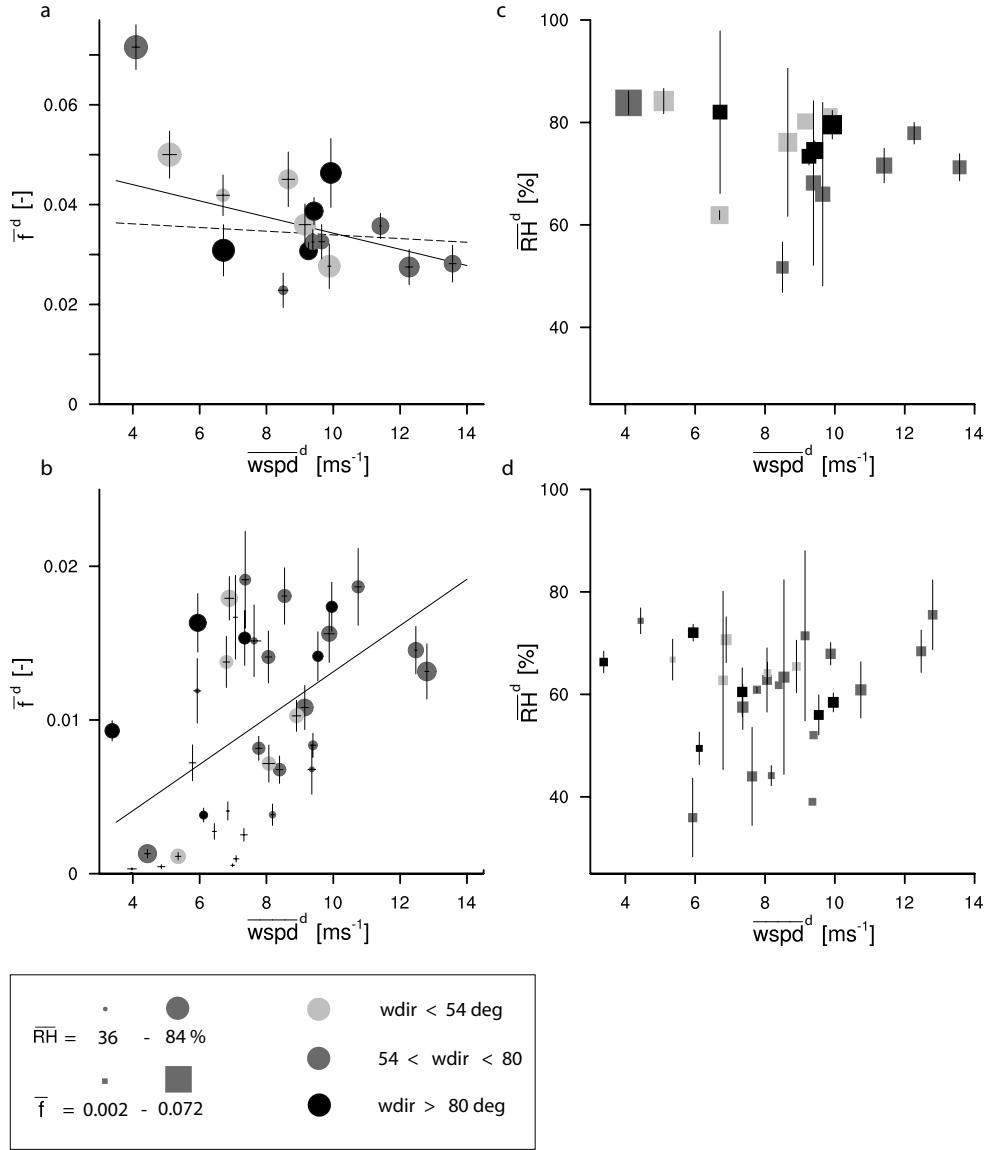


Figure 2.11: (a) Daily average echo fraction \bar{f}^d is plotted versus daily wind speed (average over a 1 km layer centered in the upper subcloud layer from SPol radial velocity data) for $\bar{f}^d > 0.02$ with vertical and horizontal bars as the uncertainty of the mean. Size of the dot varies according to the mean RH over a 900-750 hPa layer from soundings, and shading varies with the mean wind direction. In absence of soundings, rather just an error bar are plotted. The six days in Table 2.1 are excluded. (b) Same as in a, but for $\bar{f}^d < 0.02$. (c) Same as in (a) yet the size and thickness of the squares vary according to \bar{f}^d , with $\bar{f}^d > 0.02$, and the mean relative humidity is plotted on the y -axis. (d) Same as in (c) but for $\bar{f}^d < 0.02$.

the bottom panels, we may refer to the changes in meteorology with changes in echo fraction in terms of two regimes: a sparse-precipitation regime 1, in the bottom two panels, displaying variability between periods of little and moderate precipitation, and a widespread-precipitation regime 2, in the top two panels, displaying variability between periods of moderate and widespread precipitation.

For regime 1 echo fraction appears to increase with wind speed and this relation ($R = 0.51$, bottom left panel) seems to hold regardless of wind direction, though is perhaps most evident for easterly and southeasterly winds. There is some evidence that higher wind speeds correspond to higher humidities from the bottom right panel, in particular for wind directions close to average (in dark gray), yet there are some days with high humidities despite low wind speeds. A wind speed-echo fraction relation appears less evident for regime 2 ($R = -0.38$, solid regression line, top left panel) and is essentially absent if one day with $\bar{f}^d = 0.0072$ is excluded ($R = -0.12$, dashed regression line). Regime 2 clearly has the highest relative humidities, indicated by the thick dots, yet a correlation between wind speed and humidity is less evident here. Including the six days with disturbed conditions (Table 2.1) and echo fractions of 0.09 and higher, would not change this finding.

2.5. Discussion

What is the nature of the relationship between wind speed and humidity, and between wind speed and precipitation? If not wind speed, what are other possible controlling factors on precipitation? A possible mechanism through which wind speed influences humidity is through enhanced surface evaporation, which may lead to a greater population of cumulus clouds and subsequently more (upward) mixing of moisture between the

subcloud and the cloud layer, promoting the development of even deeper clouds, with higher chances of precipitation. On the other hand, weaker large-scale subsidence (less subsiding warm and dry air) can lead to a greater boundary layer depth and a more humid environment, which also promotes deeper clouds. Using (equilibrium) bulk theory, section 5.a further explains these ideas that underly our hypothesis that boundary layer humidity, hence precipitation, is regulated by subtle fluctuations in wind speed as well as subsidence. We should be mindful however because the aerosol will co-vary with the meteorological environment and may also play a role in regulating the precipitation efficiency of clouds. For instance, increasing winds can lead to higher concentrations of marine sea-salt particles from breaking waves. In section 5.b we speculate on possible aerosol effects and describe why we believe the major variability in precipitation during RICO is not controlled by the aerosol.

a. *Bulk theory*

A distinction in two regimes as introduced in section 4.d may also be used when interpreting the composite profiles and surface-flux data from a bulk perspective and is illustrated in Figure 2.12. Particularly the θ_e profiles indicate a different behavior in terms of the location of most pronounced changes in humidity between little (dotted) versus moderately (dashed) precipitating periods (regime 1) and moderately versus widespread (solid) precipitating periods (regime 2). In summary, regime 1 corresponds to higher humidities and stronger easterlies, not only near the surface but throughout the entire lower atmosphere, with a θ_e -flux that remains basically constant (Figure 2.10). In regime 2 on the other hand the variability in humidity is most pronounced at upper levels, whereas little difference in (near-surface) winds is seen and the flux of θ_e has decreased. An

increase in the inversion height is however more pronounced for these cases (Figure 2.8).

These findings support our idea that moistening is dominantly forced from the bottom part of the boundary layer (wind speed) versus the top part (subsidence). This idea may be reconciled with the observed flux behavior using bulk equilibrium theories of equatorward transport of air masses over the (subtropical) ocean by the trade winds, such as described in Betts and Ridgway (1989). In bulk theory, clouds (and precipitation) are the link between surface forcing (the surface fluxes), radiative cooling within the convective boundary layer, and subsiding tropospheric warm and dry air, which in equilibrium define the heat and moisture balance in the cloud-topped boundary layer. In view of such an equilibrium, and for simplicity assuming a constant radiative cooling rate, envision a column of air that is advected at an increasing speed in the first regime, leading to enhanced evaporation. Assuming that subsidence varies little, a heat and moisture balance with unchanging equilibrium surface fluxes can be maintained only by decreasing differences between surface and subcloud-layer temperature and humidity (the sparse-precipitation regime 1 in Figure 2.12). In the widespread-precipitation regime 2, variability in the winds is present but not dominant, and weaker subsidence may explain the observed moistening and deepening of the cloud layer, which, in equilibrium, implies lower surface fluxes.

Worth noting is that wind speed was shown to explain a significant part of daily rainfall variability in the Pacific ITCZ from four years of satellite retrieved data over 2.5 deg gridboxes in Back and Bretherton (2005). The suggested ideas through which wind speed influences precipitation (for deep convection), such as the boundary-layer quasi-equilibrium theory (Raymond 2005), are in some ways similar to the mechanisms

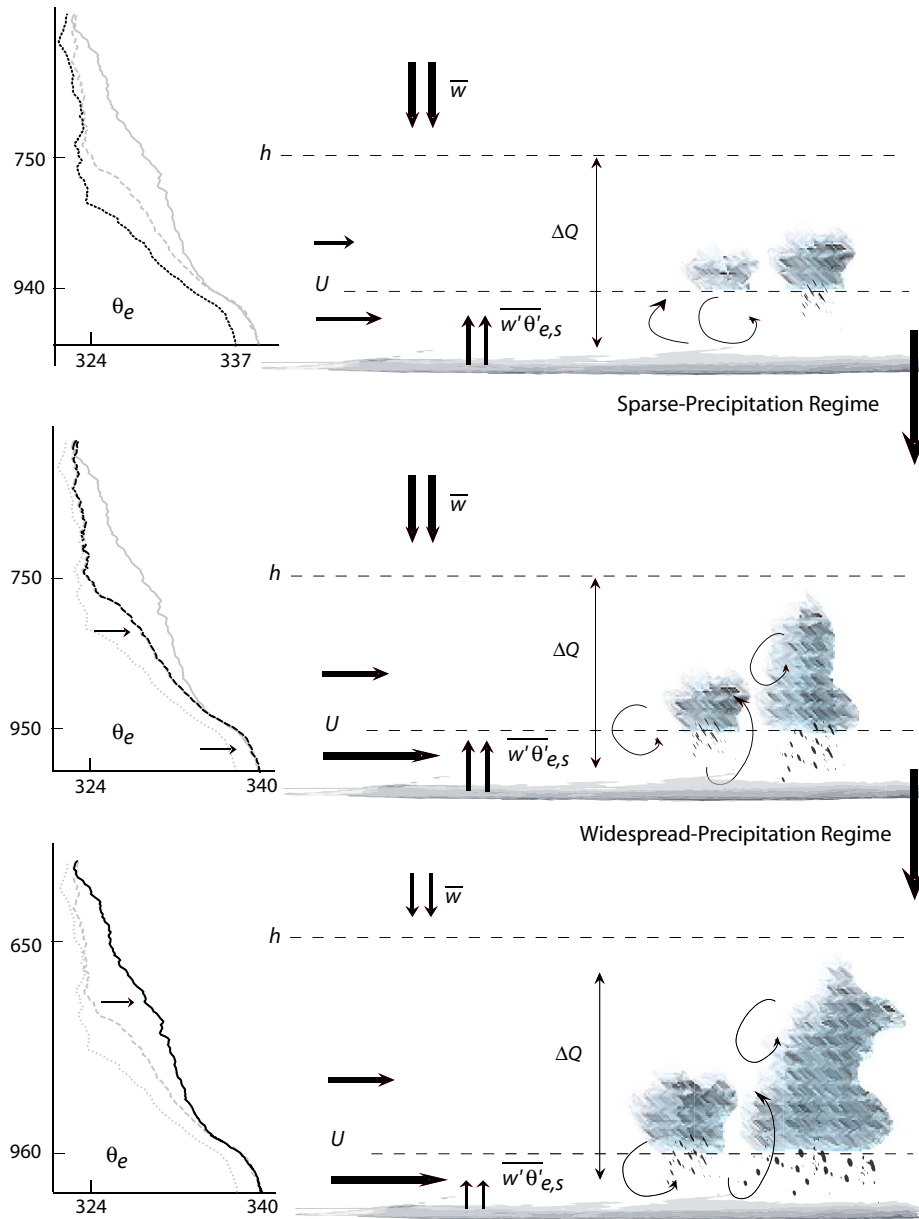


Figure 2.12: Illustration of the processes in a bulk trade-wind layer in equilibrium: wind speed (U), surface θ_e flux ($\overline{w'\theta'_{e,s}}$), subsidence velocity (\overline{w}) and the radiative flux difference (ΔQ) across the boundary layer depth (here denoted by h). Top and middle panel display composite 1 and 2 (sparse-precipitation regime), similarly, the middle and bottom panel display composite 2 and 3 (widespread-precipitation regime). θ_e profiles indicate the location of most pronounced variations in specific humidity.

proposed here for a shallow layer using bulk theory. Work is ongoing to explore the extent to which such theories are similar and provide good explanations of precipitating shallow convection.

The anomalous subsidence necessary to explain the differences between the second and first θ_e profile in regime 1 is about 0.02 Pa s^{-1} (if occurring over the course of a day), compared to 0.04 Pa s^{-1} for the third and second θ_e profile in regime 2. Because a typical subsidence rate for the Atlantic trade wind regions is about 0.05 Pa s^{-1} (Holland and Rasmusson 1973), one may infer that variability in subsidence plays a larger role in regime 2. In an effort to explore these ideas, re-analysis data from the Regional Atmospheric Climate Model (RACMO) was used, yet this proved challenging. For instance, sea-surface pressures did not respond in a systematic way to reveal a possible covariability in subsidence and the strength and direction of the mean wind field.

b. *Aerosol effects*

An enhanced contribution of sea-salt particles to marine aerosol can be expected at stronger winds from breaking of waves. This appears most evident at larger sizes, leading to more so-called giant nuclei (GN, radii roughly $> 1 \mu\text{m}$) (Woodcock 1953), though production of sea-salt particles in all sizes from $0.01 \mu\text{m}$ to $10 \mu\text{m}$, peaking at $0.03 \mu\text{m}$, has been observed as well, indicating a significant contribution of small sea-salt particles to nuclei-mode aerosol (Clarke et al. 2003). Aerosol particles with radii $> 0.2 \mu\text{m}$ during a low wind speed RICO research flight were found to be mostly sea salt, but those with radii $< 0.2 \mu\text{m}$ were ammonium sulfate (Peter et al. 2008). Yet measurements of the composition of cloud droplet nuclei in non-precipitating marine clouds from several field campaigns, including one RICO flight, indicate that preferred nuclei-

types are composed of salts (Twohy and Anderson 2008). Whether sea-salt contributed appreciably to the number of cloud condensation nuclei (CCN) for RICO in general, either directly or by coagulation or heterogeneous reactions with other aerosol particles such as sulfate, needs more investigation. From wind data, flight-averaged cloud droplet spectra near cloud base and CCN measured at 100 m for 12 different RICO flights, indeed a strong correlation between wind speed and concentration of GN is found and a much weaker correlation between wind speed and CCN (Colón-Robles et al. 2006; Hudson and Mishra 2007).

GN may accelerate collision-coalescence processes within clouds and promote warm rain formation. On the other hand, more CCN can reduce the efficiency of collision-coalescence processes (all else being equal) and slowdown warm rain formation. One of the major questions that motivated the RICO field campaign was in fact: What is the role of CCN versus GN in the fast onset of warm rain in shallow cumuli?

In studying the development of precipitation in trade wind cumulus during RICO using differential reflectivity data at S Band Knight et al. (2008) find no evidence that ultragiant aerosols initiate coalescence during rain onset, in strong contrast with a similar study for cumulus over land. Moreover, despite the strong correlation between wind speed and GN for the 12 RICO flights, Colón-Robles et al. (2006) and Hudson and Mishra (2007) find an inverse correlation between wind speed and the number of large cloud droplets near cloud base. Although generally the largest droplets form at cloud top where more liquid water is present (to the extent that droplet concentrations remain roughly constant with height), both studies take the number of large droplets as an indicator for the efficiency of warm rain formation. Hudson and Mishra (2007) also show that a factor of four variability in CCN (from 50 and 200 cm^{-3}) has the dominant influ-

ence on the number of large cloud droplets. These findings are thus consistent with the general idea that as long as CCN concentrations are low i.e., in clean maritime regions, the influence of GN on the formation of raindrops may not be critical and are in agreement with modeling studies that show that as long as $CCN < 600 \text{ cm}^{-3}$ any added GN have no appreciable effect on the onset of rain and the total precipitation on the ground (Teller and Levin 2006).

We consider these results compelling evidence that the positive wind speed-precipitation relationship found in what we have called the sparse-precipitation regime (Figure 2.11 b) is not caused by GN. To the extent that CCN scales with wind speed and rain production is more efficient in a weak-wind environment, as hypothesized by Colón-Robles et al. (2006), our data do not provide evidence for a major role of CCN in controlling precipitation i.e., we do not find an inverse wind speed-precipitation relationship. In the second (widespread-precipitation) regime no significant relationship is present at all (Figure 2.11 a) and no particular role may be attributed to either CCN or GN. The aerosol may well play a role, by influencing the intensity of precipitation or by setting the cloud depth at which rain forms, in particular for individual clouds. However, we speculate that in terms of its (large-scale) areal coverage, precipitation in the undisturbed trades is more strongly influenced by subtle variations in the meteorological environment.

2.6. Conclusions

Precipitation from shallow cumulus has been estimated using observations from a ground based radar during the two-month RICO field study, set in a typical trade-wind region, and compared to the meteorological environment measured by sounding, surface-flux and airborne lidar data. A wide range of rain-rates is observed, with one-third of the

rain-rates exceeding 1 mm h^{-1} . The contribution of shallow to total precipitation during RICO is substantial, ranging up to at least 50%. Given its minimum detectable rain-rate of 0.4 mm h^{-1} , TRMM would have missed more than half of the precipitation in regions such as these. Over larger areas, variations in rain intensity appear to have a minor influence on the area-average rainfall, compared to the area covered by precipitation. For undisturbed days during RICO, the echo fraction is typically less than 0.1, with an average of about 0.02, which implies, given a typical cloud fraction of 0.1 to 0.2, that about one tenth of the clouds are raining. A diurnal cycle in echo fraction is present, with a peak in precipitation in the early morning.

On the size of the radar domain a substantial variability in precipitation (in terms of the echo fraction) is observed. Periods with moderate precipitation, as compared to periods with little precipitation, are characterized by deeper and moister layers and stronger easterlies from the surface up to the free troposphere, but overall little change in the temperature structure and surface fluxes. Periods with more widespread precipitation reveal even higher humidities, mostly in the cloud layer and free troposphere (below 600 hPa). A clear increase in integrated water vapor is seen with increasing precipitation, as well as an increase of the inversion height. Clouds during periods of widespread precipitation reached up to 4 km, about twice that of the maximum cloud top present during periods with little precipitation.

Our analyses suggest that a more humid environment promotes deeper clouds (with a higher liquid water content) that rain more, where the humidity field itself is regulated by subtle variations in the strength of the mean wind field as well as large-scale subsidence. The observed covariability in wind speed, humidity and precipitation (similar to cases of precipitating deep convection) is considered compelling evidence that even

subtle variations in the meteorological environment are a major control on precipitation. Because these effects are subtle, and act in a way that confound expected relationships between the aerosol and precipitation, it may prove difficult to differentiate between the effects of the aerosol and the meteorological environment.

Chapter 3

The influence of wind speed on shallow cumulus convection from Large-Eddy-Simulation

Abstract

Large-Eddy-Simulation is explored to study the transient and stationary response of shallow-cumulus topped boundary layers to a sudden wind speed perturbation. To isolate wind speed effects on cloud properties, the case set-up excludes rain micro-physics and prescribes zero wind shear. Otherwise, its thermodynamic structure and large-scale forcings are typical for the sub-tropics. The surface fluxes are modeled using bulk aerodynamic formulae. Wind speed perturbations of $\pm \text{m s}^{-1}$ are applied to a reference case with a 10 m s^{-1} zonal wind. To minimize numerical errors, all cases use a Galilean transform with a velocity that equals the geostrophic zonal wind.

Results indicate that stronger winds, hence a stronger surface moisture flux, lead to a moistening of the layer, deeper clouds and an increase in the growth of the cloud layer, with differences in boundary layer depth up to a few hundred of meters after two days. The deepening results in net more drying and warming from mixing with the

free-troposphere. The moistening is present most evidently in the sub-cloud layer, but not sufficient to offset the increase in wind speed, maintaining a larger surface moisture flux. Because the surface heat flux decreases instead, due to a warming of the layer, the surface buoyancy flux and cumulus updraft velocity change little with wind speed. Cloud (core) fraction and the convective mass flux are also robust quantities. Similar results are obtained for the less-idealized Rain In Cumulus Over the Ocean (RICO) precipitating shallow cumulus case. The deepening and surface flux response appear general and independent of the detailed set-up of the cases.

3.1. Introduction

Shallow cumulus clouds, one of the dominant cloud types over subtropical oceans, are mainly driven by evaporation from the ocean surface. By moistening the lower atmosphere, these clouds significantly influence the humidity structure of air masses that are transported further into the tropics. As such, they help determine the occurrence of tropical deep convection (Tiedtke 1989; Neggers et al. 2007). The prevailing winds, the trade winds, play a crucial role not just by transporting these air masses, but by help inducing surface evaporation. Do we understand how and to what extent shallow cumulus convection, and therefore the vertical humidity structure in the trades, is influenced by wind speed?

This question is motivated by observations in a typical trade-wind region that demonstrate a positive relationship between wind speed and the area covered by rain (Figure 2.11)(Nuijens et al. 2009), suggesting that wind speed plays a major role in determining variability in shallow precipitation. The relationship between wind speed and precipita-

tion from shallow cumulus, or just wind speed and shallow cumulus, has to our knowledge never been explicitly explored in modeling and observational studies. A positive relationship is also arguable from an aerosol point of view. Stronger winds are shown to correspond to a larger concentration of sea-salt aerosol. If this leads to a larger concentration of cloud condensation nuclei, rain formation may be suppressed and one can expect a negative relationship between wind speed and precipitation (Woodcock 1953; Hudson and Mishra 2007). Because the relationship we found is not negative, we argued that aerosol effects play a minor role in controlling the occurrence of precipitation from shallow cumulus on much larger scales (*e.g.*, the scale of a GCM grid box) (Nuijens et al. 2009).

From a dynamical point of view, the relationship can be understood from the impact of wind speed on surface evaporation and hence boundary layer humidity. Via entrainment, a more humid environment promotes deeper clouds that have more cloud-top liquid water content, and hence may rain more (Stevens and Seifert 2008). Entrainment arguments have also been used to explain wind speed-precipitation relationships found in observations of deep convection (Bretherton et al. 2004; Holloway and Neelin 2009). If one pictures a column of air that is advected by the mean wind, then wind speed only enters the prognostic equations for humidity, temperature and momentum via the turbulent fluxes at the surface. The surface flux can be derived from the bulk aerodynamic formulae (Fairall et al. 2003). Here, the flux of a quantity ϕ is the product of wind speed and the difference of ϕ between the surface (denoted by s) and the sub-cloud layer:

$$\overline{w'\phi'}|_s = C_D U (\phi_s - \phi_{z1}) \quad (3.1)$$

where C_D is a surface transfer coefficient determined from similarity theory, $U =$

$\sqrt{u_{z1}^2 + v_{z1}^2}$ is the wind speed at a height $z1$ just above the surface (the wind at the surface is zero). By enhancing the surface moisture flux and moistening the sub-cloud layer, stronger winds may lead to the development of more shallow cumulus and hence more upward mixing of moisture from the sub-cloud to the cloud layer.

Interestingly, observations indicate that during periods with little to moderate amounts of rainfall, an increase in both wind speed and rain do not correspond to a significant increase in the measured surface fluxes (Figure 2.10) (Nuijens et al. 2009). Can stronger winds continue to drive an increase in surface forcing and convection, and what feedbacks play a role?

The objective of the following analysis is to gain insight into the influence of wind speed by using Large Eddy Simulation (LES). LES explicitly resolves the turbulent flow and clouds on scales of tens of meters for a given set of large-scale forcings. Considering the role of shallow convection in the modification of air masses while advected towards the tropics, our focus here is not only on the initial response to a perturbation in wind speed, but also on how such a perturbation is reflected in the vertical structure of an air mass after it has reached stationarity (the equilibrium response). The strategy and cases used for our simulations are detailed in section 2. The results of a typical shallow cumulus case are explained and discussed in section 3. The influence of wind speed perturbations is studied in section 4 and 5 and our main conclusions are discussed in section 6.

3.2. Simulation set-up

a. Case specifications

Simulations are performed for three case studies: $S_{8.5}$, $S_{7.5}$ and RICO (Table 3.1). Each case uses initial temperature, humidity and wind profiles and constant large-scale forcings that are typical for the sub-tropics and lead to the development of typical cumulus-topped boundary layers. The case set-up follows that used by Gilles Bellon (manuscript in preparation).

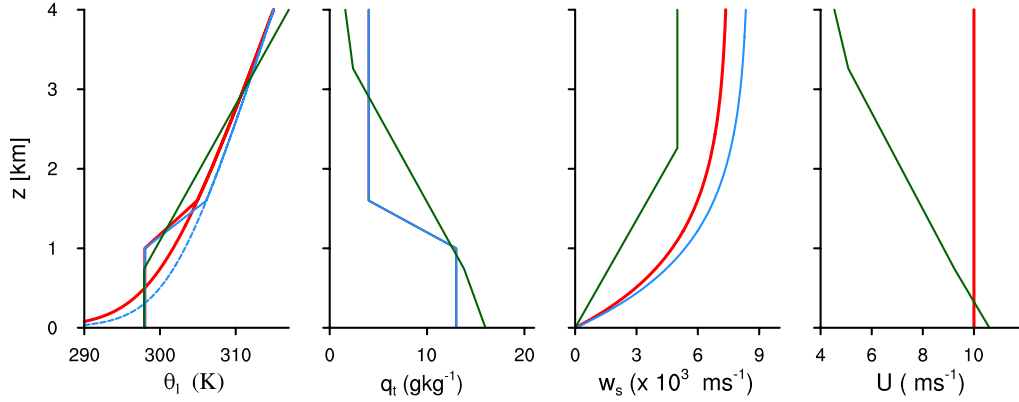


Figure 3.1: Initial profiles of liquid water potential temperature θ_l , specific humidity q_t , subsidence velocity w_s and absolute wind speed $U = \sqrt{(u^2 + v^2)}$ for case $S_{8.5}$ (red), $S_{7.5}$ (blue) and RICO (green). $S_{8.5}$ and $S_{7.5}$ have the same q_t profile (in blue). Dotted lines indicate the free tropospheric profile $d\theta_l/dz(z) = Q_r/w(z)$.

The two cases $S_{8.5}$ and $S_{7.5}$ prescribe zero wind shear and exclude rain micro-physics, hence they are more idealized than the RICO case. $S_{8.5}$ and $S_{7.5}$ differ only in the amount of subsidence that is prescribed. The subsidence velocity takes an exponential shape:

$$\bar{w}(z) = \bar{w}_0[1 - e^{-z/H}] \quad (3.2)$$

where w_0 is the base subsidence velocity and H a scale height of 1000 m (Figure 3.1

and Table 3.1). The radiative cooling rate Q_r is constant. The temperature profile in the free troposphere follows from the balance between subsidence warming and radiative cooling:

$$d\theta_l/dz(z) = Q_r/w(z) \quad (3.3)$$

The boundary layer at the start of simulation $S_{8.5}$ (blue) and $S_{7.5}$ (red) is well-mixed in temperature and humidity up to $z = 1000$ m and topped by an inversion that extends to $z = 1600$ m (Figure 3.1). The q_t profile is the same for both $S_{8.5}$ and $S_{7.5}$ and constant at 4g kg^{-1} in the free troposphere. The zonal wind speed is constant with height: $u = u_g = 10\text{ m s}^{-1}$ ($v = v_g = 0\text{ m s}^{-1}$). Surface fluxes are calculated using the bulk aerodynamic formulation (Eq. 3.1) using a prescribed sea surface temperature (SST). Horizontal advection of temperature and humidity is ignored. Simulations are performed on a domain of $12.8 \times 12.8 \times 5$ km with a resolution of 50 m in the horizontal and 25 m in the vertical, with periodic boundary conditions. Time stepping is done with a Runge-Kutta-3 scheme using a 1 second time increment.

The $S_{8.5}$ and $S_{7.5}$ cases use a Galilean transform to lower CFL numbers and reduce numerical dissipation (Appendix A). Because there is zero wind shear in the initial wind profiles, the Galilean wind equals the geostrophic wind being either 5, 10 or 15 m s^{-1} . This minimizes errors introduced by differences in advection between the cases. Differences in shear do develop in the sub-cloud layer during the course of the simulation, which could impact numerics, because the flow close to the surface moves at different speeds. We performed the same simulations with a different CFL number, which did not substantially impact the cloud statistics. As such, we believe that our results are not the result of numerical artifacts.

The initial temperature, humidity and wind profiles for the GCSS RICO intercom-

parison case on precipitating shallow cumulus case are based on observations of a three-week undisturbed period in the trades. Horizontal advection Q_q , Q_{θ_l} , subsidence \bar{w} and radiation Q_r are based on a RACMO (Regional Atmospheric Climate Model) Hind-Cast. RACMO uses the same physical parameterizations as the ECMWF integrated forecast system (IFS). RACMO simulations are performed for the RICO research area (61.46W, 17.97N) for the months of December 2004 and January 2005. The prescribed cloud condensation nuclei concentration N_c equals 70 per cc (Van Zanten et al. 2010). The RICO case uses a Galilean transform with a velocity that is the vertical average of the geostrophic wind speed. Because there is wind shear in this case, the Galilean transform noticeably impacts cloud and precipitation statistics, discussed in Appendix A. However, the RICO case is here mainly used to support and generalize the overall results of $S_{8.5}$ and $S_{7.5}$.

b. Strategy

Within the current set-up, the $S_{7.5}$ and $S_{8.5}$ simulations appear Lagrangian, wherein an air mass moves along a trade-wind trajectory. However, changes in sea surface temperature and in subsidence velocity along the trajectory are ignored. This allows us to isolate wind speed effects first.

The $S_{8.5}$ and $S_{7.5}$ cases are initialized with a 10 m s^{-1} wind speed. After stationarity is reached *i.e.*, the temperature and humidity profiles are roughly constant with time, the wind speed is perturbed by either + or - 5 m s^{-1} and the simulations are continued for two more days. For the RICO case we follow a different approach. It is run for three different wind speeds separately and for a shorter simulation period.

The $S_{8.5}$ and $S_{7.5}$ cases do not include rain micro-physics. Our choice to do so re-

quires an explanation, given that a relationship between wind speed and precipitation from observations motivated this study in the first place. Our main goal is to first establish the wind speed-convection hypothesis that was introduced in section 1 and that we repeat shortly: a relationship between wind speed and precipitation merely reflects the influence of wind speed on the amount and the mean depth of clouds. Precipitation in simulations such as these also still exhibits a somewhat worrisome sensitivity to the numerical and microphysical representation of the flow (Appendix A). Especially if precipitation effects are subtle, numerical errors may falsely influence the results. By excluding precipitation, we thus discard interesting feedbacks that it may have on, for instance, the surface fluxes by evaporation below cloud base. However, because recent studies have demonstrated a clear relationship between cloud depth and precipitation (Knight and Miller 1998; Stevens and Seifert 2008), we may still guess the overall effect of wind speed on precipitation.

Case	$S_{7.5}$, $S_{8.5}$		RICO	
Forcings				
w (m s ⁻¹)	$w_0^{(1)} = 7.5, 8.5 \cdot 10^{-3}$		$-2.2 \cdot 10^{-6} z$	$z < 2260$
			$-5 \cdot 10^{-3}$	$z > 2260$
H (m)	1000		-	
Q_r (K d ⁻¹)	2.5		$2.5^{(2)}$	
Q_q (g kg ⁻¹ s ⁻¹)	-		$-1.2 \cdot 10^{-5}$	$z = 0$
			$4 \cdot 10^{-6}$	$z = 2980$
u_g (m s ⁻¹)	10		$-9.9 + 2 \cdot 10^{-3} z$	
v_g (m s ⁻¹)	0		-3.8	
N_c (m ⁻³)	-		$70 \cdot 10^6$	
Initial and boundary conditions				
SST (K)	300		299.8	
q_t (g kg ⁻¹)	13	$z < 1000$	16	$z = 0$
	4	$z \geq 1600$	13.8	$z = 740$
			2.4	$z = 3260$
			1.8	$z = 4000$
θ_l (K)	298	$z < 1000$	297.9	$z < 740$
	⁽³⁾	$z \geq 1600$	312.7	$z = 3260$
			317	$z = 4000$
Domain and resolution				
Δt (s)	1		2	
$\Delta x, y, \Delta z$ (m)	50, 25 ⁽⁴⁾		100, 40	
n_x, n_y, n_z (-)	256 x 256 x 190		128 x 128 x 125	
domain size (km)	12.8 x 12.8 x 5		12.8 x 12.8 x 5	

Table 3.1: The initial and boundary conditions, forcings and other numerical specifications for the simulations $S_{8.5}$, $S_{7.5}$ and RICO. Details and explanation of the variables is given in the text. ⁽¹⁾ $w(z) = w_0(1 - e^{-z/H})$, ⁽²⁾ $Q_r + Q_{\theta_l}$, ⁽³⁾ $d\theta_l/dz(z) = Q_r/w(z)$, ⁽⁴⁾ stretched grid at $z > 4$ km.

3.3. Results

a. Stationary solution for the reference cases

The $S_{8.5}$ and $S_{7.5}$ reference cases with a 10 m s^{-1} wind speed (U_{10}) are run for 60 hours until stationarity is reached (Figure 3.2). Stationarity here implies that the vertical profiles do not change noticeably anymore and surface fluxes are constant with time. At this point both cases have developed a typical cumulus-topped boundary layer with a thermodynamic structure that is very similar except for the depth of the layer, that is 2.2 km for $S_{7.5}$ and 1.5 km for $S_{8.5}$. The stronger subsidence case $S_{8.5}$ leads to cumuli that are BOMEX-like (Siebesma et al. 2003), or even somewhat shallower. The $S_{7.5}$ case with 1 mm s^{-1} less subsidence leads to much deeper clouds. Clouds also continue to grow during the course of the simulation. This demonstrates just how sensitive these clouds are to small changes in subsidence.

Because the boundary layer is deeper for $S_{7.5}$ more dry and warm air is mixed down. This has led to small differences in the vertical profiles that are mainly evident for humidity, with a less humid sub-cloud layer, hence a somewhat larger surface moisture flux. Note that the sensible heat flux at the surface is close to zero (a result of the difference in surface and sub-cloud layer temperature being zero). Because the moisture flux is large, the surface buoyancy flux is still positive and we can consider the layer to be convectively driven.

In a stationary state, the prognostic equations of liquid water potential temperature θ_l , humidity q_t and the zonal and meridional winds u and v may be written as:

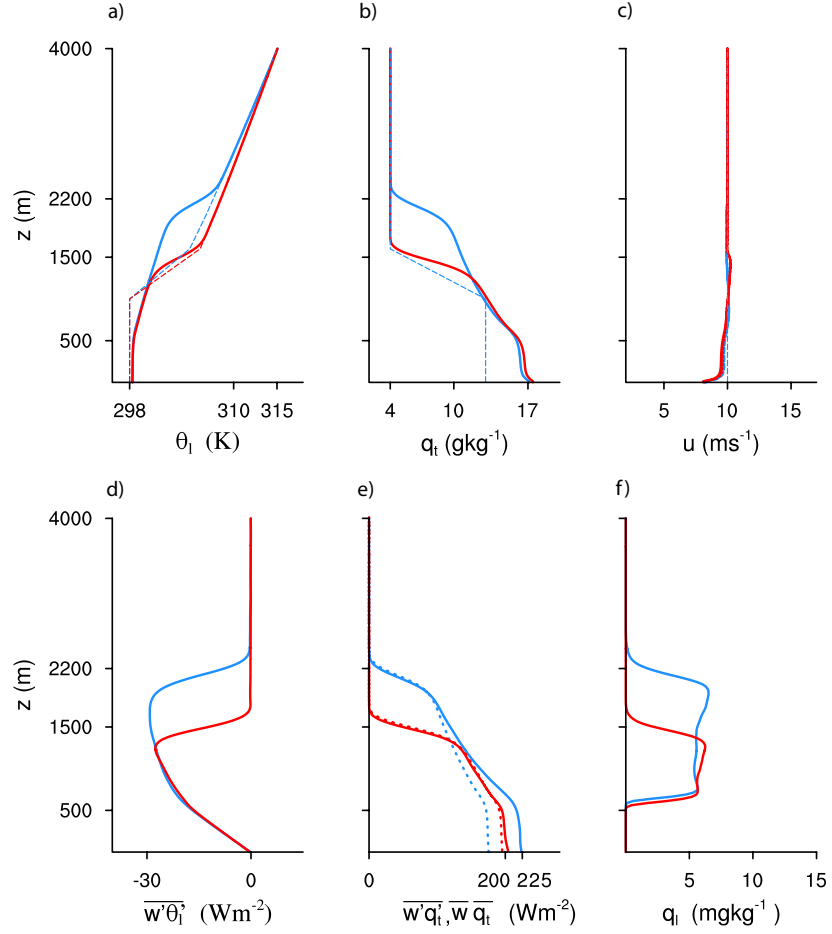


Figure 3.2: Profiles of liquid water potential temperature, specific humidity, zonal wind speed, the turbulent heat flux $\overline{w'\theta'_l}$, turbulent moisture flux $\overline{w'q'_t}$ and liquid water q_l for simulations of $S_{7.5}$ averaged over hour 52-60 (blue solid) and of $S_{8.5}$ averaged over hour 52-60 (red solid). Dotted lines in the moisture flux profiles correspond to the (negative of) the large-scale drying flux $\overline{w\bar{q}}$.

$$0 = \frac{\partial \overline{\theta}_l}{\partial t} = -\overline{w} \frac{\partial \overline{\theta}_l}{\partial z} - \frac{1}{\overline{\rho} c_p T} \frac{\partial \overline{F_r}}{\partial z} - \frac{1}{\rho_0} \frac{\partial (\rho_0 \overline{w'\theta'_l})}{\partial z} \quad (3.4)$$

$$0 = \frac{\partial \overline{q}_t}{\partial t} = -\overline{w} \frac{\partial \overline{q}_t}{\partial z} - \frac{1}{\rho_0} \frac{\partial (\rho_0 \overline{w'q'_t})}{\partial z} \quad (3.5)$$

where the over bars denote an average over the LES domain and large-scale horizontal

advection is ignored. $\overline{F_r}$ is the net radiative flux and \overline{w} is the subsidence velocity. Phase changes are accounted for by using θ_l and q_t . The last term on the right hand side of each equation represents the (vertical) turbulent flux divergence, which depends on the nature of the flow. All other terms depend on both the nature of the flow and on prescribed large-scale forcings.

In stationarity, large-scale drying due to subsidence balances turbulence moistening at each height (the two terms on the rhs of Equation 3.5). Similarly, warming due to subsidence and turbulence balances radiative cooling. To derive the large-scale drying flux F_q that results from subsiding motion \overline{w} working on the humidity gradient $d\overline{q}/dz$, we may write:

$$\begin{aligned} \overline{w} \frac{\partial \overline{q}}{\partial z} &= \frac{\partial(\overline{w} \overline{q})}{\partial z} - \overline{q} \frac{d\overline{w}}{dz} \\ \frac{dF_q}{dz} &= \frac{\partial(\overline{w} \overline{q})}{\partial z} + \overline{q} \overline{D} \\ \int_z^0 \frac{dF_q}{dz} dz &= \int_z^0 \frac{\partial(\overline{w} \overline{q})}{\partial z} dz + \int_z^0 \overline{q} \overline{D} dz \\ F_q(z) &= F_q(0) + \overline{w} \overline{q}(0) - \overline{w} \overline{q}(z) + \int_z^0 \overline{q} \overline{D} dz \end{aligned} \quad (3.6)$$

from which F_q at any z can be calculated (D denotes the divergence). To compare the turbulent and large-scale flux in the cloud and sub-cloud layer, we here use that $F_q(z \geq h) = \overline{w'q'}(z \geq h) = 0$, where h is the boundary layer depth. Note that in the remainder of this chapter, we use the notation $\overline{w} \overline{q}$ to denote the large-scale drying flux F_q at any height, even though these are principally not the same.

In Figure 3.2e) $\overline{w} \overline{q}$ (dotted lines) is compared with the turbulent moisture flux $\overline{w'q'}$ (solid lines). For $S_{8.5}$ $\overline{w} \overline{q}$ almost exactly balances the turbulent flux $\overline{w'q'}$ at all heights, including at the inversion. This implies a zero boundary layer growth and the case can be considered as truly stationary. This is not true for $S_{7.5}$ whereby the two fluxes do not

match in the cloud and sub-cloud layer. How close to stationarity a simulation is can be measured by the differences in the flux divergences *i.e.*, if the flux divergences at any height are equal, stationarity is reached. For $S_{7.5}$ this is satisfied for the sub-cloud layer at least, and will be satisfied in the cloud layer as well if the simulation is continued for two more days (Figure 3.4c).

b. *Transient response to a wind speed perturbation*

As a result of the stationary state, surface fluxes are roughly constant since hour 48 for both $S_{7.5}$ and $S_{8.5}$. A wind speed perturbation of $+5 \text{ m s}^{-1}$ (U_{15}) and -5 m s^{-1} (U_5) is applied at hour 60 and all simulations including the 10 m s^{-1} reference case U_{10} are continued for two more days. Note that a sudden 'shift' of the wind speed implies an increase or decrease in both the actual wind speed u, v as well as its prescribed geostrophic component u_g, v_g , so that the wind perturbation only impacts the surface fluxes directly. $S_{7.5}$ and $S_{8.5}$ overall behave very similarly, also after a wind speed perturbation, therefore only results for $S_{7.5}$ are shown hereafter.

The surface moisture flux LH and buoyancy flux B respond instantly to the perturbation (Figure 3.3). Comparing for instance U_{15} with U_{10} , a moistening of the sub-cloud layer takes place. Note that this immediately leads to a small recovery of the surface moisture flux. The moistening lowers the lifting condensation level, which allows a greater number of updrafts to reach saturation. As a result cloud fraction cc increases. Because the surface heat flux SH is zero initially it does not change immediately with the perturbation. However, the increased number of updrafts that overshoot cloud base and sink back into the sub-cloud layer enhance the entrainment of potentially warmer and drier air from the cloud layer. Having a closer look, it can be seen that it takes about

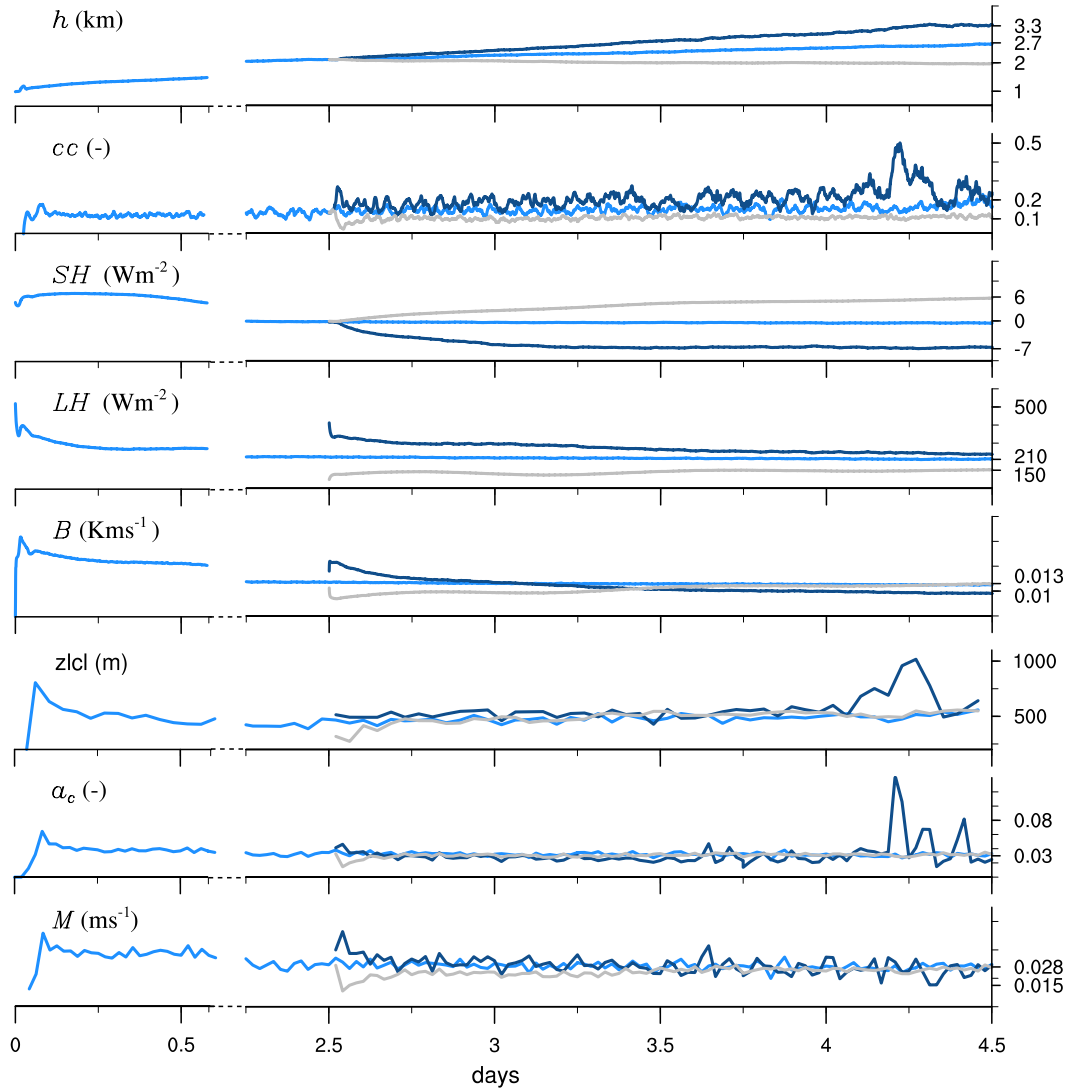


Figure 3.3: Time series before and after the wind speed perturbation for case S_{8.5}. Panels show (from top to bottom): the boundary layer height h , the fraction of cloudy columns cc , the surface sensible heat flux SH , the surface latent heat flux LH , the surface buoyancy flux B and the mass flux at cloud base M for simulations U₁₀ (blue), U₅ (grey) and U₁₅ (dark blue).

an hour before the warming due to entrainment is effectively felt close to the surface and SH decreases. Also note that the opposite happens in U₅, a reduction in entrainment of

warm air takes place (decreasing $\overline{\partial w' \theta'_i} / dz$) so that radiative cooling dominates and the surface heat flux increases instead.

The larger moisture and buoyancy flux lead to deeper clouds as reflected by the boundary layer growth that deviates after a few hours. Substantial differences in boundary layer depth are therefore present after 4.5 days of simulation. The differences are up to 600 m, but larger in the $S_{7.5}$ case (compared to the $S_{8.5}$ case) because boundary layer growth is not zero. For $S_{8.5}$, the differences in boundary layer depth are on the order of 300-400 m. That clouds are deeper is evident from Figure 3.4. Because clouds have irregular shapes and may not obey a maximum overlap rule, the total number of cloudy columns within the LES domain, defined as cc , can differ between the three wind speed cases. However, cloud fraction at cloud base in fact differs little (Figure 3.4e and k).

c. Towards a new equilibrium

The vertical structure after 4.5 days of simulation reveals that the entire layer has warmed and moistened at stronger winds (Figure 3.4.a and b). Because the layer has deepened as well, which is associated with more dry and warm air being mixed down, moistening in the cloud layer has been evidently less than in the sub-cloud layer. This increases the difference between sub-cloud- and cloud layer humidity and temperature. Through entrainment of cloud layer air into the sub-cloud layer, the deepening and associated drying and warming is also felt at the surface. Except for the initial perturbation, the surface fluxes respond more indirectly to convection, as they feel changes in sub-cloud temperature and humidity due to removal of sub-cloud layer air by the convective mass flux and entrainment of air from the cloud layer. These processes (mass flux and entrainment) are therefore crucial in determining the equilibrium surface fluxes.

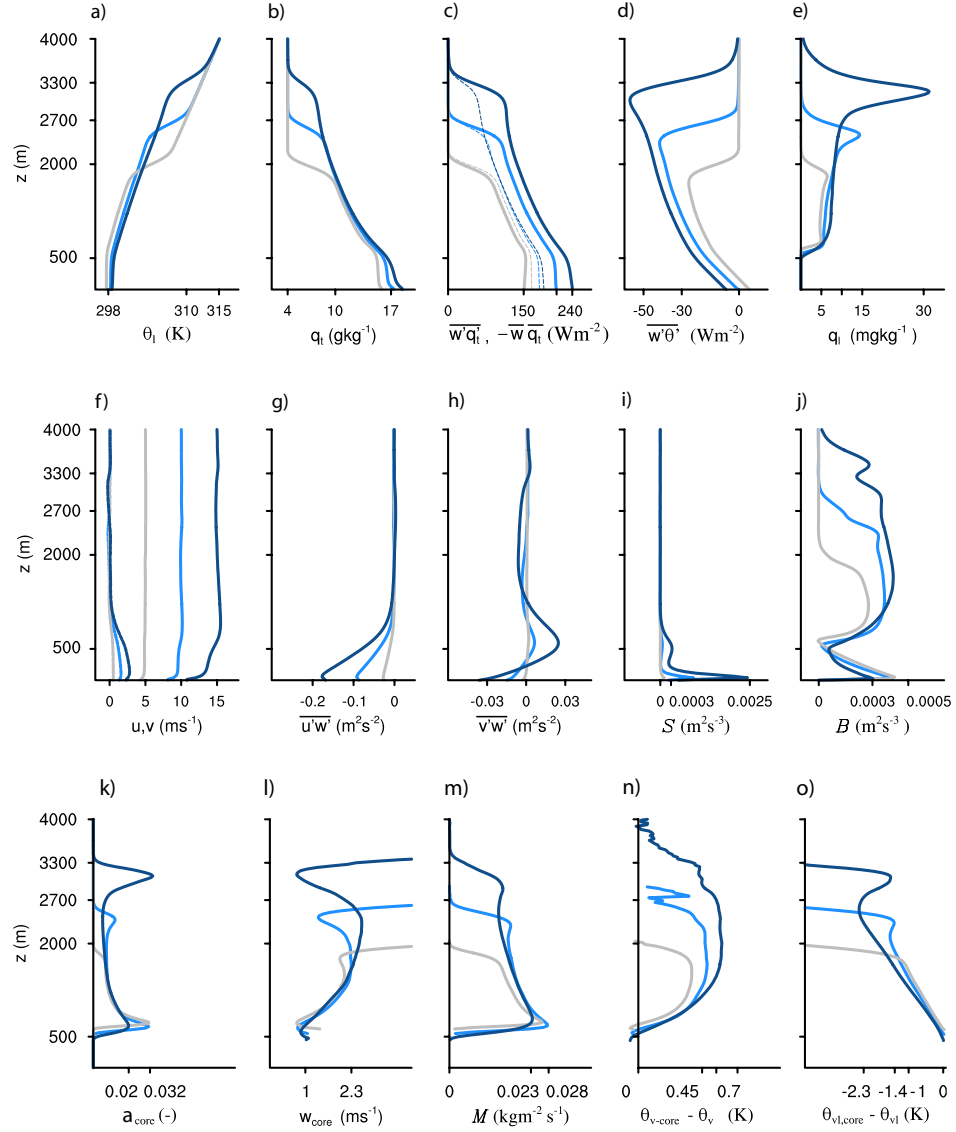


Figure 3.4: Profiles of (a) liquid water potential temperature, (b) specific humidity, (c) the turbulent moisture flux $\overline{w'q'_l}$, (d) the turbulent heat flux $\overline{w'\theta'_l}$, (e) liquid water q_l , (f) zonal and meridional wind speed u, v , (g, h) the momentum fluxes $\overline{u'w'}$, $\overline{v'w'}$, (i, j) shear S and buoyancy B production of turbulent kinetic energy, (k) cloud core fraction cc_{core} , (l) cloud core vertical velocity w_{core} , (m) mass flux M , (n) the excess in virtual potential temperature ($\theta_{v,core} - \overline{\theta}_v$) and (o) liquid water potential temperature deficit ($\theta_{v,l,core} - \overline{\theta}_{v,l}$). Profiles are averaged over hour 100-108 for U_5 (grey), U_{10} (blue) and U_{15} (dark blue). Dotted lines in the moisture flux profiles correspond to the (negative of) the large-scale drying flux $\overline{w}\overline{q}$ (see Equation 3.6).

The turbulent flux profiles indicate that the boundary layer is close to having reached stationarity for each case (Figure 3.4.c and d). The moisture fluxes at the surface balance the fluxes at the top of the sub-cloud layer, resulting in zero net moistening within the sub-cloud layer. In the cloud layer, there is a net moistening due to the divergence of $\overline{w'q'}$, but this is balanced by the divergence of the large-scale drying flux $\overline{w}\overline{q}$ (dotted lines in Figure 3.4.c). The heat flux divergence in the sub-cloud layer is balanced by the radiative cooling rate, which is prescribed. Hence, the heat flux divergence is the same for each case. The warming due to large-scale subsidence adds to the heat balance in the cloud layer, so that the turbulent flux divergence is smaller there. Boundary layer growth for U_{10} and U_{15} is non-zero (Figure 3.3), because at the inversion $\overline{w'q'} > \overline{w}\overline{q}$ (Figure 3.4.c). Hence no true equilibrium is reached for these cases.

One interesting result, evident in both the time series as the profiles, is that each case maintains a different surface heat and moisture flux. This is opposite to what we inferred from observations in Chapter 3, from which we hypothesized that the moistening and warming of the sub-cloud layer had been enough to completely offset the change in wind speed (Equation 3.1). Another interesting result is that the surface buoyancy and mass flux vary little between each wind speed case, although a somewhat different behavior appears to be present for U_{15} , which has a lower buoyancy flux and lower mass flux at cloud base.

3.4. The buoyancy and mass flux response

An obvious answer to the question why the surface buoyancy flux changes little with wind speed is the opposite response of the surface fluxes. A closer look at the sub-cloud layer budget also reveals that in equilibrium, the divergence of the buoyancy flux in the

sub-cloud layer ($\overline{dw'\theta'_v}/dz$) is constrained by the radiative cooling rate Q_r :

$$0 = \frac{d\theta_v}{dt} = -\frac{\overline{dw'\theta'_v}}{dz} + Q_r \quad (3.7)$$

If the buoyancy flux at the top of the sub-cloud mixed-layer (η) is modeled as a fixed fraction $\kappa = -0.2$ of its surface value $B = \overline{w'\theta'_{vs}}$, we can rewrite this balance to:

$$\frac{(1 + \kappa) B}{\eta} = Q_r \quad (3.8)$$

Assuming that Q_r and κ do not change with a wind speed perturbation of $\delta = \delta U$:

$$\frac{\delta B}{B} = \frac{\delta \eta}{\eta} \quad (3.9)$$

i.e., if η changes little with wind speed, then B changes little. η can be considered close to cloud base height or the lifting condensation level z_{LCL} . The latter changes little (Figure 3.3) because the sub-cloud layer both warms and moistens with wind speed, maintaining roughly the same relative humidity and lifting condensation level.

If we assume that the updraft velocity w_c scales well with the convective velocity scale w^* (Stevens 2006; Neggers et al. 2006):

$$w^* = \left(\frac{g}{\theta_{v,0}} \eta B \right)^{1/3} \quad (3.10)$$

we can infer that the strength of the updrafts is not sensitive to wind speed either if neither η nor B vary much (Figure 3.4.1). This in turn explains why the mass flux, that is typically calculated as:

$$M = w_c a_c \quad (3.11)$$

is relatively insensitive to wind speed, that is, as long as cloud core fraction a_c does not change. This appears true for our simulations, most evidently for U_5 and U_{10} (Figure 3.3 and 3.4.k).

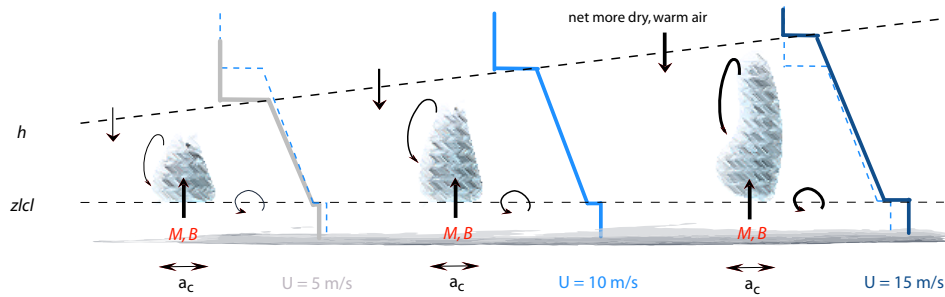


Figure 3.5: Idealized illustration of the response of clouds and the vertical humidity profile to wind speed, as observed in LES.

The above is summarized and illustrated in Figure 3.5. Principally, because the buoyancy flux and mass flux vary little, updrafts are not more energetic at stronger winds. Hence, we do not find evidence for the argument given by Colón-Robles et al. (2006) that stronger low-level wind speeds are associated with more intense cloud base updrafts. They have a larger moisture excess ($q_{t,c} - q_t$), but the extra moisture is carried all the way to the top of the layer, deepening it. Their θ_L deficit ($\theta_{l,c} - \theta_l$) is also larger. Because q_t and θ_l act in opposite ways, there is relatively little change in stability, as experienced by updrafts. This effect can be measured in terms of their deficit in virtual liquid water potential temperature: $\theta_{v,l} = \theta_l (1 + (R_v/R_d - 1) q_t)$. If anything, the $\theta_{v,l}$ deficit is somewhat larger at stronger winds (Figure 3.4.o), but overall the differences are marginal. As such, the excesses in θ_v (hence in buoyancy) are very similar (Figure

3.4.n), except above ≈ 1 km, where liquid water contents also differ (Figure 3.4.d).

3.5. A different behavior at strong winds?

The strongest wind speed case U_{15} differs from U_5 and U_{10} in a few ways. First, there is more wind shear in the sub-cloud layer. As a consequence, turbulent kinetic energy production is dominated by shear ($S = (\overline{u'w'}\partial\bar{u}/\partial z) + (\overline{v'w'}\partial\bar{v}/\partial z)$) rather than by buoyancy $B = g/\theta_0 \overline{w'\theta'_v}$ and the sub-cloud layer is effectively shear-driven (Figure 3.4.i) and j)). Stronger shear may increase the entrainment of cloudy air into the sub-cloud layer (Moeng and Sullivan 1994; Pino et al. 2003; Conzemius and Federovich 2006). This would lead to an increase in the drying tendency and an increase in the surface moisture flux, which is not evident here. Instead, the moisture flux continues to decrease with time, and along with it the buoyancy flux (Figure 3.3). Note that the surface heat flux is negative, associated with a warming of the layer that is principally driven by entrainment from the top. This means that upward transport of moisture has to work against heat and the buoyancy flux is smaller than for U_5 and U_{10} .

A plausible explanation for the different moisture flux behavior follows from the profile of the large-scale drying flux $\overline{w\bar{q}}$. For U_{15} (and also U_{10}) $\overline{w\bar{q}_h}$ is smaller than $\overline{w'q'_h}$ at the inversion (Figure 3.4.c), hence large-scale drying is not sufficient to halt boundary layer growth. However, comparing $\overline{w\bar{q}_h}$ for U_{10} and U_{15} , it is apparent that $\overline{w\bar{q}}$ decreases with height, leading to more moistening at the inversion and less dry air being mixed down. This implies that clouds can continue to deepen the layer at the same rate, but with less moisture flux.

The above explanation can be generalized with the aid of Figure 3.6. This figure uses a bulk approach to sketch an idealization of the boundary layer in equilibrium, in which

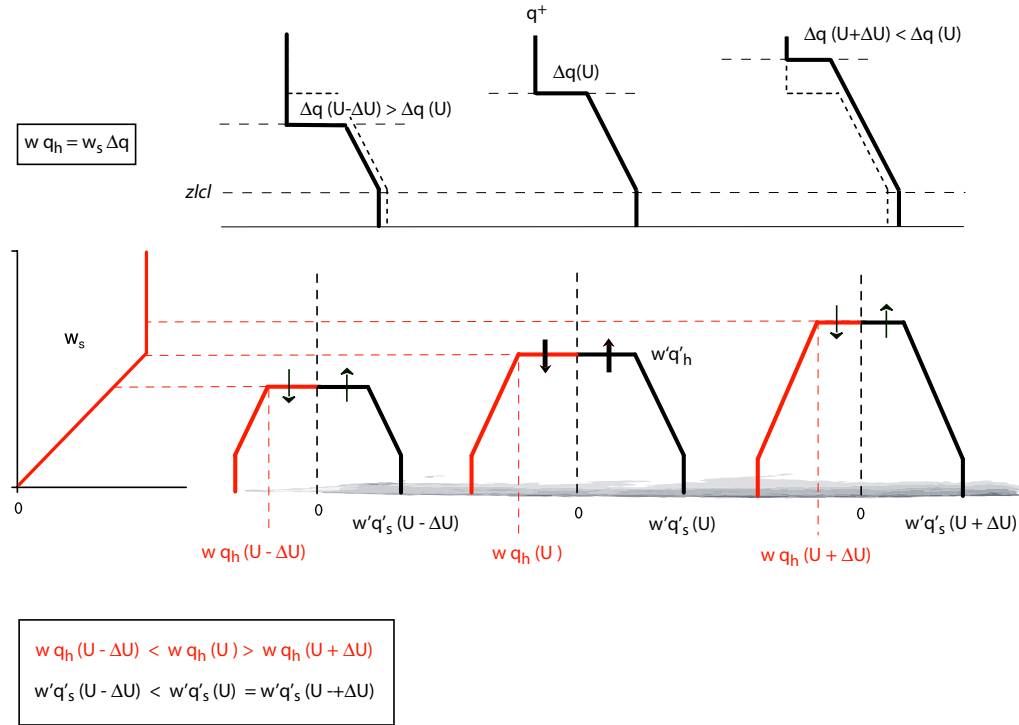


Figure 3.6: Idealized sketch of the moisture balance for different wind speed cases, denoted by $U - \Delta U$, U and $U + \Delta U$. Top panels show humidity profiles. Bottom panels show profiles of the turbulent moisture flux $\overline{w'q'}$ (black) and large-scale drying flux $\overline{w\bar{q}}$ (red). The bottom left profile corresponds to an idealized subsidence profile. The subscripts 'h' and 's' refer to the inversion height and surface respectively.

case turbulent moistening balances large-scale drying at all heights. Although our cases do not reach true equilibrium, this may at least explain where the surface fluxes tend to converge to.

For three different wind speed cases ($U - \Delta U$, U , $U + \Delta U$) the top panels illustrate idealized humidity profiles, and the bottom panels indicate the corresponding moisture flux profiles, with the turbulent moisture flux $\overline{w'q'}$ in black and the large scale drying flux $\overline{w\bar{q}}$ in red. The $\overline{w\bar{q}}$ at the inversion can be modeled as the product of the subsidence velocity w_s and the jump in humidity across the inversion Δq : $\overline{w\bar{q}}_h = w_s \Delta q$. A general

profile for w_s is included at the bottom left of the Figure. The first situation sketches the equilibrium for $U - \Delta U$ (which may be compared with U_5) in which the profiles for $\overline{w\bar{q}}$ and $\overline{w'q'}$ match. After a wind speed increase and associated deepening (the situation U in the middle), the inversion is yet located at a height with stronger subsidence. Even though Δq has decreased, the larger w_s may still lead to a larger drying flux at the inversion, $\overline{w\bar{q}}_h$. In equilibrium, this implies larger drying and moistening fluxes throughout the cloud layer, and hence at the surface: $\overline{w'q'_s}(U) > \overline{w'q'_s}(U - \Delta U)$. Similarly, one can imagine a situation where the layer deepens but subsidence does not increase (the third situation, $U + \Delta U$). Along with a further decrease in Δq , this implies a smaller $\overline{w\bar{q}}|_h$, that can be balanced by a smaller surface flux: $\overline{w'q'_s}(U + \Delta U) < \overline{w'q'_s}(U)$.

In short, if a wind speed perturbation leads to a deepening of the layer up to a height where more large-scale drying is present, the surface fluxes in equilibrium may be larger than before the perturbation. If large-scale drying is less or constant, surface fluxes may remain constant as well.

On long time scales, large-scale subsidence and the (free tropospheric) profiles therefore play an important role in regulating surface fluxes. Note that in our cases, the subsidence profile is roughly constant with height above 2.5 km. Because the free tropospheric humidity is constant, Δq and $\overline{w\bar{q}}_h$ generally decrease with height. We may hypothesize that on even longer time scales, the three wind speed cases may end up with surface fluxes that are not very different (judging the dotted blue lines in Figure 3.4c.). It may be hard to evaluate however if that might be true. The layer is still deepening for U_{15} and clouds are presumably getting too deep for our vertical domain. One can already note some irregular behavior in U_{15} in the time series of cc , a_c and z_{icl} (Figure 3.3).

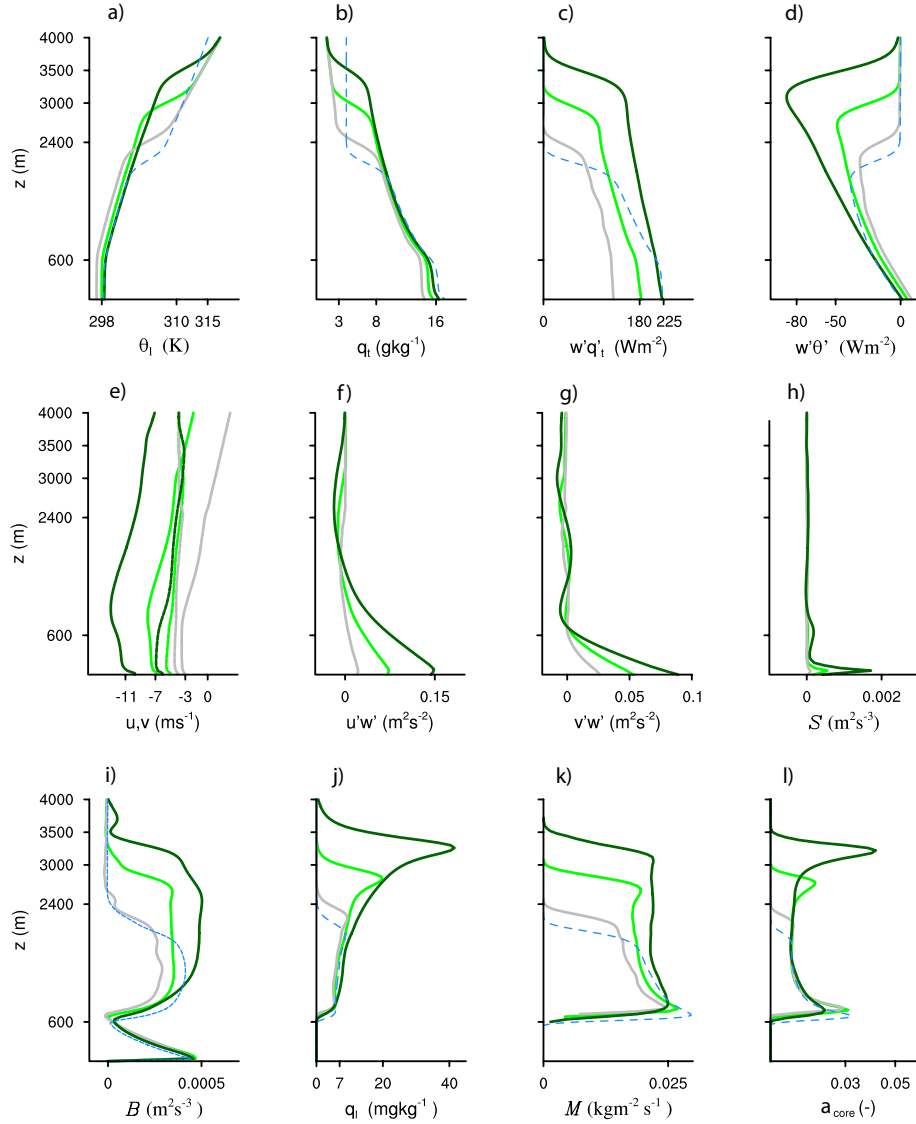


Figure 3.7: Profiles of the RICO case (solid green lines) versus the $S_{8.5}$ case (dashed blue lines), as averages over hour 52-60. RICO simulations are initialized with a (geostrophic) zonal wind profile that equals -9.9 (green), -14.9 (dark green) and -4.9 (grey) at the surface. Variable notation as in Figure 3.4.

The RICO simulations, where shear is present in both the sub-cloud and cloud layer, show overall the same deepening response to wind speed (Figure 3.7). The prescribed subsidence here is much less, hence clouds much deeper. Note that the RICO simu-

lations are only run for 60 hours, with each wind speed case starting from the initial conditions (instead of from a stationary solution). The surface heat flux is still positive. Interestingly, although the clouds are deeper, the stronger wind speed case does not show a deviating behavior in the sub-cloud layer buoyancy flux and moisture flux. It is tempting to use Figure 3.6 to argue that this may be explained from the large-scale drying profile. Indeed, the large-scale drying flux remains roughly constant with height because both the subsidence velocity (Figure 3.1) and the humidity jump at the inversion are constant with height (note that the free tropospheric humidity gradient is negative). However, these simulations have a lower resolution, a shorter duration, additional drying due to horizontal advection, and a much larger deepening rate, that may all contribute to the differences compared to the $S_{7.5}$ case.

3.6. Discussion and conclusions

Cumulus convection responds to an increase in wind speed by significantly deepening the boundary layer and mixing in warmer and drier free tropospheric air (Figure 3.5). It thereby modulates temperature and humidity in the cloud and sub-cloud layer such that a large surface moisture flux, but a smaller (negative) surface heat flux is maintained. The opposite response of the surface fluxes leads to little change in the surface buoyancy flux and sub-cloud layer depth. As a result, the buoyancy and vertical velocity of cumulus updrafts is rather insensitive to the wind speed increase. Similarly, cloud fraction and the convective mass flux vary little with wind speed.

These results differ from our initial hypothesis that was based on radiosonde profiles combined into composites based on average rainfall occurrence (Figure 3.8). In this hypothesis we argued that a shift in the zonal wind speed of about 3 m s^{-1} from one

composite to another (equivalent to changing from a period with hardly any rainfall to a period with moderate rainfall), corresponds to little change in boundary layer depth, but higher humidities throughout the entire layer.

At a first glance, it appears that the observations show a less clear deepening of the layer with wind speed, as compared to the simulations. Having a closer look though one can easily argue an increase in the inversion height anywhere between 0 and 50 hPa, judging from the dotted and dashed profile of θ_e in Figure 3.8. Smaller differences in observed boundary layer depth may have several reasons. For instance, the composites are created by averaging multiple individual radiosondes, where the original inversion structure can easily be obscured. Differences in the origin and path of the air masses measured by the radiosondes, that can reflect differences in temperature and moisture advection, SST's or subsidence, may also play a role. Moreover, stronger winds imply less time traveling *i.e.*, less time to deepen. It remains an interesting question whether changes in wind speed generally co-vary with changes in subsidence, so that the deepening of the layer could be weakened (or reinforced). For example, the U_{15} simulation of $S_{8.5}$ (not shown) has a similar boundary layer depth as the U_5 simulation of $S_{7.5}$.

Our initial hypothesis includes another discrepancy. Based on observations that showed little increase in surface fluxes with an increase in both wind speed and rain (Figure 2.10), we argued that the surface moisture flux recovers back to its original value as a result of enough sub-cloud layer moistening. However, we overlooked that the humidity jump at the top of the layer may have increased with wind speed in the observations (Figure 3.8). As such, large-scale drying across the inversion would have increased and in equilibrium, a larger (surface) moisture flux would have been necessary to balance this. There may be several explanations for this difference related to the

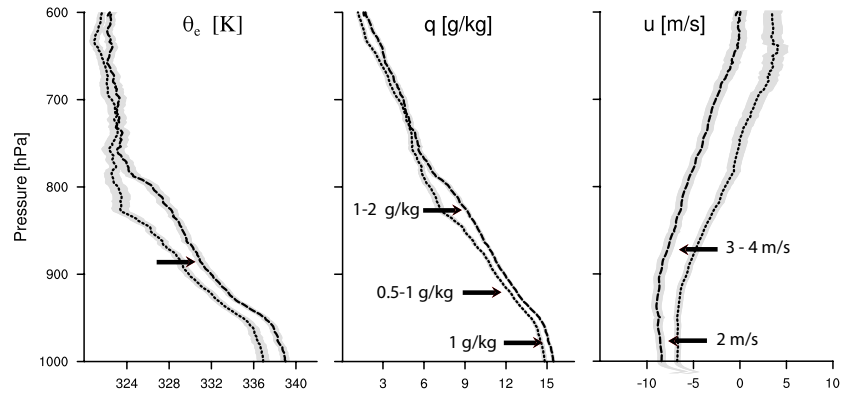


Figure 3.8: Vertical profiles of equivalent potential temperature θ_e , humidity q and zonal wind speed u from radiosondes taken during RICO. The dotted and dashed lines correspond to regimes with little precipitation and moderate precipitation respectively. Adapted from Figure 2.7 in Chapter 3.

idealized nature of our simulations or the uncertainties in the measured surface fluxes.

For example, the measurements used to derive surface fluxes are taken at a single point in the center of a 150 km radius domain over which rainfall estimates are averaged. Heterogeneities in humidity and temperature at 2 m, that are used to calculate the fluxes, across this domain may be large. One reason for such heterogeneities is the presence of so-called cold pools due to evaporative cooling of precipitation below cloud base (Jensen et al. 2000; Snodgrass 2006). Evaporative cooling would indeed increase the surface heat flux and decrease the surface moisture flux. Precipitation, in the measurements estimated to be roughly 30 W m^{-2} , may also lead to less deepening of the boundary layer.

The deepening response itself appears general and independent of the initial vertical profiles in the simulations, the depth of clouds reached, the amount of subsidence applied or wind shear being present. Exactly how much deepening occurs and how the surface fluxes respond in equilibrium, depends on subsidence and the free tropospheric

profiles of temperature and humidity.

In conclusion, our results suggest that through its significant impact on cloud and boundary layer depth, wind speed should be acknowledged as an external force and that it deserves attention in future modeling and observational studies, in particularly those focusing on interactions between large-scale meteorology, clouds and precipitation (the aerosol).

Chapter 4

A bulk perspective on the influence of wind speed

Abstract

The influence of wind speed on the equilibrium structure of the trade-wind layer is explored from bulk theory and compared with LES. Only integrated (bulk) quantities of the sub-cloud and cloud layer are considered. The inversion layer is modeled as a discontinuity and the sub-cloud layer depth equals cloud base height. Using a simple graphical explanation, it is demonstrated that with an increase in surface wind speed, hence in the surface fluxes, an inconsistency in the buoyancy budget of the sub-cloud layer develops if cloud top height (inversion height) does not change. With increased surface evaporation and a moistening of the layer the response of cloud base height is to decrease. To satisfy the moisture and heat balance at cloud top however, and hence the buoyancy budget, an increase in the sub-cloud layer depth, hence in cloud base height, is required. By deepening the layer and increasing the net amount of dry and warm air mixed into the layer, this inconsistency may be resolved.

The response to wind speed is explored in the mixed-layer model, which represents

the sub-cloud layer only, and in a well-known two-layer bulk model of the trade-wind layer (a modified version of Albrecht's model). The mixed-layer model does not capture the response seen in LES, in absence of a representation of the cloud layer. The two-layer model captures some features of the LES, including the moistening and deepening response, although the details of its response depend on the cloud model that is used *i.e.*, the mass flux structure.

From these results we may infer that the deepening response itself does not depend on the detailed internal dynamics of clouds and how they mix with their environment.

4.1. Introduction

In LES of shallow cumulus convection the response of the boundary layer to an increase in wind speed is a moistening of the layer, more evidently in the sub-cloud layer than in the cloud layer. Moreover, a clear increase in the average cloud top and boundary layer height is seen, where the boundary layer is taken to be both the sub-cloud and the cloud layer. The deepening can be explained using the balance between turbulent moistening versus large-scale drying within and at the top of the layer. When the wind speed is perturbed, an imbalance develops because a larger surface moisture flux at stronger winds increases the convective mass flux, hence the turbulent moisture flux at cloud top. In absence of sufficient large-scale drying at cloud top, clouds deepen. More overshooting of cloudy updrafts into the inversion causes dry and warm air to be more readily incorporated into the boundary layer, consequently deepening the layer.

Because the response to wind speed appears general *i.e.*, it is present in all simulations, regardless of the thermodynamic structure and forcings, we may ask to what

extent the internal structure and dynamics of the layer are important in setting the final equilibrium response. For instance, can the new equilibrium of the sub-cloud layer be explained without considering changes in the cloud layer and in entrainment? Do we need arguments such as how the mass flux changes in the transient response to explain that the boundary layer deepens with wind speed?

In exploring the equilibrium structure of the trade-wind layer, bulk models are an interesting (and cheaper) alternative. Moreover, they conceptualize our present understanding of the structure and dynamics of cloudy boundary layers. In bulk theory, the vertical structure of the boundary layer (here considered to include both the sub-cloud and the cloud layer) can be represented by one or two idealized layers. For each layer, the prognostic equations of thermodynamic quantities are integrated, or vertically averaged, over the depth of that layer:

$$\langle \phi \rangle = \frac{1}{z_h} \int_s^{z_h} \phi dz \quad (4.1)$$

with s denoting the surface and z_h denoting the depth of the layer. For layers that are well-mixed due to turbulence, so that quantities are approximately constant with height and the mean structure changes little (for instance, the well-mixed sub-cloud layer), the bulk approach seems natural. For layers that are not well-mixed (the cloud layer), additional assumptions on the internal structure of that layer are required.

Several bulk models that target the thermodynamic structure of the trade-wind layer over subtropical oceans exist. The mixed-layer model (MLM) is a one-layer model that can be used to model the cloud-topped mixed layer (Lilly 1968; Garratt 1992). In section 4.2 we use it as a simple exercise to help understand what is necessary to obtain a sub-cloud mixed layer response that conforms to the simulation results. As anticipated,

it demonstrates that changes in the cloud layer, hence in the transition layer (the thin stable layer that separates the top of the mixed-layer from cloud base height), need to be included to obtain the same response to wind speed as in LES.

Two other well-known models are the model by Betts and Ridgway (1989) (BR89), that models the sub-cloud and cloud layer as a single layer, and the two-layer model by Albrecht et al. (1979). In their model, BR89 assume that the sub-cloud layer depth equals cloud base height and therefore the model does not require a specification of the mass flux. Moreover, thermodynamic quantities in the cloud layer are assumed to lie on a mixing line between sub-cloud layer and free tropospheric values, hence there is no need to include the cloud layer as a separate layer. The mixing line structure in turn depends on a prescribed partitioning between clear and cloudy air in the cloud layer. Albrecht's model on the other hand includes a separate cumulus layer with linear gradients in temperature and humidity. An elaborated version of that model is developed by Bretherton and Park (2008) (BK08), wherein the inconsistencies in the original version (Bretherton 1993; Bellon and Stevens 2005) are resolved. This model version is hereafter referred to as the shallow cumulus bulk model (SCBM). It includes an entraining-detraining bulk plume model that predicts the ensemble mixing dynamics of cumulus convection and the cloud layer structure. It can therefore be used to explore the extent to which the internal cloud (mass flux structure) matters in setting the new equilibrium.

The response of BR89's model to wind speed is described in their paper. It indicates an increase in boundary layer height, and a decrease in cloud base height with stronger winds. Additionally, the surface moisture flux increases, whereas the surface heat flux decreases. The response of the SCBM to wind speed is explored in section 4.3. Also this model predicts an increase in boundary layer height, irrespective of the cloud plume

model (mass flux structure) that is used. These results suggest that the transient response or details on the internal structure are not necessary to explain the deepening response to wind speed. In section 4.4 we use simple equilibrium (bulk) theory to show that the deepening resolves an inconsistency that emerges when wind speed is increased. Our findings are discussed and summarized in section 4.5.

4.2. The mixed-layer model

The simulations performed with LES indicate that in equilibrium, different wind speeds correspond to different surface fluxes. This implies that the turbulent (entrainment) fluxes at the top of the sub-cloud layer also differ with wind speed. Can we illustrate the same response using the simple mixed-layer model (MLM)?

a. *The mixed-layer model equations*

In the MLM, the tendency equations for temperature and humidity (3.5 and 3.5 in Chapter 4) are integrated over the depth of the well-mixed sub-cloud layer given by η :

$$\frac{\partial \theta_M}{\partial t} = \frac{\overline{w'\theta'}|_s - \overline{w'\theta'}|_\eta}{\eta} + Q_r \quad (4.2)$$

$$\frac{\partial q_M}{\partial t} = \frac{\overline{w'q'}|_s - \overline{w'q'}|_\eta}{\eta} \quad (4.3)$$

where for simplicity q_t is written as q and θ_l as θ (Lilly 1968; Garratt 1992; Stevens 2006). The subscript 'M' indicates the bulk (slab, averaged) value, Q_r is the radiative cooling rate (note that the factor θ/T is neglected here), $\overline{w'q'}|_s, \overline{w'\theta'}|_s$ are the surface fluxes and $\overline{w'q'}|_\eta, \overline{w'\theta'}|_\eta$ are the turbulent fluxes at the top of the layer. The latter are

commonly referred to as the entrainment fluxes, representing entrainment of overlying air (here, from the cloud layer) into the mixed layer. Note that subsidence warming and drying terms are absent, because there are no gradients in q_M and θ_M .

The surface fluxes are modeled using bulk aerodynamic formulae:

$$\overline{w'\theta'}|_s = C_D U (\text{SST} - \theta_M) \quad (4.4)$$

$$\overline{w'q'}|_s = C_D U (q_{s(\text{SST})} - q_M) \quad (4.5)$$

$$(4.6)$$

If the mixed-layer is in a steady state, the tendency terms are put to zero and the resulting balances are:

$$\begin{aligned} \overline{w'\theta'}|_\eta &= \overline{w'\theta'}|_s + (\eta Q_r) \\ \overline{w'q'}|_\eta &= \overline{w'q'}|_s \end{aligned} \quad (4.7)$$

Because $Q_r < 0$ and $\overline{w'\theta'}|_s > 0$, $\overline{w'\theta'}|_\eta < 0$ and represents entrainment of potentially warmer air. Similarly, $\overline{w'q'}|_\eta > 0$ and represents entrainment of drier air. If η does not change with wind speed, the entrainment fluxes must change proportionally to the surface fluxes.

Except for the initial perturbation in the surface fluxes due to the wind speed perturbation, the surface fluxes respond passively to changes in temperature and humidity in the sub-cloud layer. Given that radiative cooling is prescribed, a new equilibrium is determined by the change in η and the change in the entrainment fluxes due to the perturbation.

In the MLM the stable layer that tops the mixed layer is represented by a sharp

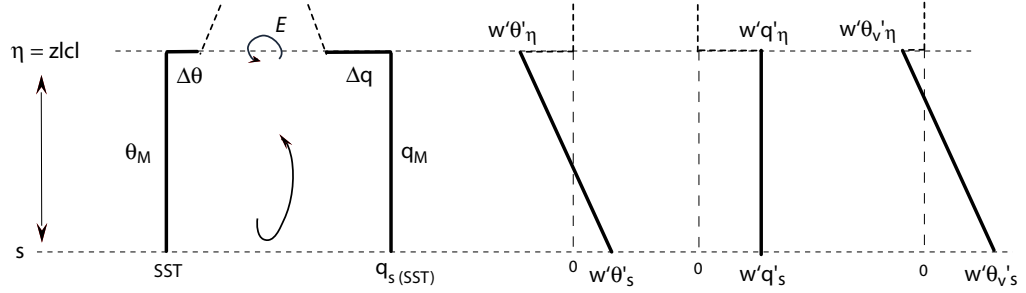


Figure 4.1: Illustration of the mixed-layer model.

discontinuity in $\Delta q, \Delta\theta$ with $\Delta q = q^+ - q_M$ and $\Delta\theta = \theta^+ - \theta_M$ with (Figure 4.1). In a dry convective boundary layer this discontinuity represents the inversion layer. In a cumulus-topped mixed-layer, the mixed-layer height is chosen to equal cloud base height (the lifting condensation level of mixed-layer air with properties θ_M and q_M). The discontinuity then equals the thin stable layer (the transition layer) that in observations separates the top of the mixed layer η from cloud base height (Augstein et al. 1974; Albrecht et al. 1979; Yin and Albrecht 2000). The transition layer is most evident in humidity and to a lesser extent in temperature.

The turbulent fluxes at the top of the mixed-layer can be modeled as the product of the jump across the transition layer and a velocity E , that represents the rate at which air is entrained across η :

$$\begin{aligned}\overline{w'\theta'}|_{\eta} &= -E \Delta\theta \\ \overline{w'q'}|_{\eta} &= -E \Delta q\end{aligned}\tag{4.8}$$

E is obtained from the typical closure used in convective boundary layers, in which the

buoyancy flux at η is a given fraction $\kappa = -0.2$ from the surface buoyancy flux $\overline{w'\theta'_v}|_s$:

$$E = \frac{\overline{w'\theta'_v}|_\eta}{\Delta\theta_v} = \kappa \frac{\overline{w'\theta'_v}|_s}{\Delta\theta_v} \quad (4.9)$$

where $\Delta\theta_v$ and $\overline{w'\theta'_v}|_s$ are given by:

$$\Delta\theta_v = \Delta\theta + (R_v/R_d)(\theta\Delta q + q\Delta\theta) \quad (4.10)$$

$$\overline{w'\theta'_v}|_s = C_D U (\theta_{v,s} - \theta_{v,M}) \quad (4.11)$$

b. *The response to wind speed in comparison with LES*

From the LES, we expect the surface fluxes to increase with the initial wind speed perturbation and to moisten and warm the layer. If this happens such that relative humidity remains constant, then η does not change. As a first approximation we may assume that the overlying air (the cloud layer) warms and moistens proportionally to the sub-cloud layer, and hence that Δq and $\Delta\theta$ remain constant. What is the response of the MLM to wind speed in that case?

Figure 4.2 plots the steady-state solutions of cases that differ only in their specification of Δq and $\Delta\theta$. These are somewhat arbitrarily chosen, combining into different values of $\Delta\theta_v$. The colors represent small (blue) to large (green) values of $\Delta\theta_v$, and moving along a given color implies moving along constant $\Delta\theta_v$, Δq and $\Delta\theta$. The initial and boundary conditions, summarized in Table 4.1, are taken from the S_{8.5} and S_{7.5} cases used in LES (Chapter 3).

Generally, a larger $\Delta\theta_v$ implies a smaller E , hence less entrainment of dry air. This leads to a higher sub-cloud humidity, a lower cloud base height and smaller surface

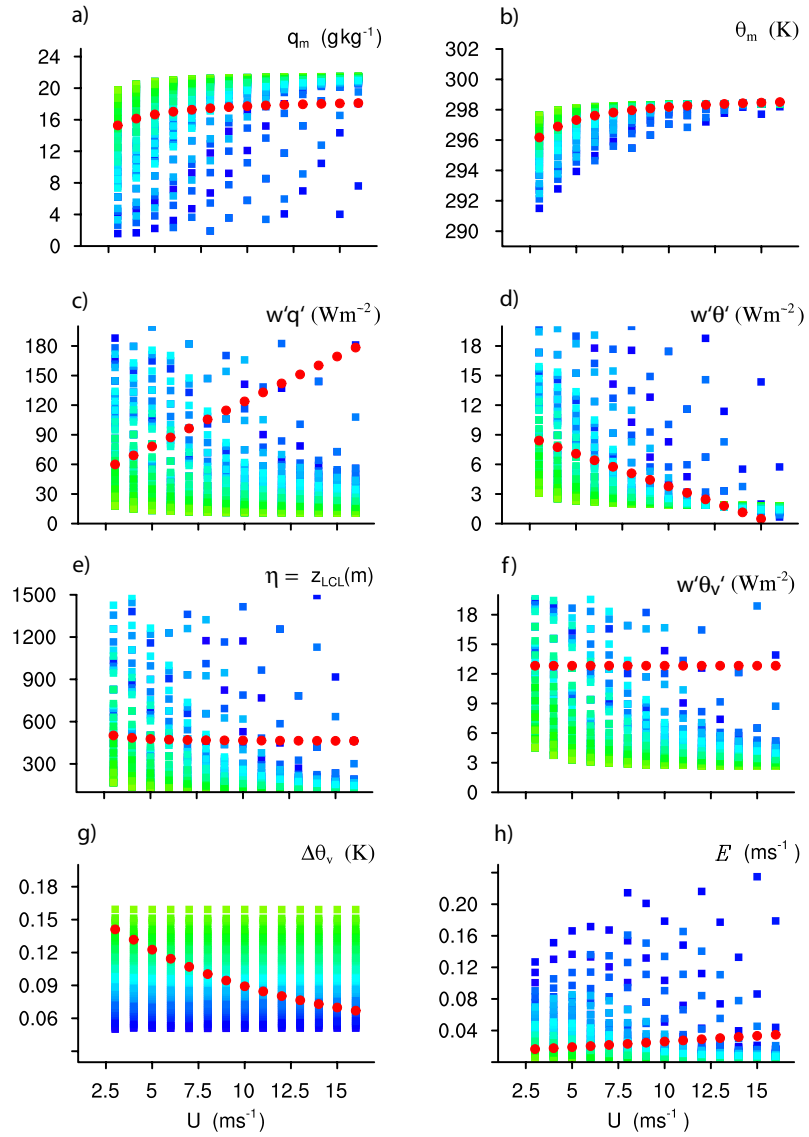


Figure 4.2: Sensitivity of (a) specific humidity $\overline{q_M}$, (b) potential temperature θ_M , (c) the surface moisture flux $\overline{w'q'}$, (d) the surface heat flux $\overline{w'\theta'}$, (e) the mixed-layer and cloud base height $\eta = z_{cl}$, (f) the surface buoyancy flux $\overline{w'\theta'_v}$, (g) and (h) the entrainment velocity E to wind speed U in the mixed-layer model for a range of $\Delta\theta_v = \{0.03\text{K (dark blue)} - 0.16\text{K (light green)}\}$. The red dots indicate one example of a solution in which Δq_t is adjusted as to maintain a constant $\overline{w'\theta'_v}|_s$. Further details are given in the text.

MLM: initial conditions and forcings

SST	(K)	300
$q_{M,0}$	(g kg ⁻¹)	13
$\theta_{M,0}$	(K)	298
η_0	(m)	800
p_s	(hPa)	1020
Q_r	(K d ⁻¹)	2.5
Δq	(g kg ⁻¹)	{0, -0.02, ..., -2}
$\Delta\theta$	(K)	{0, 0.02, ..., 0.16}

Table 4.1: The initial conditions and forcings derived from case S1 used in Chapter 4 (Table 3.1) and here used for the mixed-layer model.

moisture flux. For $\Delta\theta_v > 0.12$, the solutions predict an unrealistically low moisture flux and cloud base height, whereas for $\Delta\theta_v < 0.03$ solutions are rather unrealistic in that relative humidities in the sub-cloud layer become less than 10%. Focusing on intermediate values of $\Delta\theta_v$, stronger winds overall correspond to a warmer and more humid mixed-layer and a lower mixed-layer height η .

Compared to LES, where cloud base height varies little with wind speed, the MLM thus predicts a more sub-cloud layer, hence a lower cloud base height, at stronger winds. This is consistent with the decrease in E seen in the MLM. The only way one can maintain the same cloud base height is by increasing the entrainment fluxes of dry and warm air with wind speed. In the MLM, the only way to increase entrainment is through a change in $\Delta q, \Delta\theta$. Note that with constant $\Delta\theta_v$, an increase in the surface buoyancy flux would be necessary to obtain larger entrainment fluxes (Equation 4.9 - 4.8), which is inconsistent with little change in cloud base height and η (see also Equation 3.9).

Allowing Δq to change in the MLM, so that the surface buoyancy flux remains constant with wind speed, leads to a solution whereby cloud base height changes little,

whereas the surface moisture flux increases, as in LES. This is the solution indicated by the red dots in Figure 4.2 (note that the decrease in $\Delta\theta_v$ corresponds to an increase in Δq).

In LES the entrainment fluxes indeed appear to increase not due to a change in E , but by a change in $\Delta q, \Delta\theta$. This is because E varies proportionally to the convective mass flux M , which in LES varies little with wind speed. From the mass budget of the sub-cloud layer:

$$\frac{\partial\eta}{\partial t} = E - M - \bar{w} \quad (4.12)$$

one can see that $E \sim M$ if $d\eta/dt = 0$. The changes in humidity, temperature and buoyancy jumps in LES are roughly estimated in Table 4.2 by applying the mixed-layer approach to the U_5 and U_{10} results in Chapter 3.

The increase in Δq and $\Delta\theta$ with wind speed are due to a deepening of the layer and enhanced downward mixing of warm and dry air. Because Δq and $\Delta\theta$ change in opposite ways, they act to maintain the transition layer equally stable with respect to rising thermals from the mixed-layer, which thereby constrains the buoyancy and mass flux.

4.3. A two-layer shallow cumulus bulk model

The shallow cumulus bulk model (SCBM) by (Bretherton and Park 2008) (BP08) is a two-layer model and can hence more realistically capture the interaction between the cumulus layer and the underlying well-mixed layer. This interaction *e.g.*, the removal of sub-cloud layer air by the convective mass flux and the entrainment of cumulus layer air into the sub-cloud layer, are important in regulating the detailed behavior of the sub-

Parameter		U5	U10
z_{lcl}	(m)	524	503
E	(m s^{-1})	0.028	0.028
$\overline{w'q'} _{\eta}$	(W m^{-2})	148	211
$\overline{w'\theta'} _{\eta}$	(W m^{-2})	-11	-15
Δq	(g kg^{-1})	-1.83	-2.60
$\Delta\theta$	(K)	0.39	0.54
$\Delta\theta_v$	(K)	0.06	0.08

Table 4.2: Estimates of cloud base height z_{lcl} , entrainment rate E , turbulent moisture and heat fluxes at $\eta = z_{lcl}$ (from Equation 4.7), and the humidity, potential temperature and virtual potential temperature jumps $\Delta q_t, \Delta\theta_t, \Delta\theta_v$ at $\eta = z_{lcl}$ (from Equation 4.8 and noting that in equilibrium $E = M - \bar{w}$). All estimates are averages of the last eight hours of simulation of the S1 case performed with LES (Chapter 4).

cloud layer and the response of the surface fluxes to wind speed.

The additional advantage of the SCBM is that it includes a flexible cloud scheme that predicts the vertical structure of the mass flux and the cumulus updraft excesses of temperature and humidity. It therefore offers the possibility to explore to what extent the deepening of the cloud layer (the main response to wind speed in LES) depends on the choice of the cloud scheme (section c).

a. *A short description of the SCBM*

The SCBM is a refinement of the two layer bulk model developed by Albrecht et al. (1979). It has been used by BP08 to study the response of BOMEX shallow cumuli to a SST perturbation. Here we shortly describe the main model features and key assumptions, for a detailed description we refer to BP08 and Appendix C. The thermodynamic structure of the model is defined in terms of pressure and the conserved variables

$q_t = q_v + q_l$, the total specific humidity and θ_{vl} , the liquid water virtual potential temperature (Figure 4.3):

$$\theta_{vl} = \theta_l \left(1 + \left(\frac{R_v}{R_d} - 1 \right) q_t \right) \quad (4.13)$$

where $\theta_l \approx \theta - (L_v q_l / C_p \Pi)$, Π is the Exner function $\Pi = (p/p_{00})^{R_d/C_p} = T/\theta$ and $(\frac{R_v}{R_d} - 1) \approx 0.608$ with $R_v = 461.5 \text{ J kg}^{-1}$ and $R_d = 287 \text{ J kg}^{-1}$ (the gas constants for water vapor and dry air).

The model includes two layers, the sub-cloud mixed layer (denoted by 'M') and the cumulus layer (denoted by its mid-point 'H'), that are separated from the overlying free troposphere through an infinite (sharp) inversion layer (denoted by 'I'). The two layers are separated by the transition layer located at cloud base (denoted by 'B'). Other notations used are capital letters for the surface ('S'), the subscript 'c' that denotes the cumulus updraft, the subscript 'e' that denotes entrainment, and Δ , that denotes the jump of any quantity across the transition layer Δ_B or the inversion Δ_I .

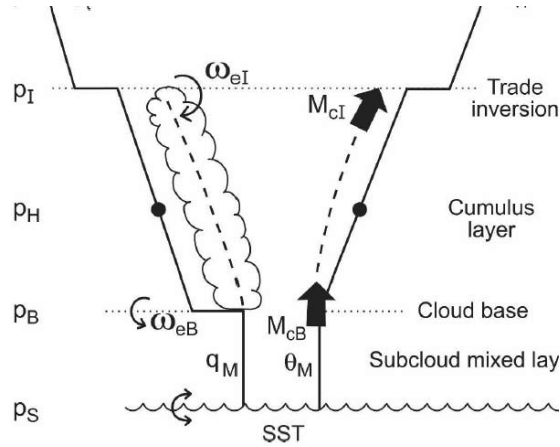


Figure 4.3: Cartoon (taken from Bretherton and Park (2008)) illustrating the two-layer structure of the shallow cumulus bulk model.

Within the cumulus layer, θ_{vl} and q_t are defined as :

$$\theta_{vl}(p) = \theta_{vlM} + \gamma_{vl} (p_B - p) \quad (4.14)$$

$$q_t(p) = q_{tM} + \Delta_B q_t \gamma_{qt} (p_B - p) \quad (4.15)$$

where the jump in θ_{vl} across the transition layer $\Delta_B \theta_{vl}$ is assumed to equal zero. This is the first assumption, stating that there is no turbulent (entrainment) flux of θ_{vl} across the transition layer. This is a reasonable assumption given that this jump is typically much smaller than the change in temperature throughout the cumulus layer (see for instance Figure 3.4).

The model solves five prognostic equations: for θ_{vl} and q_t in the sub-cloud layer ('M'), for θ_{vl} and q_t in the middle of the cumulus layer ('H') and for the pressure at the inversion ('I'). The SCBM is forced by radiative cooling Q_r , large-scale divergence (large-scale subsiding motion $\bar{\omega}$), free tropospheric profiles of θ_{vl} and q_t and the surface fluxes. The latter depend on the product of the surface transfer velocity $\omega_{tS} = \rho_S g C_T U$ and the differences between temperature and humidity in the sub-cloud layer (M) and the surface (S) (the bulk aerodynamic formulation). The full prognostic equations are included in Appendix C.

One major modification of the SCBM compared to Albrecht's version is that the cumulus layer gradients of θ_{vl} and q_t (γ_{vl} , γ_{qt}) are simply diagnosed, rather than prognosed. Because $\Delta_B \theta_{vl} = 0$, knowing θ_{vlM} , θ_{vlH} and p_I at any time step allows one to diagnose the temperature gradient. The most elaborate part of the model involves diagnosing $\Delta_B q_t$ and γ_{qt} such that they are consistent with the temperature structure. This is done through two additional closure assumptions that allow one to solve for the two

unknowns $\Delta_B q_t$ and γ_{qt} .

Other key assumptions of the model The first closure assumption is the so-called “entrainment-consistency condition”. It states that the rate at which free tropospheric air is entrained into the boundary layer, ω_{eI} , is the same for heat and moisture. The product of the penetrative entrainment velocity ω_{eI} and the jumps across the inversion $\Delta_I \theta_{vl}$, $\Delta_I q_t$ equals the cumulus heat and moisture fluxes into the inversion $g M_{cI} \widetilde{\theta_{vl}}$ and $g M_{cI} \widetilde{q_{tI}}$. This directly links the cumulus excess of humidity at the inversion to that of temperature:

$$\widetilde{q_{tI}} / \Delta_I q_t = \widetilde{\theta_{vl}} / \Delta_I \theta_{vl} \quad (4.16)$$

where $\widetilde{\theta_{vl}}$ is the cumulus excess of temperature: $(\theta_{vlcI} - \theta_{vlI})$, $\widetilde{q_{tI}}$ is the cumulus excess of humidity $(q_{tcI} - q_{tI})$ and M_{cI} is the convective mass flux at the inversion. The cumulus excesses and the inversion mass flux follow from the cloud model (see further below).

The second assumption is the “penetrative entrainment” closure, stating that at the inversion, the ratio of the cumulus updraft buoyancy excess ($\widetilde{\theta_{vI}}$) to its θ_{vl} deficit ($\widetilde{\theta_{vl}}$) must equal the factor A^{-1} :

$$\widetilde{\theta_{vI}} = -\widetilde{\theta_{vl}} / A \quad (4.17)$$

$$\widetilde{\theta_{vl}} + \lambda \widetilde{q_{tI}} = -\widetilde{\theta_{vl}} / A \quad (4.18)$$

In other words, updrafts contain just the amount of liquid water they need to achieve a positive buoyancy that depends on A and the vertical temperature and humidity struc-

ture. This is because the difference between θ_v and θ_{vl} is just the liquid water content:

$$\theta_v = \theta (1 + 0.608 q_v - q_l) \quad (4.19)$$

$$\begin{aligned} &= \theta (1 + 0.608 q_t - 1.608 q_l) \\ &= \theta_l \frac{(1 + 0.608 q_t - 1.608 q_l)}{1 - L_v q_t / C_p T} \\ &\approx \theta_{vl} + \lambda q_l \end{aligned} \quad (4.20)$$

where $\lambda = \frac{\mu L_v}{C_p \Pi}$ and $\mu = 1 - (1 + 0.608) \frac{C_p T}{L_v}$.

BP08 notes that solutions are not very sensitive to A , which they call the penetrative entrainment efficiency. They discuss that in the SCBM a strong negative penetrative entrainment feedback is present: a de-stabilization of the boundary layer leads to vigorous updrafts, that in turn quickly act to stabilize the layer by mixing in more warm air through penetrative entrainment and limiting updraft buoyancy. Entrainment of dry air would destabilize the cloud layer by enhancing surface evaporation, but via entrainment, a drier cloud layer in turn causes updrafts to loose their buoyancy more readily. Important to note is that both closure equations depend to a large extent on the cloud model *e.g.*, the assumptions made about entrainment and detrainment. This is because the cumulus excesses, the θ_{vl} deficit and q_t excess, are determined from the cloud model. As such, liquid water and the θ_v excess are already constrained and A plays an almost negligible role in determining the mean thermodynamic structure.

Cloud model In the SCBM, the mass flux at cloud base M_{cB} is chosen such that the penetrative entrainment closure is zero at each new time step. Two provisional solutions are determined for $M_{cB} = 0$ and 0.1 Pa s^{-1} . The desired M_{cB} then follows through linear interpolation. A cloud model is used to predict the (non-dimensional) mass flux at the

inversion per unit mass flux at cloud base: $m_I = M_{cI}/M_{cB}$ (see Appendix C for a more elaborate description). The cloud model also predicts the coefficients G_I and b_I that specify the change in the cumulus updraft excesses $\widetilde{\theta}_{vI}, \widetilde{q}_{tI}$ with height depending on their original excess at cloud base and the dilution due to entrainment of environmental air:

$$\widetilde{\theta}_{vI} = -G_I \gamma_{vl} \quad (4.21)$$

$$\widetilde{q}_{tI} = -G_I \gamma_{qt} - b_I \Delta_B q_t \quad (4.22)$$

In BP08, m_I , b_I and G_I are determined by an entraining - detraining plume model:

$$\frac{dM}{dp} = -(\epsilon - \delta) M \quad (4.23)$$

The cloud plume model can principally be used to derive the vertical structure of cumulus updraft properties within the cloud layer, but the bulk model itself only requires the values at cloud base and at the inversion. It should be noted that the assumption of linear gradients within the cloud layer may not be exactly consistent with the assumed entrainment and detrainment that follow from the chosen cloud model. This implies that the profile of $\widetilde{\theta}_v$ (the virtual potential temperature excess, and hence the buoyancy excess $\widetilde{b} = g \frac{\widetilde{\theta}_v}{\theta_{00}}$) can and does vary non-linearly with height. It may even be negative at some heights in the cumulus layer (see Figure 4.4c.). Important to remember is that the mass flux and entrainment and detrainment in the SCBM do not respond to the updraft buoyancy profile. Only $\widetilde{\theta}_v$ at the inversion is used in the model, through the penetrative entrainment closure in Equation 4.18 (personal communication, Chris Bretherton).

Different versions of the cloud model are used here: one in which entrainment and

detrainment are constant with pressure and one in which they vary with pressure as $\epsilon, \delta \sim c_e/dp$. A third option explores the use of a constant mass flux at the inversion: $m_I = M_{cI}/M_{cB} = \text{constant}$ (see also Appendix C).

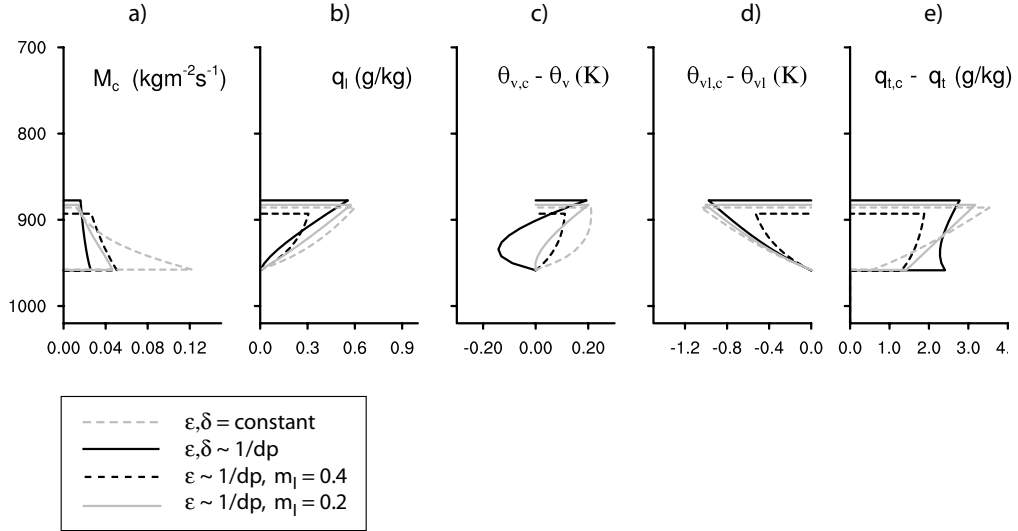


Figure 4.4: Vertical cloud and mass flux structure from SCBM solutions at day 16 with a 10 m s^{-1} wind speed. The panels represent the mass flux (a), cloud liquid water (b), the θ_v excess (c), θ_{vl} -deficit (d) and q_t excess of cumulus updrafts. Different lines and colors represent different versions of the cloud plume model used (see legend and Appendix C).

b. Solution of the reference case

The initial and boundary conditions for the SCBM, summarized in Table 4.3, are taken from the $S_{7.5}$ and $S_{8.5}$ cases used in LES. The SCBM does not yield a steady-state solution for $S_{7.5}$ with a subsidence of $\bar{w} = 7.5 \cdot 10^{-3} \text{ m s}^{-1}$ (results are not shown). This could have been anticipated given that LES does not obtain a steady-state solution with a zero boundary layer growth for this case either. The $S_{8.5}$ case with a subsidence of $\bar{w} = 8.5 \cdot 10^{-3} \text{ m s}^{-1}$ and a wind speed of 10 m s^{-1} does lead to a steady-state solution af-

ter roughly 16 days. It predicts cumuli that are rather shallow, with the inversion height at roughly 870 hPa for all different versions of the cloud model (Figure 4.4).

Case specifications for SCBM

Forcings

ω_B	(Pa s ⁻¹)	$g \rho_B \bar{w}(z_B)^{(1)}$
ω_I	(Pa s ⁻¹)	$g \rho_I \bar{w}(z_I)^{(1)}$
Q_r	(K d ⁻¹)	2.5
U	(m s ⁻¹)	10
SST	(K)	300
p_S	(hPa)	1020
q_t^+	(g kg ⁻¹)	4
$\theta_{v,l}^+$	(K)	$299.03 + (4.14 \cdot 10^{-4})(p_S - p)$

Initial and boundary conditions

p_B	(hPa)	962
p_I	(hPa)	860
$SST - T_{MS}$	(K)	0
$\gamma_{vl}/\gamma_{vl}^{ma}$	(-)	0.5

Model parameters

ϵ	(Pa ⁻¹)	$2.5 \cdot 10^{-4}$
δ	(Pa ⁻¹)	$3.45 \cdot 10^{-4}$
c_e	(-)	1.4
c_d	(-)	2
A	(-)	5

Table 4.3: The initial conditions and forcings for the SCBM derived from the equilibrium state of case S2 used in Chapter 4 (Table 3.1). Values of p_B , p_I , $SST - T_{MS}$, ϵ and δ are based on eight hour averages at the end of the S2 U10 simulation. ⁽¹⁾ $\bar{w}(z) = \bar{w}_0(1 - e^{-z/H})$, $\bar{w}_0 = 8.5 \cdot 10^{-3} \text{ m s}^{-1}$, $H = 1000 \text{ m}$.

The difficulty of using constant entrainment ϵ and detrainment δ (dashed grey lines) is that little or zero mass flux remains at cloud top when clouds get (too) deep. The model therefore needs to choose a large mass flux at cloud base to maintain at least some

mass flux at cloud top that is consistent with the closures. The other model versions predict less decrease of mass flux with height. The versions differ mostly in their updraft humidity excess and virtual potential temperature excess (Figure 4.4e. and c.). The first depends on the cloud base humidity jump Δ_{Bq_t} and humidity gradient in the cloud layer γ_{qt} , that both appear explicitly in the closure equations. These are evidently the more sensitive parameters of the model. The differences in the virtual potential temperature excess, compared to the θ_{vl} deficit, reflect mostly differences in liquid water content. Because γ_{vl} and γ_{qt} are strictly linear in the model, unrealistic updraft profiles may be obtained, such as in this case, the negative θ_v excess for the cloud model in which entrainment and detrainment vary with height. As mentioned previously in section a), this does not affect the model itself, because it uses only the θ_v excess at the inversion.

c. The response to wind speed

A sudden wind speed perturbation is applied to the steady-state solution of $S_{8.5}$. Even though the cumuli for this case are not very deep, the solutions still get unstable if the wind speed perturbation is large (the 7.5 - 10 m s^{-1} wind speed cases reach a steady-state, whereas the 5, 12.5 and 15 m s^{-1} do not). It is clear that we are pushing the limits of the model. We therefore focus on the solution obtained 4 days after the perturbation, which gives a fairly good impression of the general behavior of the model in response to wind speed. However, one should keep in mind these results do not reflect a final equilibrium solution. This can for instance be seen from the moisture flux profiles in the sub-cloud layer that indicate that the surface moisture flux does not yet balance the flux at the top of the sub-cloud layer (Figure 4.6).

Irrespective of the cloud model used, the SCBM predicts that at stronger winds, the

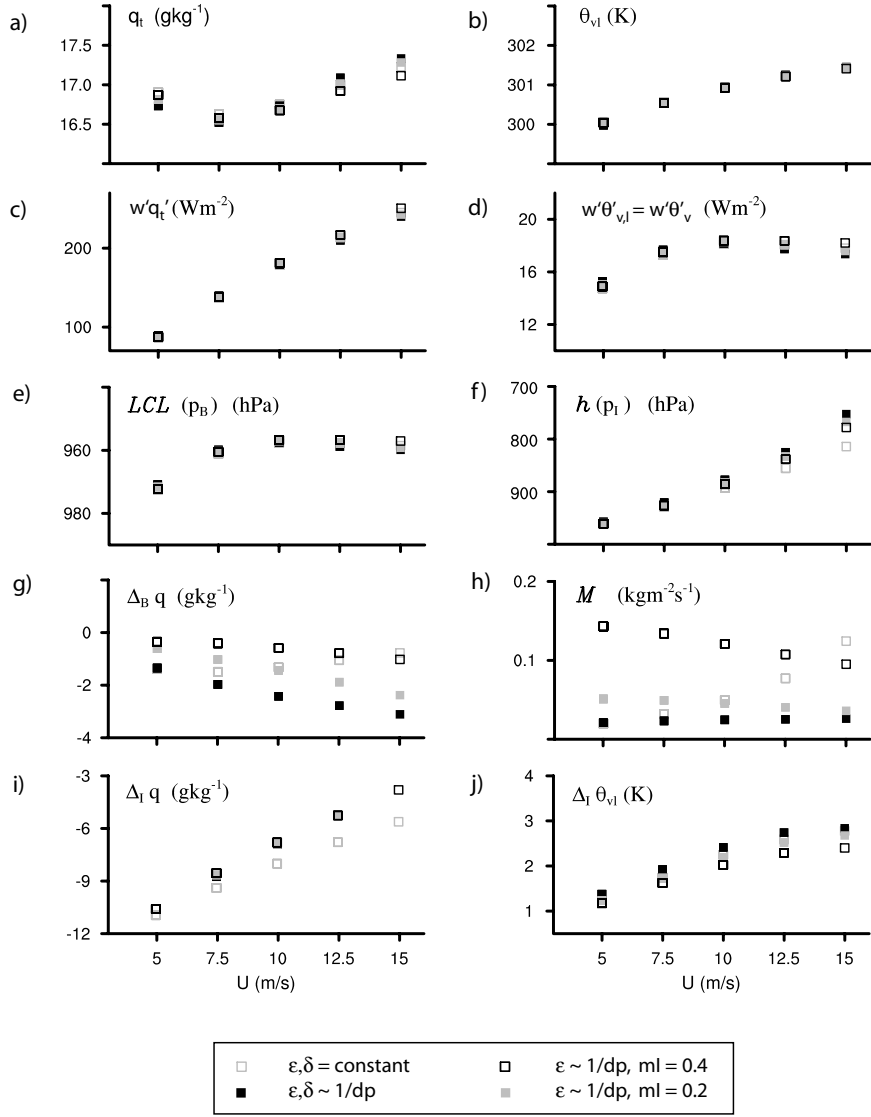


Figure 4.5: Solutions of the SCBM versus wind speed at day 20 (the wind speed is perturbed on day 16). Panels show (from top to bottom, left to right) the sub-cloud layer q_t (a), the sub-cloud layer θ_{vl} (b), the surface moisture flux (c), the surface θ_{vl} (buoyancy) flux (d), cloud base height (e), inversion (cloud top) height (f), the q_t jump at cloud base (g), the mass flux at cloud base (h), the q_t jump at the inversion (i) and the θ_{vl} jump at the inversion. Different symbols correspond to different versions of the cloud plume model used, see legend and Appendix C.

surface moisture flux is larger and the (cloud) layer is deeper (Figure 4.5 c and f), and Figure 4.6 a and b). The model also predicts that both cloud base and the surface buoyancy flux vary little with wind speed (Fig.4.5 d and e) - note that the flux of θ_{vl} equals the buoyancy flux in the sub-cloud layer). Because the buoyancy flux varies little, whereas the moisture flux increases, the surface heat flux here must decrease with wind speed.

The general response of the model is thus similar to the LES and independent of the internal dynamics (the mass flux and cloud structure). The differences that do arise due to a different mass flux structure present themselves most clearly in the vertical structure of humidity. This is as expected as the model chooses $\Delta_B q_t$ and γ_{qt} such that the closure is satisfied. The larger the mass flux at cloud base (Figure 4.4.a), the smaller $\Delta_B q_t$ (Figure 4.4 e). This can be understood from the moisture balance in the sub-cloud layer: the moisture flux at the surface must equal the flux at the top of the sub-cloud layer:

$$\overline{w'q'_tS} = \overline{w'q'_tB} = M_{cB} \widetilde{q}_{tB} = M_{cB} \Delta_B q_t \quad (4.24)$$

Because the surface flux varies little among the different model versions, the mass flux and cloud base jump vary oppositely.

Small differences in the gradient of q_t in the cloud layer can be noted (Figure 4.6 a). For instance, the plume model with constant ϵ and δ (dashed lines) has steeper gradients than the model with $\epsilon, \delta \sim 1/dp$ (solid lines). The more humid environment in the lower cloud layer and the steeper q_t gradient consequently allows for a relatively high moisture excess and liquid water content in cumulus updrafts at the inversion (Figure 4.4 b and e). Note that the spread in $\Delta_I q_t$ and $\Delta_I \theta_{vl}$ among the models at strong winds (Figure 4.5 h and i) mostly reflects the differences in inversion height that are reached.

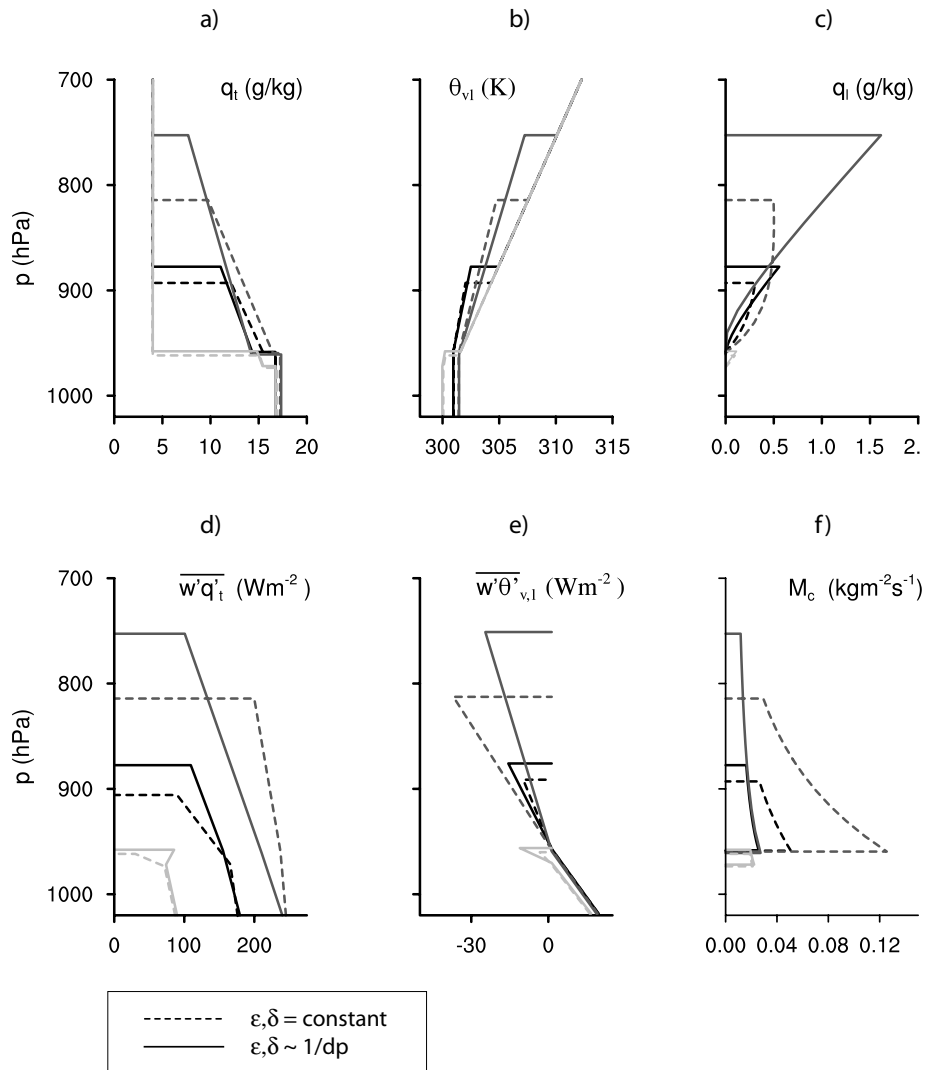


Figure 4.6: The vertical structure predicted by the SCBM at day 20 for wind speeds of 10 m s^{-1} (black), 5 m s^{-1} (light grey) and 15 m s^{-1} (dark grey). The panels show profiles of q_t (a), θ_{vl} (b), liquid water q_l (c), the turbulent moisture flux (d), the turbulent flux of θ_{vl} (e) and the mass flux (f). Solid versus dashed lines indicate different cloud plume models used, see legend and Appendix C.

4.4. A simple explanation for the deepening response at stronger winds

Can the deepening response to wind speed be understood without considering the detailed internal structure or without relying on mass flux arguments? To explore whether

a new equilibrium solution may be obtained that is also consistent with a zero deepening of the boundary layer, we here use a simple graphical illustration. Figure 4.7 illustrates a simplified vertical structure of the trade-wind layer. The solid lines indicate the profiles of temperature and humidity and their corresponding fluxes before the wind speed is perturbed. The sub-cloud layer is well-mixed in temperature θ_M and humidity q_M . The sub-cloud layer depth η is assumed to equal the lifting condensation level. Jumps in temperature and humidity at the top of the sub-cloud layer are ignored. The profiles are linear in the cloud layer with a discontinuity at the top of the cloud layer h (the inversion) represented by $\Delta\theta$ and Δq . The fluxes Q_θ and Q_q at the surface and at the top are indicated with the subscripts s and h .

At the surface, the heat and moisture flux Q_θ and Q_q are modeled using bulk aerodynamic formulae:

$$Q_{q,s} = C_D U (q_s - q_M) \quad (4.25)$$

$$Q_{\theta,s} = C_D U (\theta_s - \theta_M) \quad (4.26)$$

The fluxes at h can be linearly related to the surface fluxes by using the change in flux across the cloud layer Q_{cl} :

$$Q_{q,h} = Q_{q,s} - Q_{q,cl} = C_D U (q_s - q_M) - Q_{q,cl} \quad (4.27)$$

$$Q_{\theta,h} = Q_{\theta,s} - Q_{\theta,cl} = C_D U (\theta_s - \theta_M) - Q_{\theta,cl} \quad (4.28)$$

with $Q_{\theta,cl}, Q_{q,cl} > 0$. In equilibrium, $Q_{q,h}$ and $Q_{\theta,h}$ must equal the large-scale drying respectively warming flux at h . These are typically represented by the product of the subsidence velocity w_s and the jump of temperature and humidity across h :

$$w_s \Delta q = C_D U (q_s - q_M) - Q_{q,cl} \quad (4.29)$$

$$w_s \Delta \theta = C_D U (\theta_s - \theta_M) - Q_{\theta,cl} \quad (4.30)$$

with $w_s < 0$, $\Delta q < 0$, $\Delta \theta > 0$. . One can define a wind speed perturbation of δU and assume that for $\delta U > 0$ the layer moistens homogeneously by an amount δq and $\delta \theta$. In a bulk approach this implies that the gradients dq/dz and $d\theta/dz$ do not change. The red and black dashed profiles in Figure 4.7 resemble the possible new equilibria.

The first possibility implies that the layer has moistened enough by δq to offset the increased contribution of wind speed to the surface flux (the red profiles), and therefore $\delta Q_q = 0$, with δQ_q defined as:

$$\delta Q_q = C_D \delta U (q_s - q_M) - C_D U \delta q \quad (4.31)$$

If the surface flux does not change, then $Q_{q,h}$ does not change either (Equation 4.28). However, this is inconsistent with the large-scale drying flux at h that has increased by an amount of $w_s \delta q$:

$$w_s (\Delta q - \delta q) \neq Q_{q,h} \quad (4.32)$$

This leaves only the possibility $\delta Q_q \neq 0$ i.e., there is a certain amount of moistening, but not enough to offset the change in wind speed. If $\delta U > 0$ we expect $\delta Q_q > 0$ (the black dashed lines in Figure 4.7). Rewriting Equation 4.30 gives a new expression for the flux balance at h :

$$\begin{aligned}
w_s (\Delta q - \delta q) &= Q_{q,s} - Q_{q,cl} + \delta Q_q \\
&= Q_{q,s} - Q_{q,cl} + C_D \delta U (q_s - q_M) - C_D U \delta q \\
&= Q_{q,s} - Q_{q,cl} + (\delta U/U) Q_{\theta,s} - C_D U \delta q
\end{aligned} \tag{4.33}$$

This appears a plausible new equilibrium whereby h does not change and the layer moistens. Using $w_s \Delta q = Q_{q,h} = Q_{q,s} - Q_{q,cl}$, the expression can be re-arranged to solve for the amount of moistening δq :

$$\delta q = \frac{Q_{q,s} (\delta U/U)}{C_D U - w_s} \tag{4.34}$$

A similar derivation can be done for temperature and gives the expression for $\delta \theta$:

$$\delta \theta = \frac{Q_{\theta,s} (\delta U/U)}{C_D U - w_s} \tag{4.35}$$

Because the denominator is > 0 , a situation with surface fluxes being positive initially leads to a net moistening and warming when the wind speed is increased. As long as δq and $\delta \theta$ at the surface equal δq and $\delta \theta$ at h , the above expressions are valid, even if there is non-homogeneous moistening and warming within in the cloud layer and the gradients of dq/dz and $d\theta/dz$ differ locally. The expressions do not depend on η either, but do put some constraints on η . If $\delta q > 0$, one can expect cloud base height to decrease, hence $\delta \eta < 0$. Similarly, if $\delta \theta > 0$, then $\delta \eta > 0$. If temperature and humidity change such that sub-cloud layer relative humidity remains constant, then $\delta \eta = 0$. But are the above expressions still consistent with the sub-cloud layer budget in a new equilibrium?

From the tendency equation for buoyancy we can derive an expression for the sub-cloud layer depth η . In equilibrium, the divergence of the buoyancy flux Q_b within the

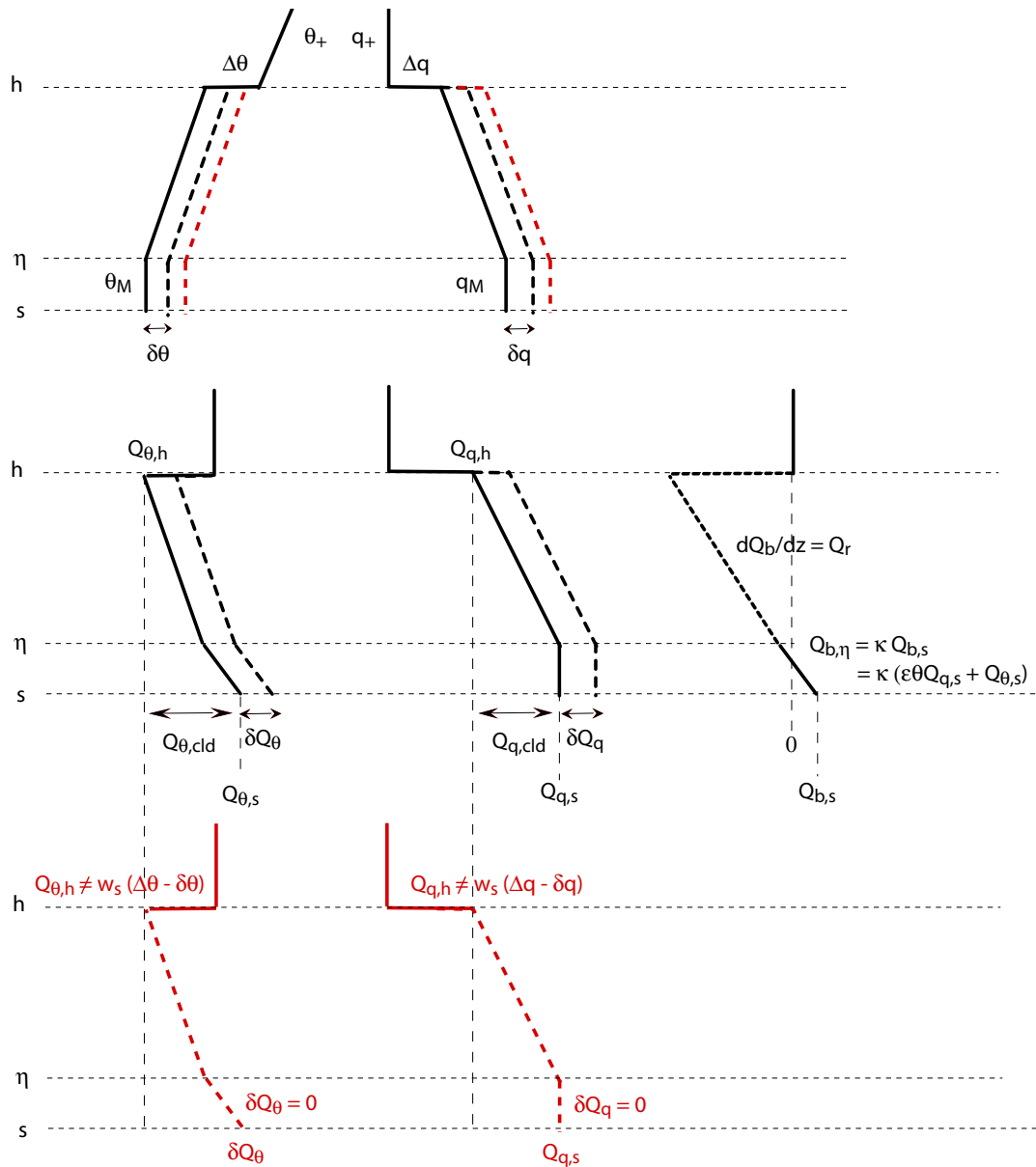


Figure 4.7: Cartoon illustrating the possible response of the temperature and humidity profiles (top) and the heat, moisture and buoyancy flux profile (middle) to a wind speed perturbation of δU , given the assumption that the boundary layer does not deepen. The initial equilibrium state is indicated by solid lines, the possible new equilibrium by dashed lines. Shown in red at the bottom is the response whereby $\delta Q_q, \delta Q_\theta = 0$, which leads to an inconsistency at h .

sub-cloud layer must equal the radiative cooling rate Q_r :

$$\frac{dQ_b}{dz} = \frac{Q_{b,\eta} - Q_{b,s}}{\eta} = Q_r \quad (4.36)$$

where $Q_r < 0$. Using the typical closure whereby the flux at the top of the sub-cloud layer is a fixed fraction κ of the surface flux, this equals:

$$\kappa Q_{b,s} = Q_{b,s} + Q_r \eta \quad (4.37)$$

with $\kappa = -0.2$. In response to a wind speed perturbation of δU , the buoyancy flux is altered by δQ_b and the new equilibrium is:

$$\kappa [Q_{b,s} + \delta Q_b] = [Q_{b,s} + \delta Q_b] + Q_r (\eta + \delta \eta) \quad (4.38)$$

where $\delta Q_r = 0$. This can be rewritten as:

$$\kappa \delta Q_b = \delta Q_b + Q_r \delta \eta \quad (4.39)$$

This equation demonstrates that a situation in which the sub-cloud layer depth does not change with wind speed ($\delta \eta = 0$) can only be true if either $\kappa = 1$ or if $\delta Q_b = 0$. In other words: if the sub-cloud layer depth does not change, the surface buoyancy flux cannot change and vice versa, a result we showed previously in Chapter 4.

If $\delta \eta \neq 0$ however, we can write:

$$\delta \eta = -\delta Q_b \frac{Q_r}{1 - \kappa} \quad (4.40)$$

in which the buoyancy flux can be replaced by a combination of the moisture flux and the heat flux $Q_b \approx Q_\theta + \epsilon \theta Q_q$:

$$\delta\eta = -[\delta Q_\theta + \epsilon\theta\delta Q_q] \frac{Q_r}{1-\kappa} \quad (4.41)$$

Let us imagine a situation with the original surface heat flux equal to zero, because $(\theta_s - \theta_M)$ equals zero. This is the situation present in LES before the wind speed is perturbed. If $Q_{\theta,s} = 0$, then $\delta Q_\theta = 0$, and as such, an increase in wind speed only alters the moisture flux. Hence, Equation 4.41 predicts that the sub-cloud layer depth increases: $\delta\eta > 0$ (recall that both κ and $Q_r < 0$). However, if h does not change (hence $w_s, \Delta q$ and $Q_{q,cl}$ do not change) Equation 4.32 and 4.33 must be true, so that:

$$\delta q = -\frac{\delta Q_q}{w_s}$$

i.e., if $Q_{q,s} > 0$, then $\delta q > 0$: the (sub-cloud) layer will moisten and cloud base height decreases $\delta\eta < 0$. The only way to resolve this inconsistency (the opposite sign of $\delta\eta$) is if the sub-cloud layer would have warmed proportionally. This is impossible however from Equation 4.35 if $Q_{\theta,s} = 0$. Deepening the layer can resolve the contradiction, because it increases the amount of warm and dry air mixed into the layer. The same inconsistency is true when $Q_{\theta,s} > 0$ or < 0 (except when $Q_{\theta,s} < 0$ as well as $Q_{b,s} < 0$ so that Equation 4.34, 4.35 and 4.40 all predict $\delta\eta < 0$, however, an initial buoyancy flux that is negative is rather unrealistic).

This bulk approach may be considered a simplified version of the one-layer bulk model developed by Betts and Ridgway (1989), except that their closure at cloud base height is in terms of temperature, and not buoyancy: $Q_{\theta,h} = \kappa Q_{\theta,s}$. Because in the cases used for the simulations in Chapter 4 and the bulk models in section 5.2 and 5.3, a substantial fraction of the buoyancy flux comes from the moisture flux (the heat flux is

close to zero), using the above formulation makes a difference in terms of how η behaves with wind speed.

If we had used their closure in the above analysis, the term $(\epsilon \theta \delta Q_q)$ would disappear from Equation 4.41. This would imply that in equilibrium the heat flux determines η , and only the additional warming (not the drying) that results from deepening the layer can resolve the inconsistency in $\delta\eta$ that is present if $Q_{\theta,s} = 0$ or > 0 initially. Their solutions are thus more likely to predict a decrease in η with a wind speed increase, which is indeed what happens in the experiments described in their paper. Also note that if $Q_{\theta,s} < 0$ in their model, the layer does not require any deepening regardless of the sign of the buoyancy flux.

4.5. Summary and conclusions

In this chapter we adopted a bulk approach in explaining the response of shallow cumulus convection to wind speed. We first evaluated two different bulk models and their response to a wind speed perturbation (section 4.2 and 4.3). We ended the chapter with a simple graphical illustration and used bulk concepts to explain the general response (section 4.4).

These simple bulk concepts demonstrate why the equilibrium response of the boundary layer to a perturbation in wind speed is one whereby the layer as a whole may deepen. Given certain assumptions, such as a constant radiative cooling and a homogeneous distribution of the warming and moistening throughout the layer, bulk theory demonstrates a contradicting response of the sub-cloud layer depth when the cloud layer does not deepen at stronger winds. Because a large fraction of the buoyancy flux is essentially carried by vapor in the (marine-cumuli) cases studied, a stronger wind speed,

and thus stronger surface evaporation, tend to increase the buoyancy flux. In equilibrium, an increase in the surface buoyancy flux implies an increase in the sub-cloud layer depth. This is inconsistent with a moistening of the layer as a whole, that tends to decrease cloud base height, hence sub-cloud layer depth (the two are assumed to equal in bulk theory). Deepening of the layer would resolve this inconsistency due to additional warming and drying. This would allow the surface evaporation to remain high and the sub-cloud layer depth to be roughly constant.

Because these arguments are independent on the detailed structure of the cumulus layer, and do not require arguments such as how the mass flux and entrainment change in the transient response, it demonstrates that a much simpler bulk model can predict the same equilibrium response as LES. One requirement is that the bulk model includes some representation of the cumulus layer. For example, a mixed-layer model of just the sub-cloud layer does not suffice, because it cannot model changes in the cumulus layer independently (section 4.2). Two well-known models of the cumulus-topped mixed-layer, the model by Betts and Ridgway (1989) (BR89) and by Albrecht et al. (1979), modified by Bretherton and Park (2008) (BP08), both predict that the general response to a wind speed increase is to moisten as well as to deepen the layer.

In BR89 the boundary layer is modeled as a single layer by assuming a mixing line structure in the cumulus layer. It also assumes that the bulk mixing line parameters are constant, by essentially fixing the partitioning between clear and cloudy air a priori, a parameter to which the surface fluxes and sub-cloud layer depth are sensitive (Stevens 2006). This may not be a bad assumption given that in LES the cloud fraction and mixing do not vary much with wind speed. In our bulk explanation (section 4.4), that is based on a similar set of equations used in BR89, we assume that moistening and warm-

ing occurs homogeneously throughout the layer. Although principally our explanation does not exclude the possibility of gradients varying locally within the layer, the extent to which thermodynamic gradients and mixing play a role in determining the transient and equilibrium response, while worth further investigation, appear secondary.

In the two-layer shallow cumulus bulk model by BP08, the cumulus layer is defined separately and its thermodynamics gradients are diagnosed through a set of closure assumptions that involve (penetrative) entrainment at cloud top. Aside from the deepening of the cloud layer in response to wind speed, it also captures some other features of the LES, such as a slightly more stable temperature gradient of θ at stronger winds, a lower heat flux and a negative feedback on updraft buoyancy. However, the model does not seem to realistically capture the dynamics of the sub-cloud layer and the mass flux. The mass flux is largely constrained by closures assumed at the inversion, instead of for instance by allowing the mass flux to depend on cloud fraction and the updraft velocity (a dependency derived from LES that is used as a closure in Neggers et al. (2006)). As such, an increase in the turbulent fluxes at cloud base with wind speed is achieved differently depending on the cloud model (mass flux structure) that is used. Regardless of these differences though, the general response of this model remains a deepening.

Chapter 5

Summary and concluding remarks

Shallow cumulus clouds prevail over much of the world's subtropical oceans in regions that are well-known as the trades. Because these clouds have captivated scientists since the early fifties, their dynamics and influence on the larger-scale environment, as well as the general structure of the boundary layer in which they are embedded, are reasonably well-understood. Recent observational studies continue to contribute to the recognition that cumuli with tops above 3-4 km are not uncommon, and that they can be accompanied by non-negligible amounts of rain, which contribute substantially to the total rainfall over tropical oceans. This has triggered questions as to what extent precipitation and organization affect their overall statistics and behavior. Another reason for the renewed interest in shallow cumulus comes from the climate modeling community. Low-level clouds, particularly shallow cumuli, are not-well represented in global climate models and their contribution to a changing climate is inconsistent among those models. Hence there is a need to improve their parameterization, which asks for a better understanding of their behavior, especially in a varying large-scale environment.

Inspired and motivated by these advances, this dissertation focuses on relationships between precipitating shallow cumulus convection and the large-scale meteorological

environment. Two main questions are addressed: 1) to what extent and how can variability in precipitation from shallow cumulus be explained by variability in meteorology? 2) what is the influence of wind speed on shallow cumulus convection, and can it be understood from simple theoretical considerations?

The first question is explored using data from radar, radiosondes, airborne-lidar and a land-based meteorological station. These data were collected during the Rain In Cumulus Over the Ocean (RICO) field study that took place in a typical trade-wind region during two relatively undisturbed months in the winter of 2004 and 2005. Precipitation during RICO was prevalent and contributed to at least half of the total rainfall observed, confirming old ship observations and more recent studies using TRMM data that indicated that trade-wind cumuli rain frequently. Precipitation did vary substantially on timescales of a few hours to a day. Simultaneous observations of the meteorological environment suggest that subtle fluctuations in the strength of the easterlies and in subsidence played a major role in regulating this variability. In particular the covariability between wind speed, humidity and precipitation stands out.

Such a relationship has been established in several studies of tropical deep convection. A similar relationship for shallow convection however has to our knowledge not been evidently established from observations, nor from simulations. We hypothesized that a wind speed "regime" exists for shallow cumulus as well, wherein winds are a major influence on clouds and rain. Via enhanced evaporation from the ocean's surface, stronger winds increase boundary layer humidity, leading to more and deeper clouds and hence more rain. But in the absence of continual cloud observations during RICO, the interaction between winds, humidity, clouds and rain cannot be confidently established. For instance, it is still uncertain whether a greater rain fraction is caused by clouds be-

ing deeper and/or more slanted due to wind shear, or just by a greater number of clouds present, although a combination of all is not unlikely.

The wind speed hypothesis is also arguable from an aerosol point of view. At times of strong winds one can expect higher concentrations of sea-salt aerosol, which, if corresponding to higher concentrations of cloud droplets (CCN) can suppress collision-coalescence processes and warm rain formation. Such a (negative) relationship between wind speed and precipitation is not evident in RICO observations, suggesting that aerosol effects play a minor role in controlling precipitation from trade-wind cumuli on larger scales.

In Chapter 3 of this thesis, LES is used to bolster our confidence and understanding of the influence of wind speed. The simulations that are performed are somewhat ideal in that they exclude rain microphysics and prescribe zero initial wind shear (note that wind shear does develop in the sub-cloud layer through the course of the simulation, but not in the cloud layer). These simplifications are done to isolate the effect of wind speed on clouds and to minimize numerical errors introduced by advecting the flow at different speeds. In simulations, the response to an increase in wind speed is a deepening of the boundary layer due to deeper clouds, resulting in substantial differences in the inversion height upon reaching stationarity. The boundary layer also warms and moistens, with the moistening most evidently in the sub-cloud layer and to a lesser extent in the cloud layer. The extra moisture supplied by surface evaporation is carried by cumulus updrafts all the way to the top of the cloud layer, resulting in evaporative cooling at the inversion. The extra dry and warm air mixed into the boundary layer from overshooting cumuli and the deepening of the layer maintains a strong surface moisture flux, but lowers the surface heat flux. As such, updraft buoyancy as well as the convective mass flux in

a new stationary state do not differ much from their original values. Moreover, wind speed only affects cloud depth, whereas cloud (core) fraction appears very robust. All simulations show this behavior, regardless of the initial thermodynamic profiles, the amount of subsidence or wind shear that is prescribed.

From an LES point of view, the deepening can be explained from the increased flux of moisture (and mass flux) into the inversion in the transient response, which cannot instantly be balanced by sufficient drying. Arguments involving the mass flux or internal processes such as mixing and entrainment may however not be necessary to explain the deepening response. In Chapter 4 we use simple concepts from bulk theory to demonstrate that a zero deepening leads to a contradiction in the response of the sub-cloud layer depth with wind speed. The explanation only uses the bulk (averaged) values for temperature and humidity in the sub-cloud- and cloud layer and it assumes sub-cloud layer depth equals cloud base height. The inversion is modeled as an infinitely small layer (discontinuity) across which turbulent moistening needs to balance large-scale drying. Given the assumption that the inversion height does not change, it is demonstrated that with a wind speed perturbation, the change in the inversion moisture balance leads to a change in cloud base height that is inconsistent with the change in the buoyancy budget of the sub-cloud layer. This inconsistency may be resolved by deepening the layer. Well-known bulk models of the trade-wind layer represent the cumulus layer in different ways, either through a mixing line assumption or through the use of an entraining-detraining plume model. All these models predict a deepening response to wind speed.

Exactly how much deepening takes place and by how much the surface fluxes have changed upon reaching a new equilibrium, depends on whether an equilibrium is in fact

reached, and on the prescribed profiles of subsidence, humidity and temperature. Our work suggests a very limited regime in which equilibrium solutions can be obtained *i.e.*, solutions whereby the thermodynamic structure in the sub-cloud and cloud layer does not change noticeably (stationarity) and whereby boundary layer growth is zero. In most of our cases, in particular those at stronger winds, cumuli continue to deepen over the course of the simulation (1-4 days). The absence of an equilibrium solution also seems to complicate the use of bulk (equilibrium) models to address our questions *i.e.*, we appear to be pushing limits trying to obtain solutions for which the inversion height is much beyond 3 km. This calls for a more in depth understanding of the dynamics of cumulus congestus.

If an equilibrium is reached however, the change in surface fluxes may be guessed based on the large-scale drying (and warming) profile, that depend on subsidence and the free-tropospheric profiles of humidity and temperature. When boundary layer growth is zero, the drying flux balances the turbulent moisture flux at the inversion. In a bulk approach, the moisture flux at the inversion is an approximately linear function of the surface moisture flux. If clouds grow into a region where large-scale drying increases (for instance due to increased subsidence), the surface moisture flux in equilibrium may be larger as well.

As of yet our theoretical considerations neglect precipitation and one may ask to what extent including it changes our conclusions. Precipitation is known to limit boundary layer growth and it can affect sub-cloud layer thermodynamics when it evaporates below cloud base. If we would have included precipitation in the simulations, the differences in inversion height with wind speed would be reduced. Evaporative cooling would lead to relatively more moistening and less warming of the sub-cloud layer. This

in turn would limit the surface moisture flux and enhance the surface heat flux. This effect on the surface fluxes may be amplified because of less warming and drying of the layer due to reduced boundary layer growth. Precipitation hence stabilizes the solution by making it less sensitive to perturbations.

Precipitation during RICO was on average 30 W m^{-2} , which is roughly half of the change in surface moisture flux from a $3\text{-}5 \text{ m s}^{-1}$ surface wind speed increase. According to the observations, such a change could move a non-raining case to a raining one. Precipitation effects may therefore not be insignificant. They may partly offset the response of the surface fluxes to a wind speed perturbation that is yet present in our simulations. In fact, this would bring the simulations closer to the observations that show little change in the surface fluxes with rainfall.

Establishing relationships between cloud properties and precipitation, using simulations that include precipitation wisely, as well as resolving the remaining discrepancies between the observations and the simulations, are all important next steps in our attempt to unravel the interplay between factors that impact shallow cumulus. Enough puzzles remain to get excited for yet another field campaign.

Appendix A

Sensitivity to the Galilean transform

A.1. Introduction

The Galilean transform allows computations to be performed within a frame of reference that moves at a velocity that is approximately the domain-averaged mean wind. It is often applied in Large-Eddy-Simulation to allow the use of a larger time step at the same Courant-Friedrich-Levy (CFL) number. It has been shown to reduce finite differencing errors and loss of turbulent energy at high wavenumbers that arise when the mean wind speed is large. In LES the Galilean transform involves subtracting a (Galilean) velocity from the wind components, so that only deviations from that velocity are carried around, except in computing the surface heat, moisture and momentum fluxes. The caveat is choosing a Galilean velocity that does not result in larger differencing errors at for instance the surface, when using the vertically-averaged wind, or elsewhere. This problem is even larger for simulations in which considerable wind shear is present. Often a velocity is used that is half, or some other fraction, of the geostrophic (large-scale) wind. Another caveat is that a larger time step reduces the accuracy of the solution.

This appendix explores the effect of the Galilean transform (or CFL number) on

statistics of cloud and precipitation in LES of shallow cumulus. The main idea is that the Galilean transform also reduces numerical dissipation of scalars, such as liquid water. The LES code we use is the UCLALES. It uses some blend of a second order central difference and upwind advection for scalars (the MUSCL flux-limiter). Momentum advection is fourth-order central. Time stepping in version 3 of the code is done with a third-order Runge Kutta scheme, whereas version 2 uses a blend between forward and leap-frog time differencing. Our emphasis here is on version 3 of the code.

The shallow cumulus case used is the RICO case, that prescribes a mean wind shear in the zonal wind component. Initial profiles and a case description are given in section 2 of Chapter 3 (see also Figure 3.1 and Table 3.1). The Galilean velocity that is used is the vertically averaged-wind: $u = -5 \text{ m s}^{-1}$ (zonal wind component) and $v = -4 \text{ m s}^{-1}$ (meridional wind component). Unless otherwise noted, the domain is 12.8 by 12.8 by 5 km with a horizontal resolution of 100 m and a vertical resolution of 40 m. Time increments are either 4 or 1 second, but time-stepping is adaptive as to keep the CFL number at a maximum of 0.5. The total duration of the simulations is 12 hours and statistics are calculated over hours 6 to 12. Cases are performed with and without the Galilean transform (G versus NG). Most cases are performed without micro-physics, as to explore the effect of the transform on the cloud field first.

We acknowledge that this case is rather complex and that for isolating the sole effect of the transform idealized cases are better suited. Such cases (for instance, 2D simulations without wind shear and with just a single cloud) were explored and overall show the same sensitivity of cloud amount and precipitation that is evident in results of 3D simulations presented here.

UCLA-LES	Simulation	$\Delta x, z$ [m]	Δt [s]	CFL	L [gm^{-2}]	z_i [m]	C [-]	R [gm^{-2}]	P_{sfc} [Wm^{-2}]	N_r [dm^{-3}]
3.0	NG	100,40	4	0.50	7.6	1915	0.08			
3.0	G	100,40	4	0.50	8.1	1839	0.10			
3.0	NG	100,40	1	0.19	6.8	1912	0.08			
3.0	G	100,40	1	0.17	8.7	1862	0.10			
3.0	NG	50,25	1	0.31	7.1	1815	0.10			
3.0	G	50,25	1	0.28	9.0	1780	0.13			
3.0	NG no limiters	100,40	1	0.20	8.6	1845	0.12			
3.0	G no limiters	100,40	1	0.17	10.7	1813	0.16			
3.0	NG precip	100,40	1	0.20	8.4	1926	0.09	0.65	0.5	18.4
3.0	G precip	100,40	1	0.17	8.4	1835	0.11	0.23	0.1	14.8
2.0	NG	100,40	4	0.40	8.6	1904	0.09			
2.0	G	100,40	4	0.40	7.9	1839	0.10			
2.0	NG	100,40	1	0.37	8.2	1902	0.09			
2.0	G	100,40	1	0.34	8.2	1837	0.11			
2.0	NG	50,25	1	0.40	8.7	1822	0.11			
2.0	G	50,25	1	0.39	9.5	1771	0.13			

Table A.1: Sensitivity to Galilean transform (NG = no transform, G = galilean transform) as well as resolution, time step and use of limiters for scalar advection for UCLA-LES version 2.0 (leapfrog) and version 3.0 (runge-kutta). All simulations are without micro-physics, unless denoted by *precip*, in which case cloud droplet number concentrations equal $N_c = 70 \text{ mg}^{-1}$. Variables are averages over the last six hours of each simulation (12 hours in total) and represent: CFL number, cloud (liquid) water path L , inversion height z_i , fraction of cloudy columns C , rain water path R , surface rain rate P_{sfc} and rain-drop number concentrations averaged over raining regions only N_r .

A.2. Results

a. *Thermodynamics and cloud properties*

A sensitivity to the transform is most apparent in the domain-averaged cloud top liquid water r_c (Figure A.1). Simulations with the transform (G) have more liquid water at all levels, but the differences are most pronounced at cloud top (Figure A.1). Smaller though noticeable differences are present in the mean profiles and variances of thermodynamic quantities and the wind components. The galilean transformed simulations also tend to develop a sharper inversion, an effect that gets more pronounced at higher resolution. This is evident from larger gradients of temperature and humidity $d\theta/dz$ and dr_t/dz across the inversion (not shown) as well as the lower inversion height z_i for the G simulations shown in Table A.1. Other differences include a higher liquid water path LWP (exceptions are the low resolution simulations with version 2) and higher total cloud fraction C .

Generally, less numerical diffusion leads to more cloud-top liquid water and a shallower but sharper inversion, which is presumably the effect seen here. Consequently, one may also expect that the liquid water amount averaged over just cloudy regions is higher for the G simulations. However, this appears not to be the case from the right and uppermost panel in Figure A.2 and A.3, that plots the in-cloud liquid water $r_{c,cloud}$. Because global cloud water (averaged over the entire domain) *i.e.*, r_t shown in Figure A.1, does exhibit a difference, this must imply that the total number of clouds present in the G simulations is larger. This result is still somewhat puzzling. A larger number of clouds is however consistent with clouds being on average less vigorous, with smaller updraft (vertical) velocities, in the G simulations (Figure A.3 d)).

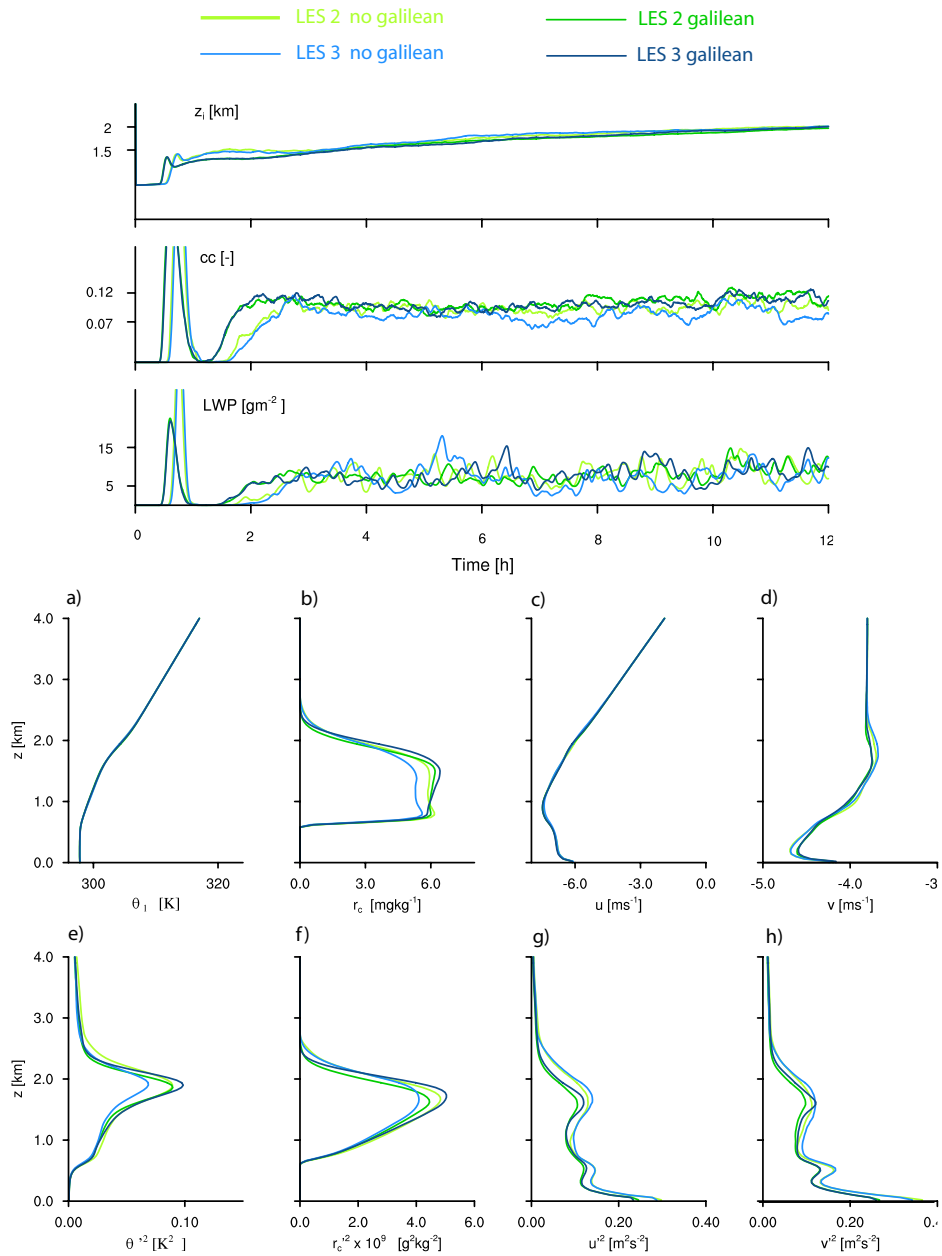


Figure A.1: Top panels show time series of inversion height z_i , total number of cloudy columns cc and liquid water path LWP for simulations with LES version 2 (green) and version 3 (blue) either without (lighter colors) or with (dark colors) a galilean transform. Lower panels show corresponding six hour averaged profiles of (from left to right, top to bottom) potential temperature θ_l , liquid (cloud) water r_c , zonal u and meridional v wind speed, and their variances.

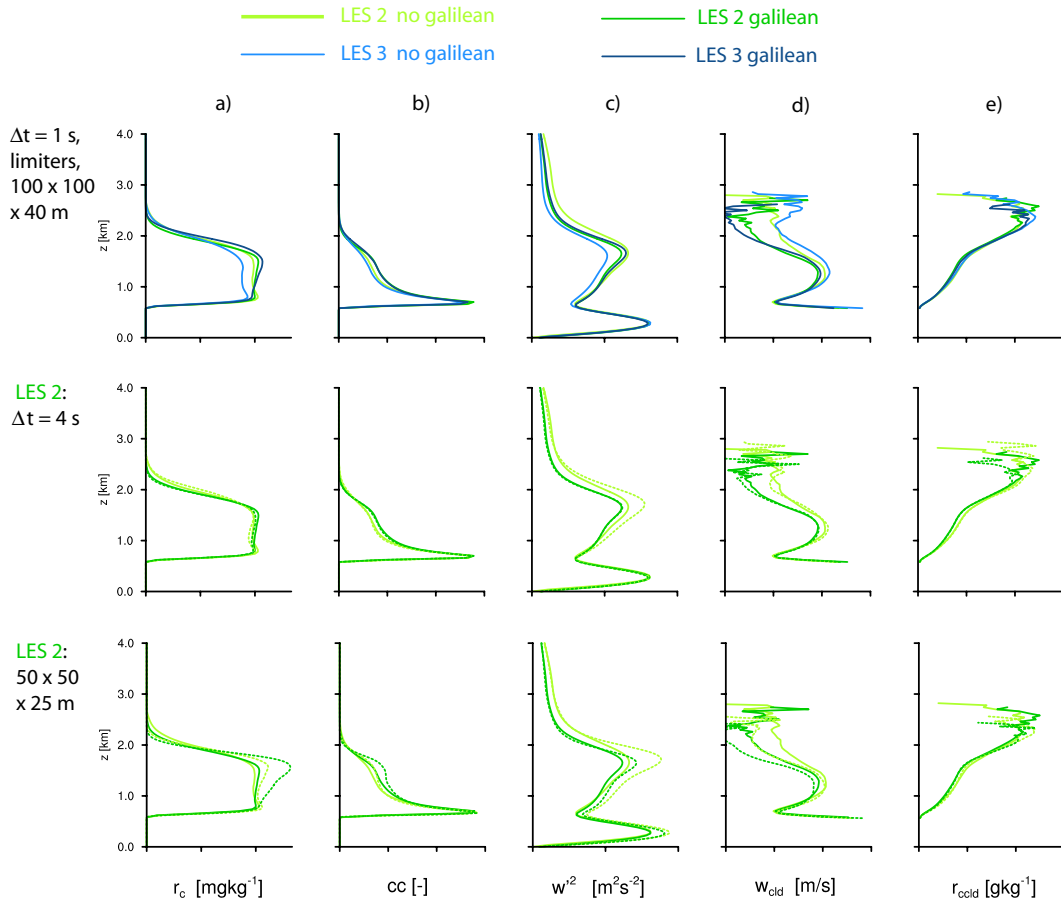


Figure A.2: Six hour averaged profiles for liquid (cloud) water r_c , cloud fraction cc , vertical velocity variance w'^2 , in-cloud vertical velocity (updraft speed) w_{cld} and in-cloud liquid (cloud) water $r_{c,cld}$. Top panel shows the base simulation with $\Delta t = 1$ s, limiters and 100 by 100 by 40 m resolution (colors as in Figure A.1). Lower panels show the base simulations (solid lines) versus simulations with a longer time step, higher resolution, or without limiters (dashed lines).

Test studies performed with a 2D version of the code (not shown), that generally show a much higher sensitivity to the galilean transform, indicate that the first differences arise in the vertical velocity and its variance within the subcloud layer, most evidently around cloud base. These are then followed by differences in (global) liquid water and cloud fraction. The sensitivity in 2D runs reduces with a smaller timestep. One hy-

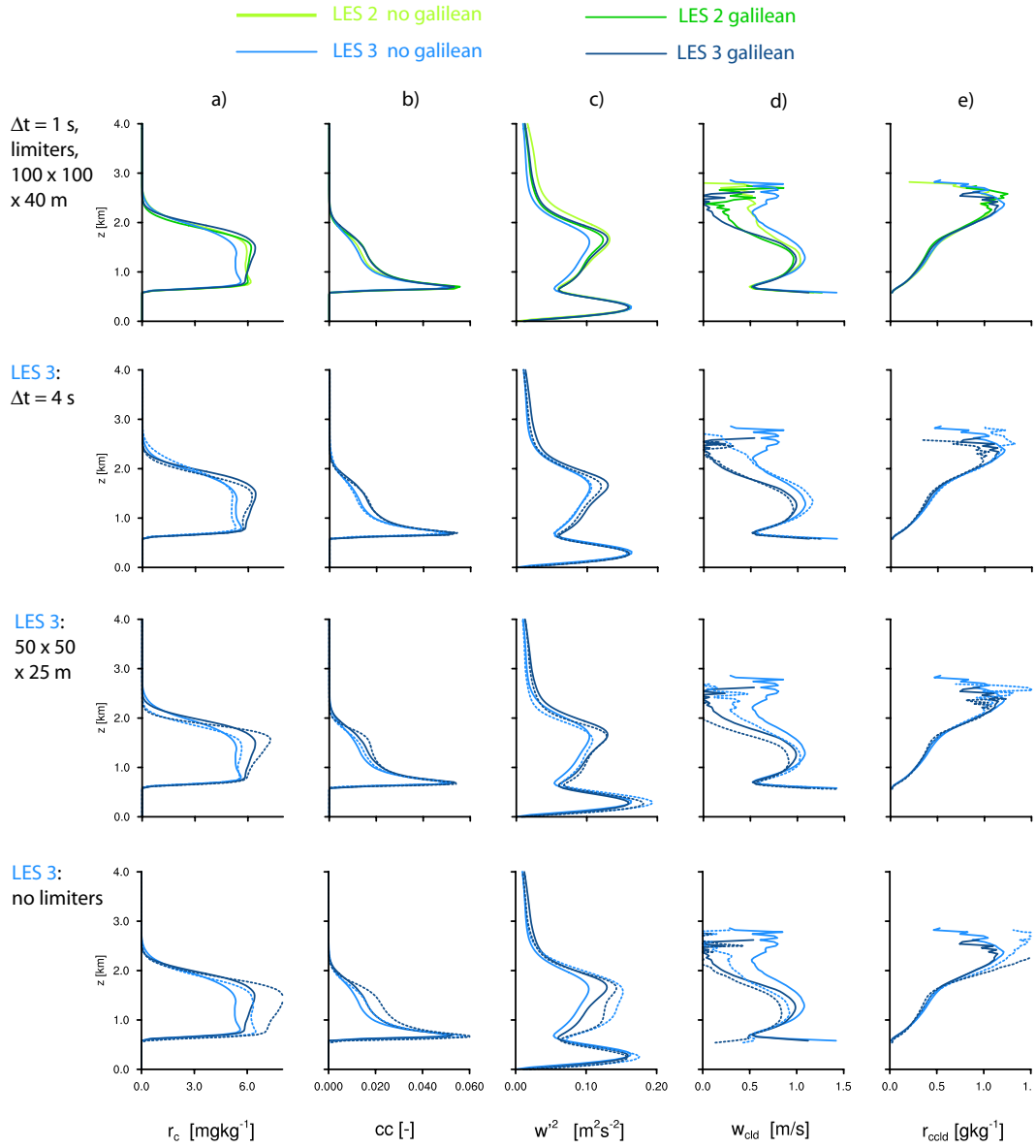


Figure A.3: Labels as in Figure A.2, but for UCLA-LES version 3.0.

pothesis is that the stronger updrafts may be caused by increased maxima and minima ('ripples') developing within the flow when no transform is used (NG). This may lead to higher vertical velocities, a greater CFL, and a greater vertical velocity variance.

A sensitivity of the vertical velocity variance to the galilean transform is indeed present in our results (all middle panels in Figure A.3c)), but depends on the LES version, on the resolution and the time increment used. Results for simulations in which the time increment or resolution is varied are shown as the dotted lines in the other panels/rows of Figure A.3, where the solid lines always correspond to the (reference) case with a 1 s time increment (the uppermost panels). Simulations with a 1 and 4 s time increment for version 3 indicate a lower vertical velocity variance in the cloud layer for the NG simulation (opposite to what we just hypothesized). However, using version 3 of the code with limiters turned off reverses the response, and at higher resolution it does exhibit a larger vertical velocity variance below cloud base (≈ 600 m) for the NG runs. Version 2 always exhibits a greater variance for the NG runs.

A positive result is the overall lack of sensitivity to the time step refinement in both versions of the code. As for the sensitivity to finer resolution, opposing effects may be at play. Less numerical diffusion at finer resolution would lead to more cloud-top cloud amount, but because smaller eddies, that are responsible for entrainment, are better resolved at finer resolution, clouds tend to be more dilute (*i.e.*, have less liquid water). Numerical dissipation appears dominant in our results, because there is little difference in cloud-averaged liquid water $r_{c,cl}$ (Figure A.3e).

Overall one can argue that absolute differences in cloud amount are not that large here. Our results do demonstrate the susceptibility of cloud statistics changing substantially with advection, a result that is well-known among the LES community. A range of 10-20 % in cloud fraction for different LES codes and different advection schemes is not uncommon.

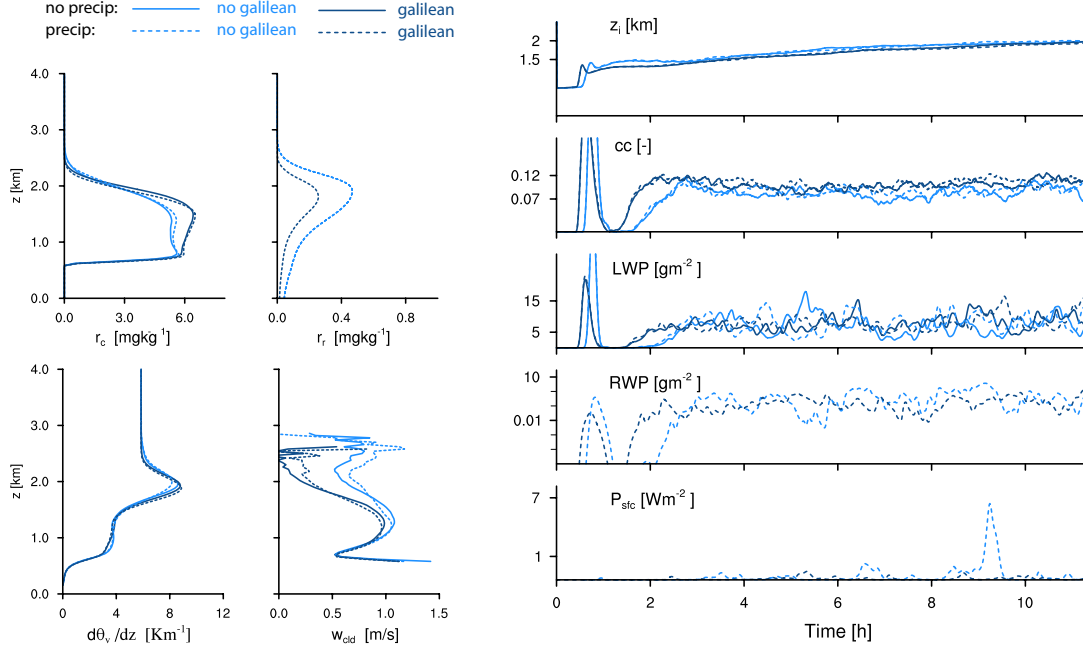


Figure A.4: Left panels show six-hour averaged profiles of cloud water r_c , rain water r_r , gradient of virtual potential temperature $d\theta_v/dz$ and updraft speed w_{cld} . Rightmost panels show time series of inversion height z_i , total number of cloudy columns cc , liquid (cloud+rain) water path LWP , rain water path RWP and surface precipitation P_{sfc} .

b. Precipitation

The impact of the galilean transform on cloud amount translates in somewhat scary differences in precipitation, especially in the domain-averaged rain water r_r and surface precipitation rates P_{sfc} (Figure A.4). Because the simulations used here are run for 12 hours, more significant precipitation has not yet developed. The rain amounts in Figure A.4 and Table A.1 are therefore smaller than the typical values reported in LES studies of the RICO case. Somewhat surprisingly, the galilean transformed simulation produces less precipitation than the simulation without a transform, even though total

cloud amount is larger. This may be explained by the less strong updrafts and somewhat shallower clouds that develop in this simulation. It also demonstrates how extremely sensitive precipitation is to very small differences in for instance here, mean cloud depth and updraft strength. We should note that an opposite response of precipitation to the galilean transform is noted in simulations performed with another LES code (DALES), and with a second-order strictly non-dissipative scheme (by Harlow and Welch) implemented in the UCLALES (George Matheou, personal communication). Regardless of the sign of the response though, the differences in precipitation in our simulations as well as in others, in particular the differences in precipitation rates at the surface are by far the most pronounced of all statistics that are impacted by the galilean transform.

Appendix B

Turbulence effects on warm rain autoconversion in Large-Eddy Simulation

B.1. Introduction

The following is an excerpt of a manuscript titled: "Turbulence effects on warm-rain autoconversion", by Axel Seifert, Louise Nuijens and Bjorn Stevens. The manuscript is submitted to the Quarterly Journal of the Royal Meteorological Society and currently in the review process. The manuscript describes a new parameterization of rain formation in warm clouds that includes the effects of turbulence on the collision rate of droplets in a cloud and is developed by the first author, Axel Seifert.

Small cloud droplets grow mainly by condensation, whereas larger cloud droplets are also created by collision of droplets. The collision process depends largely on the gravitational sedimentation of the droplets *i.e.*, bigger droplets fall faster and collect smaller and slower droplets within their swept volume. Depending on the flow field around the droplets, not all droplets in the geometrical swept volume are collected, an effect which is described by the collision efficiency. For droplets with radii roughly

between 10 and 50 μm , the collision-coalescence process can be increased by turbulence in several ways. It can modify the relative velocity between colliding droplets, it can lead to spatial inhomogeneities in droplet concentration, or it can influence the flow field around droplets and modify the collision efficiency.

The paper describes and tests a new parameterization that is based on the warm rain scheme of Seifert and Beheng (2001), but yet extended to a turbulent flow with explicit dependencies on the turbulent dissipation rate ϵ and the Taylor microscale Reynolds number Re_λ . Using a 1D kinematic cloud model the paper shows that already moderate turbulence with dissipation rates of $400 \text{ cm}^2 \text{ s}^{-3}$ can lead to a significant speed-up of the rain formation corresponding to an increase in the autoconversion rate by a factor 4-6 depending on the size of the droplets.

The last section of the paper, that is included here with a few adaptations, describes the implementation of the new parameterization in Large-Eddy-Simulation (LES) and discusses the following questions: What is the impact of turbulence-enhanced coalescence when implemented in bulk microphysical parameterizations used in models such as LES? Does it lead to pronounced differences in precipitation and cloud properties on scales much larger than a single cloud?

B.2. Turbulence effects in LES

For our study we use the latest version of the UCLA LES (Stevens et al. 2005; Stevens 2007). It differs from earlier versions through its incorporation of a fourth-order Runge-Kutta scheme instead of a blend between forward and leapfrog time-differencing. The model solves prognostic equations for the velocity vector (u, v, w) , the total water mixing ratio r_t , liquid water potential temperature θ_l , the mass mixing ratio of rain water r_r

and the mass specific number of rain-water drops n_r . The cloud water mixing ratio r_c is diagnosed from r_t and the saturation mixing ratio r_s so that: $r_c = \max(0, r_t - r_r - r_s)$. The default bulk microphysical scheme of the UCLA LES model is the one from Seifert and Beheng (2001).

The turbulence-enhanced coalescence is implemented in the LES by allowing the autoconversion and accretion parameters k_{cc} and k_{rr} to be a function of the dissipation rate ϵ , mixing length ℓ and Taylor-Reynolds number Re_λ . Rather than prescribing fixed values for these parameters (as is done when testing the kinematic 1-D cloud model), they are directly obtained from the sub-grid scale (SGS) turbulence model used by the LES. For the UCLA LES this is the Smagorinsky-Lilly model. In this model the turbulence kinetic energy e , eddy viscosity K_m and the mixing length ℓ are related by:

$$e^{1/2} = \frac{K_m}{C_s \ell}, \quad (\text{B.1})$$

where $C_s = 0.23$ is the Smagorinsky constant. The mixing length ℓ is taken as the geometric average between the LES grid scale and a length scale proportional to the height above the surface z :

$$\ell^{-2} = (\Delta x \Delta y \Delta z)^{-2/3} + (z\kappa/C_s)^{-2} \quad (\text{B.2})$$

with $\kappa = 0.35$ as the von Kármán constant. Such an average was shown by Scotti et al. (1993) to be an appropriate choice for anisotropic grids. The eddy viscosity K_m is calculated as:

$$K_m = (C_s \ell)^2 S \sqrt{1 - \frac{Ri}{Pr}} \quad \text{where} \quad Ri = \frac{S^2}{N^2} \quad (\text{B.3})$$

$Pr = 0.33$ is the eddy Prandtl number and S^2 and N^2 are the strain rate factor and Brunt-Vaisala frequency. From e and ℓ , the local (turbulent) energy dissipation rate, ϵ ,

can be calculated from

$$\epsilon = c \frac{e^{3/2}}{\ell} \quad \text{with} \quad c = 0.93. \quad (\text{B.4})$$

where 'local' here refers to scales on the size of an LES grid box. The Taylor-microscale Reynolds number Re_λ can be estimated from the following expression, using some assumptions on homogeneous turbulence Siebert et al. (2006b):

$$Re_\lambda = \frac{6}{11} \left(\frac{\ell}{c} \right)^{2/3} \left(\frac{15}{\nu} \right)^{1/2} \epsilon^{1/6}. \quad (\text{B.5})$$

where ν is the kinematic viscosity. At each time step within LES ϵ as well as Re_λ are used to calculate the autoconversion and accretion parameters k_{cc} and k_{rr} .

Local dissipation rates in LES of shallow cumulus seem to be generally around 10-100 cm s^{-3} in clear air and incipient or decaying cloud elements, but can reach values up to a few thousand cm s^{-3} within the top of developing, vigorous clouds (not shown here). Assuming that the effect of turbulence on coalescence processes saturates at high energy dissipation rates, and based on observations where maximum in-cloud dissipation rates are on the order of about 100 cm s^{-3} (Siebert et al. 2006a) (though the observed cumuli in these cases were generally less vigorous than the cumuli simulated here), we set an upper limit of ϵ to 600 cm s^{-3} when calculating k_{cc} and k_{rr} . Hence, if anything our estimates of turbulence effects are likely to be somewhat conservative.

The initial data for the simulations are based on a moister version of the standard precipitating shallow cumulus case that was constructed by the GCSS* boundary layer working group, based on the Rain In Cumulus over the Ocean (RICO) field study (Raubert et al. 2007). This modified moister version was first used by Stevens and Seifert (2008), to which we refer for a detailed set-up of the case. All simulations use a domain

*GEWEX (Global Energy and Water Experiment) Cloud System Studies

of $19.2 \text{ km} \times 19.2 \text{ km} \times 5 \text{ km}$, with a grid spacing of 100 m in the horizontal and 40 m in the vertical, unless otherwise noted. The model time step is variable, with a maximum Courant number of 0.5. Because we are using a new version of the UCLA LES, the reference case with drop concentrations of 70 cm^{-3} was first compared to the earlier version of the model Stevens and Seifert (2008). Although the baseline simulations show small quantitative differences from what was reported by Stevens and Seifert (2008) the general behavior is similar, and well within the range one would expect based on small changes to the numerics. The simulations we analyze for this study are thus based on the new model version with turbulence-enhanced (T) and non-turbulence enhanced (NT) coalescence at cloud number mixing ratios of $N_c = 70, 140$ or 300 cm^{-3} , with a focus on the high concentrations, so as to explore the role of turbulence in situations where rain production might otherwise not be favored.

Does including turbulence effects matter? In terms of its impact on domain-averaged precipitation in LES, our results suggest they do. The CCN cases shift from producing very little surface precipitation in the 140 cm^{-3} case (hardly visible in Fig. B.1), to quite moderate and at times intense rainfall comparable to or even stronger than the rainfall produced in the 70 cm^{-3} non-turbulent case. The practically non-raining case with 300 cm^{-3} case shifts to a lightly raining case (Fig. B.1).

Except for the 70 cm^{-3} case, rain amounts at higher drop concentrations appear too small to significantly affect cloud and boundary layer characteristics (Table B.1) in terms of the time-averaged fraction of cloudy columns, denoted by C , or the inversion height z_i (estimated as the height of the maximum θ_v gradient). The differences among all simulations are consistent with the finding that more precipitation over a long time period leads to a shallower boundary layer (Stevens and Seifert 2008). In terms of different

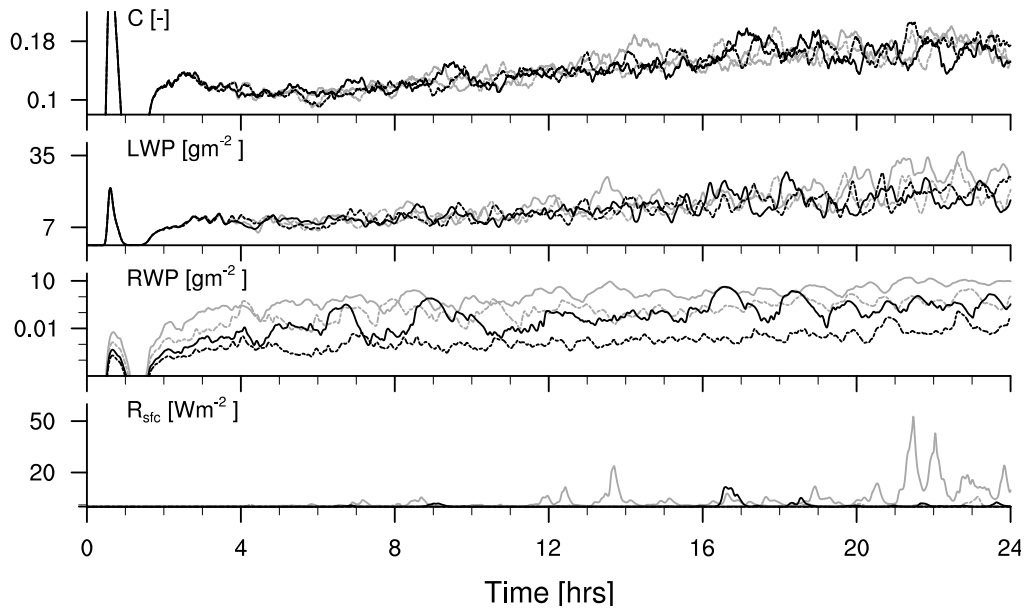


Figure B.1: Time series of the number of cloudy columns (cloud fraction) C , liquid (cloud + rain) water path L , rain water path R and surface rain-rate R_{sfc} for simulations with cloud droplet number concentrations N_c of 140 cm^{-3} (grey) and 300 cm^{-3} (black), without turbulence-enhanced coalescence (dashed line) and with turbulence-enhanced coalescence (solid line)

rain measures though, such as time-averaged rain water paths, R , the maximum value of rain rate within the time-averaged vertical profile of rain, R_{max} , or the conditionally averaged rain drop number concentration over grid-cells where $r_r > 1 \text{ mg kg}^{-1}$, N_r , the impact of turbulence is clearly evident.

One of the reasons that turbulence-enhanced coalescence has such a noticeable effect may be the collocation of regions that generally experience the highest energy dissipation rates (in cloud core and cloud-top of actively developing clouds) with those regions where the biggest raindrops naturally develop first *i.e.*, in regions with the highest liquid water at cloud-top, where increased coalescence would thus be most beneficial. This is evident in Fig. B.2 where the cross section of a typical cumulus cloud is taken from

Table B.1: Sensitivity to turbulence-enhanced coalescence T, versus no turbulence enhancement NT, for cloud droplet number concentrations $N_c = 70, 140$ and 300 mg^{-1} . NT-140-hr and T-140-hr represent simulations with doubled horizontal resolution (grid spacing of 50 m). Variables are cloud (liquid) water path L , rain water path R , inversion height z_i , fraction of cloudy columns C , rain-drop number concentrations averaged over raining regions N_r , surface rain rate R_{sfc} and the maximum rain-rate R_{max} within the (domain-averaged) profile of rain-rate. All variables are averaged over the last four hours of each simulation.

Run	L	R	z_i	C	R_{sfc}	R_{max}	N_r
	[gm^{-2}]	[gm^{-2}]	[m]	[-]	[Wm^{-2}]	[Wm^{-2}]	[dm^{-3}]
NT-70	18.6	7.0	2418	0.17	8.6	16.6	19.7
T-70	19.3	22.2	2358	0.15	43.3	51.6	26.6
NT-140	18.9	0.8	2449	0.17	0.8	2.0	8.7
T-140	19.7	8.3	2422	0.17	13.2	18.8	14.9
NT-140-hr	21.1	1.0	2422	0.21	1.1	2.6	8.9
T-140-hr	21.9	3.9	2399	0.21	4.9	9.9	10.9
NT-300	20.2	0.0	2442	0.17	0.0	0.0	4.7
T-300	18.3	0.4	2438	0.16	0.4	0.9	6.4

a simulation. The figure also emphasizes how poorly the LES resolves the internal microstructure of such shallow cloud, emphasizing that the detailed interaction of turbulence and microphysics likely requires a ten, or perhaps hundred fold, increase in resolution before the fine-structure of such shallow clouds is adequately resolved.

Thus it is not surprising that, as discussed in Stevens and Seifert (2008), a sensitivity to resolution remains, with somewhat less precipitation at a finer (50 m) resolution (the T-140-hr run). At higher resolution the clouds tend to be more dilute (with less cloud-core liquid water), whereas less numerical diffusion leads to more cloud-top cloud amount, and a somewhat shallower but sharper inversion height. Despite this sensitivity, the general response of the simulation to the incorporation of turbulence effects on droplet coalescence rates is robust. Even so, based on Fig. B.2 the possibility re-

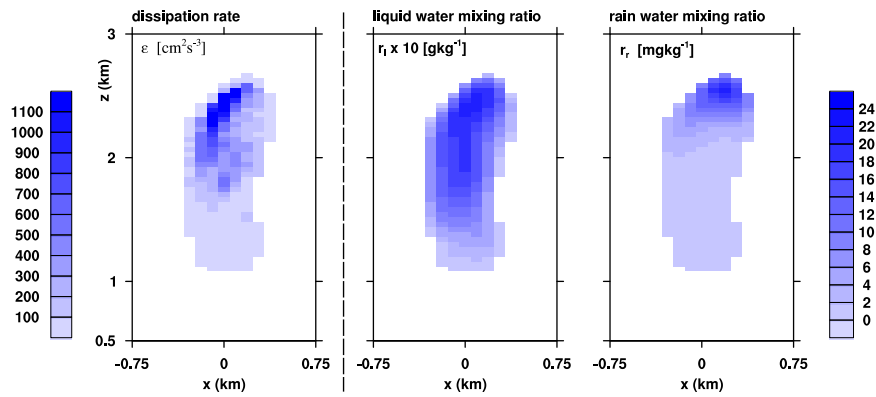


Figure B.2: Snapshot of the initial development of precipitation in a typical cumulus cloud from the LES. Shown from left to right are the dissipation, cloud-water mixing ratio and rain-water mixing ratio. The latter two share the color bar on the far right.

mains that this picture changes once LES begins to resolve the fine internal structure of evolving clouds.

Appendix C

The shallow cumulus bulk model by Bretherton and Park

C.1. Prognostic equations

The shallow cumulus bulk model by Bretherton and Park (2008) (BP08) solves five prognostic equations for θ_{vl} and q_t in the subcloud layer 'M', for θ_{vl} and q_t at the cloud layer midpoint 'H' and for the inversion height (p_I).

Within the subcloud layer, θ_{vl} is solely determined by the surface heat flux and radiative cooling rate Q_r *i.e.*, there is no source of θ_{vl} due to entrainment, or loss due to convective mass flux M_{cB} (recall that $\Delta_B \theta_{vl} = 0$). q_t in the subcloud layer is forced by the turbulent moisture fluxes at the surface and at the top, as well as large-scale subsidence ω_B that works on the cloud-base humidity jump $\Delta_B q_t$.

$$\frac{d\theta_{vlM}}{dt} = -\frac{\omega_{tS} \Delta_S \theta_{vl}}{\Delta p_B} - Q_r \quad (\text{C.1})$$

$$\frac{dq_{tM}}{dt} = -\frac{\omega_{tS} \Delta_S q_t + [\omega_B + gM_{cB} + c_{vl} d\theta_{vlM}/dt]/\Delta_B q_t}{\Delta p_B + c_{qt} \Delta_B q_t} \quad (\text{C.2})$$

$$(\text{C.3})$$

where $\Delta p_B = (p_S - p_B)$ is the subcloud layer thickness, $\omega_{tS} = \rho_S g C_T U$ is the surface transfer velocity, $\Delta_S \theta_{vl}$ and $\Delta_S q_t$ are the temperature difference ($\theta_{vlM} - \theta_{vlS}$) respectively humidity difference ($q_{tM} - q_{tS}$) between the surface and subcloud (mixed-layer), and c_{vl} and c_{qt} are thermodynamic quantities whose full derivation is included in the appendix of BP08.

In the cumulus layer, temperature and humidity tendencies both depend on the turbulent flux divergence across a layer with thickness $\Delta p_C = p_B - p_I$, radiative cooling and large-scale warming and drying that depends on the (subsidence) vertical velocity at its midpoint H ω_{eH} :

$$\frac{d\theta_{vlH}}{dt} = \frac{g M_{cB} f_{vlI}}{\Delta p_c} - Q_r + \omega_{eH} \gamma_{vl} \quad (\text{C.4})$$

$$\frac{dq_{tH}}{dt} = \frac{g M_{cB} (-\Delta_B q_t - f_{qtI})}{\Delta p_c} + \omega_{eH} \gamma_{qt} \quad (\text{C.5})$$

where f_{vlI} and f_{qtI} are the fluxes of heat and moisture into the inversion that depend on the cumulus excess of temperature $\tilde{\theta}_{vlI}$ and of humidity \tilde{q}_{tI} :

$$f_{vlI} = g m_I \tilde{\theta}_{vlI} = g m_I (\theta_{vlcI} - \theta_{vlI}) \quad (\text{C.6})$$

$$f_{qtI} = g m_I \tilde{q}_{tI} = g m_I (q_{tcI} - q_{tI}) \quad (\text{C.7})$$

where m_I is the (non-dimensional) mass flux at the inversion *i.e.*, $m_I = M_{cI}/M_{cB}$.

Lastly, the pressure tendency at the inversion is determined by the subsidence velocity, ω_I , and the penetrative entrainment velocity ω_{eI} , that acts to deepen the layer:

$$\frac{dp_I}{dt} = \omega_I - \omega_{eI} \quad (\text{C.8})$$

C.2. Cloud model

In BP08 a simple bulk plume with constant fractional entrainment ϵ and detrainment δ is used:

$$\frac{1}{M} \frac{dM}{dp} = -(\epsilon - \delta) \quad (\text{C.9})$$

Integrating this equation over the cumulus layer, from cloud base (B) to the inversion (I), gives:

$$m_I = \exp [(\epsilon - \delta) \Delta p_C] \quad (\text{C.10})$$

where $\Delta p_C = p_B - p_I$ is the pressure thickness of the layer. Taking q_t as an example, the cumulus excess at the inversion \widetilde{q}_{tI} takes the form:

$$\widetilde{q}_{tI} = -G_I \gamma_{qt} - b_I \Delta_B q_t \quad (\text{C.11})$$

where γ_{qt} is the cumulus layer q_t gradient. Expressions for the non-dimensional parameter b_I and the parameter G_I can be derived from the gradient of $\widetilde{q}_t = q_{tc} - q_t$ within the cumulus layer:

$$\frac{d\widetilde{q}_t}{dp} = \frac{dq_{tc}}{dp} - \frac{dq_t}{dp} = \epsilon \widetilde{q}_t + \gamma_{qt} \quad (\text{C.12})$$

Rearranging Eq.C.12:

$$\frac{d\widetilde{q}_t}{\epsilon \widetilde{q}_t + \gamma_{qt}} = dp \quad (\text{C.13})$$

and integrating it over the cumulus layer:

$$\int_{p_B}^{p_I} \frac{d\widetilde{q}_t}{\epsilon \widetilde{q}_t + \gamma_{qt}} = \int_{p_B}^{p_I} dp$$

$$\ln \left(\frac{\epsilon \widetilde{q}_{tI} + \gamma_{qt}}{\epsilon \widetilde{q}_{tB} + \gamma_{qt}} \right) = -\epsilon \Delta p_C$$

gives an expression for \widetilde{q}_{tI} :

$$\begin{aligned}\widetilde{q}_{tI} &= -\frac{\gamma_{qt}}{\epsilon} + \frac{1}{\epsilon}(\epsilon \widetilde{q}_{tB} + \gamma_{qt}) \exp[-\epsilon \Delta p_C] \\ &= -\frac{(1 - \exp[-\epsilon \Delta p_C])}{\epsilon} \gamma_{qt} - \exp[-\epsilon \Delta p_C] \Delta_B q_t\end{aligned}\quad (\text{C.14})$$

where we use $\widetilde{q}_{tB} = -\Delta_B q_t$. Comparing Eq.C.14 with Eq.C.11 gives b_I and G_I :

$$b_I = \exp[-\epsilon \Delta p_C] \quad (\text{C.15})$$

$$G_I = (1 - \exp[-\epsilon \Delta p_C]) / \epsilon \quad (\text{C.16})$$

A similar derivation for θ_{vl} leads to a cumulus excess of $\widetilde{\theta}_{vl} = -G_I \gamma_{vl}$ because $\Delta_B \theta_{vl} = 0$.

Alternatively, we may derive equations for a cloud model in which $\epsilon(p) \sim c_e/dp$ and $\delta(p) \sim c_d/dp$ (Pa^{-1}):

$$\begin{aligned}\int_{p_I}^{p_B} \frac{dM}{M} &= -\int_{p_I}^{p_B} \left(\frac{c_e}{p_S - p} - \frac{c_d}{p_S - p} \right) dp \\ m_I &= \exp[(c_e \ln \widehat{p}_I) - (c_d \ln \widehat{p}_I)] \\ &= \frac{\widehat{p}_I^{c_e}}{\widehat{p}_I^{c_d}} \quad \text{with} \quad \widehat{p}_I = \frac{p_S - p_I}{p_S - p_B}\end{aligned}\quad (\text{C.17})$$

Repeating the derivation for b_I and G_I using the gradient of \widetilde{q}_t in the cumulus layer:

$$\frac{d\widetilde{q}_t}{dp} = \epsilon(p) \widetilde{q}_t + \gamma_{qt} \quad (\text{C.18})$$

$$f(p) \left(\frac{d\widetilde{q}_t}{dp} \right) - f(p) \epsilon(p) \widetilde{q}_t = f(p) \gamma_{qt} \quad (\text{C.19})$$

Taking $f(p) = \exp \left[- \int_{p_I}^{p_B} (\epsilon(p) dp) \right] = \exp [c_e \ln \hat{p}] = \hat{p}_I^{c_e}$ we can write:

$$\int_{p_I}^{p_B} \frac{d(f(p)\tilde{q}_t)}{dp} dp = \gamma_{qt} \int_{p_I}^{p_B} f(p) dp \quad (\text{C.20})$$

giving the solution:

$$\begin{aligned} \tilde{q}_{tI} &= \left(-\frac{1}{f(p)} \int_{p_I}^{p_B} f(p) dp \right) \gamma_{qt} + \frac{1}{f(p)} \tilde{q}_{tB} \\ &= -\frac{1}{\hat{p}_I^{c_e}} \frac{p_S - p_B}{c_e + 1} (\hat{p}_I^{c_e+1} - 1) \gamma_{qt} - \frac{1}{\hat{p}_I^{c_e}} \Delta_B q_t \end{aligned}$$

which leads to b_I and G_I :

$$b_I = \frac{1}{\hat{p}_I^{c_e}} \quad (\text{C.21})$$

$$G_I = \frac{p_S - p_B}{c_e + 1} \frac{(\hat{p}_I^{c_e+1} - 1)}{\hat{p}_I^{c_e}} \quad (\text{C.22})$$

Equation C.10, C.15 and C.16 are used for the cloud model with constant entrainment and detrainment. Equation C.17, C.21 and C.22 are used for a cloud model with entrainment and detrainment varying with pressure. $\epsilon, \delta, c_e, c_d$ are obtained from the LES results in Chapter 4 for the S_{8.5} case and included in Table 4.3.

A third option we explore is to fix the non-dimensional mass flux at cloud top (the inversion). This approach is inspired by De Rooij and Siebesma (2008) who show that entrainment varies little from case to case and can be formulated by the standard parameterization ($\epsilon \sim c_e/dp$ in Pa⁻¹). For δ however, which often shows a much greater

dependence on cloud depth (decreases for deeper clouds), a more dynamical parameterization may be more appropriate *i.e.*, one that allows a fixed fraction of the mass flux to remain at cloud top.

Choosing the non-dimensional mass flux at cloud top (the inversion) $m_I = (0.2 - 0.4)$, one can obtain an equation for δ that can be used to derive $m_p = M_{cp}/M_{cB}$ at all pressure levels. b_I and G_I still depend only on $\epsilon \sim c_e/dp$ as in Equation C.21 and C.22.

$$m_p = \exp [c_e \ln(\hat{p}_I) - \delta (p - p_B)] \quad (\text{C.23})$$

$$\delta = [-\ln(m_I) + c_e \ln(\hat{p})]/(p_I - p_B) \quad \text{with} \quad \hat{p} = \frac{p_S - p}{p_S - p_B} \quad (\text{C.24})$$

Bibliography

- Albrecht, B., A. Betts, W. Schubert, and S. Cox, 1979: A model of the thermodynamic structure of the trade-wind boundary layer, Part I: Theoretical formulation and sensitivity tests. *J. Atmos. Sci.*, **36**, 90–98.
- Arakawa, A. and W. Schubert, 1974: Interaction of a cumulus cloud ensemble with the large-scale environment, Part I. *J. Atmos. Sci.*, **31**, 674–701.
- Augstein, E., H. Riehl, F. Ostapoff, and V. Wagner, 1974: The vertical structure of the atmospheric planetary boundary layer in undisturbed trade winds over the Atlantic Ocean. *Boundary Layer Meteorology*, **6**, 129–150.
- Austin, G., R. Rauber, H. Ochs III, and L. Miller, 1996: Trade-wind clouds and Hawaiian rainbands. *Mon. Wea. Rev.*, **124**, 2126–2151.
- Austin, J., 1948: A note on cumulus growth in a nonsaturated environment. *J. Meteor.*, **5**, 103–107.
- Back, L. and C. Bretherton, 2005: The relationship between wind speed and precipitation in the pacific itcz. *J. Climate*, **18**, 4317–4328.
- Bellon, G. and B. Stevens, 2005: On bulk models of shallow cumulus convection. *J. Atmos. Sci.*, **62**, 3286–3302.

- Betts, A. and W. Ridgway, 1989: Climatic equilibrium of the atmospheric convective boundary layer over a tropical ocean. *J. Atmos. Sci.*, **46**, 2621–2641.
- Bony, S., J.-L. Dufresne, H. Le Treut, J.-J. Morcrette, and C. Senior, 2004: On dynamic and thermodynamic components of cloud changes. *Clim. Dyn.*, **22**, 71–86.
- Bretherton, C., 1993: Understanding albrecht’s model of trade-cumulus cloud fields. *J. Atmos. Sci.*, **50**, 2264–2283.
- Bretherton, C. and S. Park, 2008: A new bulk shallow-cumulus model and implications for penetrative entrainment feedback on updraft buoyancy. *J. Atmos. Sci.*, **65**, 2174–2193.
- Bretherton, C., M. Peters, and L. Back, 2004: Relationships between water vapor path and precipitation over the tropical oceans. *J. Climate*, **17**, 1517–1528.
- Byers, H. and R. Hall, 1955: A census of cumulus cloud-height versus precipitation in the vicinity of Puerto Rico during the winter and spring of 1953-1954. *J. Atmos. Sci.*, **12**, 176–178.
- Caesar, K., 2005: Summary of the weather during the RICO project, available online at www.eol.ucar.edu/rico.
- Clarke, A., V. Kapustin, S. Howell, K. Moore, B. Lienert, S. Masonis, T. Anderson, and D. Covert, 2003: Sea-salt size distributions from breaking waves: implications for marine aerosol production and optical extinction measurements during SEAS. *J. Atmos. Oceanic Technol.*, **20**, 1362–1374.
- Colón-Robles, M., R. Rauber, and J. Jensen, 2006: Influence of low-level wind speed on droplet spectra near cloud base in trade wind cumulus. *Geophys. Res. Lett.*, **33**.

- Conzemius, R. and E. Federovich, 2006: Dynamics of sheared convective boundary layer entrainment. Part i: Methodological background and Large-Eddy Simulations. *J. Atmos. Sci.*, **63**, 1151–1178.
- De Rooij, W. and A. Siebesma, 2008: A simple parameterization for detrainment in shallow cumulus. *Mon. Wea. Rev.*, **136**, 560–576.
- Doneaud, A., S. Ionescu-Niskov, D. Priegnitz, and P. Smith, 1984: The area-time integral as an indicator for convective rain volumes. *J. Appl. Meteor.*, **23**, 555–561.
- Fairall, C., E. Bradley, J. Hare, A. Grachev, and J. Edson, 2003: Bulk parameterization of air-sea fluxes: Updates and verification for the COARE algorithm. *J. Climate*, **16**, 571–591.
- Garratt, J., 1992: *The atmospheric boundary layer*. Cambridge University Press.
- Gray, W. and R. Jacobson Jr., 1977: Diurnal variation of deep cumulus convection. *Mon. Wea. Rev.*, **105**, 1171–1188.
- Holland, J. and E. Rasmusson, 1973: Measurements of the atmospheric mass, energy and momentum budgets over a 500-km square of tropical ocean. *Mon. Wea. Rev.*, **101**, 44–55.
- Holloway, C. and J. Neelin, 2009: Moisture vertical structure, column water vapor and tropical deep convection. *J. Atmos. Sci.*, **66**, 1665–1683.
- Hudson, J. and S. Mishra, 2007: Relationships between CCN and cloud microphysics variations in clean maritime air. *Geophys. Res. Lett.*, **34**.

- Jensen, J., S. Lee, P. Krummel, J. Katzfey, and D. Gogoasa, 2000: Precipitation in marine cumulus and stratocumulus. part I: Thermodynamic and dynamic observations of closed cell circulations and cumulus bands. *Atmos. Res.*, **54**, 117–155.
- Johnson, R., T. Rickenbach, S. Rutledge, P. Ciesielski, and W. Schubert, 1999: Trimodal characteristics of tropical convection. *J. Climate*, **12**, 2397–2418.
- Joss, J. and R. Lee, 1995: The application of radar-gauge comparisons to operational precipitation profile corrections. *J. Appl. Meteor.*, **34**, 2612–2630.
- Knight, C. and L. Miller, 1993: First radar echoes from cumulus clouds. *J. Atmos. Sci.*, **74**, 179–188.
- 1998: Early radar echoes from small, warm cumulus: Bragg and hydrometeor scattering. *J. Atmos. Sci.*, **55**, 2974–2992.
- Knight, C., L. Miller, and R. Rilling, 2008: Aspects of precipitation development in trade wind cumulus revealed by differential reflectivity at s band. *J. Atmos. Sci.*, **65**, 2563–2580.
- Lau, K. and H. Wu, 2003: Warm rain processes over tropical oceans and climate implications. *Geophys. Res. Lett.*, **30**.
- LeMone, M. and W. Pennell, 1976: The relationship of trade wind cumulus distribution to subcloud layer fluxes and structure. *Mon. Wea. Rev.*, **104**, 524–539.
- Lilly, D., 1968: Models of cloud-topped mixed layers under a strong inversion. *Quart. J. Roy. Meteor. Soc.*, **94**, 292–309.

- Medeiros, B., L. Nuijens, C. Antoniazzi, and B. Stevens, 2010: Low-latitude boundary layer clouds as seen by CALIPSO, in preparation for *J. Geophys. Res.*
- Medeiros, B., B. Stevens, I. Held, M. Zhao, D. L. Williamson, J. G. Olson, and C. S. Bretherton, 2008: Aquaplanets, climate sensitivity, and low clouds. *J. Climate*, **21**, 4974–4991.
- Moeng, C.-H. and P. Sullivan, 1994: A comparison of shear and buoyancy-driven planetary boundary layer flows. *J. Atmos. Sci.*, **51**, 999–1022.
- Neggers, R., J. Neelin, and B. Stevens, 2007: Impact mechanisms of shallow cumulus convection on tropical climate dynamics. *J. Climate*, **20**, 2623–2642.
- Neggers, R., B. Stevens, and J. Neelin, 2006: A simple equilibrium model for shallow-cumulus-topped mixed layers. *Theor. and Comp. Fluid. Dyn.*, **20**, 305–322.
- Nesbitt, S. and E. Zisper, 2003: The diurnal cycle of rainfall and convective intensity according to three years of TRMM measurements. *J. Climate*, **16**, 1456–1475.
- Nuijens, L., 2005: *Estimating precipitation from radar observations in the trade-wind cumulus region*. Master's thesis, Wageningen University and Research Center.
- Nuijens, L., B. Stevens, and A. Siebesma, 2009: The environment of precipitating shallow cumulus convection. *J. Atmos. Sci.*, **66**, 1962–1979.
- Peter, J., A. Blyth, B. Brooks, J. McQuaid, J. Lingard, and M. Smith, 2008: On the composition of Caribbean maritime aerosol particles measured during RICO. *Quart. J. Roy. Meteor. Soc.*, **134**, 1059–1063.

- Petty, G., 1999: Prevalence of precipitation from warm-topped cumulus clouds over eastern Asia and the western Pacific. *J. Climate*, **12**, 220–229.
- Pino, D., J. Vilà-Guerau de Arellano, and P. Duynkerke, 2003: The contribution of shear to the evolution of a convective boundary layer. *J. Atmos. Sci.*, **60**, 1913–1926.
- Rauber, R. M., B. Stevens, and co authors, 2007: Rain in (shallow) cumulus over the ocean - the RICO campaign. *Bull. Amer. Meteor. Soc.*, **88**, 1912–1928.
- Raymond, D., 2005: Regulation of moist convection over the west pacific warm pool. *J. Atmos. Sci.*, **52**, 3945–3959.
- Reynolds, R. W., N. A. Rayner, T. M. Smith, D. C. Stokes, and W. Wang, 2002: An improved in situ and satellite SST analysis for climate. *J. Climate*, **15**, 1609–1625.
- Schumacher, C. and R. Houze, Jr., 2003: The TRMM precipitation radar's view of shallow, isolated rain. *J. Appl. Meteor.*, **42**, 1519–1524.
- Scotti, A., C. Meneveau, and D. Lilly, 1993: Generalized Smagorinsky model for anisotropic grids. *Phys. of Fluids A*, **5**, 2306–2308.
- Seifert, A. and K. D. Beheng, 2001: A double-moment parameterization for simulating autoconversion, accretion and selfcollection. *Atmos. Res.*, **59-60**, 265–281.
- Short, D. and K. Nakamura, 2000: TRMM radar observations of shallow precipitation over the tropical oceans. *J. Climate*, **13**, 4107–4124.
- Siebert, H., H. Franke, L. K., R. Maser, E. Saw, D. Schell, R. Shaw, and M. Wendisch, 2006a: Probing fine scale dynamics and microphysics of clouds with helicopter-borne measurements. *Bull. Amer. Meteor. Soc.*, **87**, 1727–1738.

- Siebert, H., K. Lehmann, and M. Wendisch, 2006b: Observations of small-scale turbulence and energy dissipation rates in the cloudy boundary layer. *J. Atmos. Sci.*, **63**, 1415–1466.
- Siebesma, A. P., C. S. Bretherton, A. Brown, A. Chlond, J. Cuxart, P. G. Duynkerke, H. L. Jiang, M. Khairoutdinov, D. Lewellen, C. H. Moeng, E. Sanchez, B. Stevens, and D. E. Stevens, 2003: A large eddy simulation intercomparison study of shallow cumulus convection. *J. Atmos. Sci.*, **60**, 1201–1219.
- Snodgrass, E., 2006: *Precipitation characteristics from trade wind clouds during RICO derived from radar, satellite and aircraft measurements*. Master’s thesis, University of Illinois at Urbana-Champaign.
- Sobel, A., S. Yuter, C. Bretherton, and G. Kiladis, 2004: Large-scale meteorology and deep convection during TRMM KWAJEX. *Mon. Wea. Rev.*, **132**, 422–444.
- Stevens, B., 2005: Atmospheric moist convection. *Annu. Earth Planet. Sci.*, **33**, 605–643.
- 2006: Bulk boundary layer concepts for simplified models of tropical dynamics. *Theoretical and Computational Fluid Dyn.*, **20**, 279–304.
- 2007: On the Growth of Layers of Non-precipitating Cumulus Convection. *J. Atmos. Sci.*, **64**, 2916–2931.
- Stevens, B., C. Moeng, A. Ackerman, C. Bretherton, A. Chlond, S. De Roode, J. Edwards, J. Golaz, H. Jiang, M. Khairoutdinov, M. Kirkpatrick, D. Lewellen, A. Lock, F. Muller, D. Stevens, E. Whelan, and P. Zhu, 2005: Evaluation of large-eddy sim-

- ulations via observations of nocturnal marine stratocumulus. *Mon. Wea. Rev.*, **133**, 1443–1462.
- Stevens, B. and A. Seifert, 2008: Understanding macrophysical outcomes of microphysical choices in simulations of shallow cumulus convection. *J. Meteorol.Soc.Japan*, **86**, 143–162.
- Stevens, B. et al., 2001: Simulations of trade wind cumuli under a strong inversion. *J. Atmos. Sci.*, **58**, 1870–1891.
- Teller, A. and Z. Levin, 2006: The effects of aerosols on precipitation and dimensions of subtropical clouds: a sensitivity study using a numerical cloud model. *Atmos.Chem.Phys.*, **6**, 67–80.
- Tiedtke, M., 1989: A comprehensive mass flux scheme for cumulus parameterization in large-scale models. *Mon. Wea. Rev.*, **117**, 1779–1800.
- Trivej, P. and B. Stevens, 2010: The echo size distribution of precipitating shallow cumuli. *J. Atmos. Sci.*, **67**, 788–804.
- Tustison, B., D. Harris, and E. Foufoula-Georgiou, 2001: Scale issues in verification of precipitation forecasts. *J. Geophys. Res.*, **106**, 11775–11784.
- Twohy, C. and J. Anderson, 2008: Droplet nuclei in non-precipitating clouds: composition and size matter. *Environ.Res.Lett.*, **3**, 1–9.
- Van Zanten, M., B. Stevens, L. Nuijens, A. Siebesma, A. Ackerman, P. Bogenschutz, F. Burnet, A. Cheng, F. Couvreux, H. Jiang, M. Khairoutdinov, D. Lewellen, A. Noda, D. Mechem, B. Shipway, J. Slawinska, and S. Wang, 2010: Controls on precipitation

- and cloudiness in simulations of shallow fair-weather cumulus, in preparation for *Atmos. Chem. Phys.*
- Woodcock, A., 1953: Salt nuclei in marine air as a function of altitude and wind force. *J. Meteor.*, **10**, 363–371.
- Xue, H. and G. Feingold, 2006: Large-eddy simulations of trade wind cumuli: Investigation of aerosol indirect effects. *J. Atmos. Sci.*, **63**, 1605–1622.
- Xue, H., G. Feingold, and B. Stevens, 2007: Aerosol effects on clouds precipitation, and the organization of shallow cumulus convection. *J. Atmos. Sci.*, **65**, 392–406.
- Yin, B. and B. Albrecht, 2000: Spatial variability of atmospheric boundary layer structure over the eastern equatorial Pacific. *J. Climate*, **13**, 1574–1592.
- Zhao, H. and L. Di Girolamo, 2007: Statistics on the macrophysical properties of trade wind cumuli over the tropical western Atlantic. *J. Geophys. Res.*, **112**, (D10204) doi:10.1029/2006JD007371.